Multi-Epoch Millimeter VLBI Observations of the Twin-Jet System in NGC 1052

Masterarbeit aus der Physik
vorgelegt von

Anne-Kathrin Baczko

08. 04. 2015

Dr. Karl Remeis-Sternwarte Bamberg
Erlangen Centre for Astroparticle Physics
Friedrich-Alexander-Universität
Erlangen-Nürnberg

Betreuer:
Prof. Dr. Jörn Wilms
Prof. Dr. Matthias Kadler

Abstract

This Master thesis reports on a detailed analysis of the emission from the center of the active galaxy NGC 1052 at 22, 43, and 86 GHz. The active galactic nucleus (AGN) of this elliptical galaxy hosts two radio-emitting jets with an unresolved emission gap in between at lower frequencies. This gap can be explained by an absorbing torus. Due to its distance of about 19 Mpc, the innermost structure can be analyzed in great detail with millimeter-wavelength very-long-baseline interferometry (VLBI).

AGNs are known for strong emission over the whole electromagnetic spectrum. To explain the high energy output a super massive black hole (SMBH) is thought to be located at the center. A unified scheme was developed to describe most aspects seen in different classes of AGN, but the underlying physical processes are not completely understood, yet. The low luminosity AGN NGC 1052 is an excellent source to test current jet models, thanks to its orientation near to the plane of the sky and the observed twin-jet structure. Observations at 3 mm wavelength reveal a strong central feature, smaller than 8.6 μas along the jet angle, from that both jets are emanating with similar brightness. This gave rise to the question whether the central radio feature is the center of the AGN.

To check this assumption, I analyzed 29 VLBI-observations at 22 GHz and 43 GHz carried out between March 2005 and April 2009. Two attempts were made to test whether the central feature is the center of the source. The technique of phase-referencing recovers the relative position of VLBI observations to align the maps. A kinematic study was performed to track the kinematic center of the jets. The proper motions for both jets were derived to $\mu = 1.12 \pm 0.46\,\mathrm{mas\,yr^{-1}}$ for the eastern jet and $\mu = 1.86 \pm 0.61\,\mathrm{mas\,yr^{-1}}$ for the western jet, leading to apparent speeds of $\beta = 0.34 \pm 0.14$ and $\beta = 0.56 \pm 0.18$, respectively. A detailed analysis of the morphology and flux evolution revealed an asymmetry in the two-sided jet system. Measurements of the brightness temperature gradient and opening angle of the jets support these assumptions and show distinctions from the standard model describing a conical jet. In contrast to previous studies of NGC 1052, which identified the eastern jet to be approaching and the western jet to be receding, in this work the western jet was proved is the brighter one.

In 2006 the jet-system was very symmetric. Starting in 2007 the morphology of the source showed a significant asymmetry, which is seen in the flux ratio between western and eastern jet, too. It rises from around 1 in 2006 to a mean value of 1.7 from 2007 on. There are two possible reasons for this asymmetry: a change of the inclination angle of the jets to the line of sight or an intrinsic asymmetry. Assuming initial symmetric jet parameters, same brightness and velocity for both jets, an estimate on the inclination angle for 2006, and 2007 to 2009 was derived. Within 1σ Gaussian error of the flux density ratios and velocities, the angle to the line of sight has to change from the lowest possible value during 2006 of 84 ° to the highest possible value after 2006 of 80 ° to explain the results from my analysis.

An asymmetry in the jets is more likely than the change of angle to the line of sight, since the morphology, the flux density, and brightness temperature studies reveal an asymmetry in the twin-jet. To explain and initial asymmetry the intrinsic assumptions could be wrong: the velocities and/or the flux densities are not initially the same for both jets. There could be differences in the jet-production for the western and eastern jet, for example resulting from an asymmetric magnetic field or changing particle densities. It is possible that there is an external distorting medium, that has more impact on one of the jets than on the other. To verify the reason for the observed asymmetry more studies have to be conducted, testing the magnetic field, and material producing or distorting the jets.

Contents

1 Introduction

Electro-magnetic radiation at optical wavelengths can penetrate the atmosphere since we are able to see optical (visible) light. We see stars and a lot more in the universe that is bright enough to get perceived by our eyes. What is too faint for our eyes can still be seen by optical telescopes on earth, objects that appear point-like may be resolved by a telescope. To overcome absorption and turbulences in the atmosphere, the next big step is to go to outer space, for example with the Hubble Space Telescope (HST).

But there is another possibility to ascertain the properties of the universe from surface of the earth. There is a second window through that we can have a look at outer space. It is located between wavelength of mm up to several meters, as shown in Fig. 1. Radiation at these wavelengths is known as radio emission and it is not strongly affected by our atmosphere. The resolution θ of an image depends

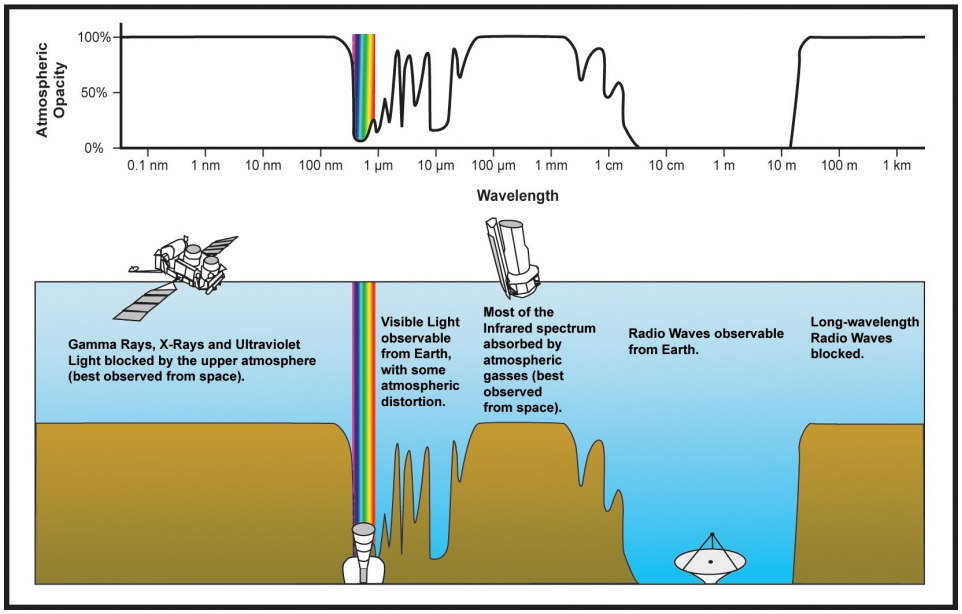

Figure 1.1.: *The observational possibilities due to the opacity of the atmosphere*

on the wavelength λ and the diameter D of the telescope as

$$\theta = 1.22\frac{\lambda}{D}. \tag{1.0.1}$$

For example the human eye responds to wavelength from about 390 nm to 700 nm and can resolve, with a comparable small size of the pupil, an angle of about 1 arcmin.

Such a good resolution is only possible, because we are able to see optical light. If we now want to observe with a radio telescope at a typical frequency of 15 GHz (corresponding to a wavelength of about

2 cm) we would need a telescope with a diameter of about 84 m to achieve the same resolution. That is possible, e.g., the Effelsberg telescope (see Fig. 1) has a diameter of 100 meter. At present the largest radio aperture is the Arecibo Observatory in Puerto Rico with a dish diameter of 305 m. As shown in Fig. 1 it is not steerable, but the receiver can be moved around in the focal plane, so that a range of 15° in declination and an elevation from 75° to the zenith can be reached.

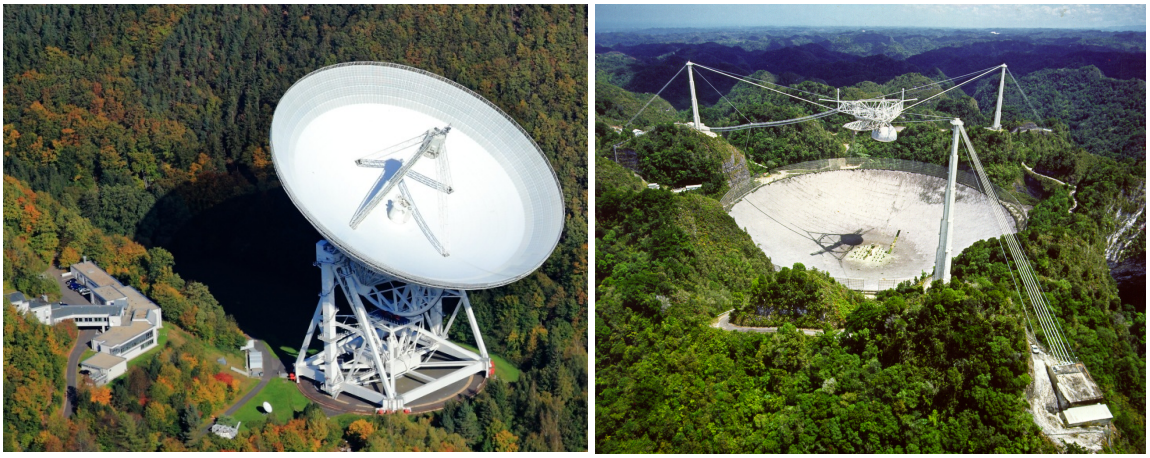

Figure 1.2.: *Left:The Effelsberg telescope in Bonn, Germany. (Foto: Peter Sondermann, VisKom/City-Luftbilder); Right: The Arecibo Observatory, Puerto Rico. (courtesy of the NAIC - Arecibo Observatory, a facility of the NSF)*

So the maximum possible diameter of a radio dish seems to be on the order of a few hundred meters, at present. This leads to a maximum possible angular resolution of 0.4 arcmin for the highest observational frequency at Arecibo of 10 GHz. A new telescope is under construction in China which will have a diameter of 500 m, which would result in $\theta = 0.25$ arcmin at the same frequency.

However, this is not the largest radio antenna that is possible. By translating the idea of the Michelson-Interferometer to radio astronomy even higher angular resolutions can be reached. An interferometer of two radio antennas, when interferometrically connected, represents an radio telescope with a diameter as large as the distance between the two telescopes. If telescopes are used in this way and their distance is large, e.g. some hundreds of kilometer, the used technique is called Very-Long-Baseline Interferometry (VLBI). Typically, the shortest spacings in VLBI are of the order of kλ to Mλ, in units of observing wavelengths, in this way, the inverse of the baseline will be approximately the resolution in radians. A key point of astronomical studies in this wavelength band is focused on compact objects, like neutron stars or black holes.

This thesis takes a closer look at so called Active Galactic Nuclei (AGN). AGNs define a special class of galaxies, its nucleus can be brighter than the whole host galaxy. The radiation is not produced directly by stellar emission, but by complex mechanisms around the SMBH in the center.
I will first give a short introduction of AGN and the mechanisms that lead to the observed radio emission. Afterwards I will discuss the technique of VLBI and the processes needed to retain an image out of an VLBI observation. Then I will introduce the observations of the low luminosity AGN NGC 1052 conducted with the Very Long Baseline Array (VLBA) and how current AGN models can be tested.

2 | Active Galactic Nuclei - an introduction

All galaxies probably host a Super Massive Black Hole (SMBH) in their center. Besides that there exists a special class of galaxies, which have a so called *active nucleus*. These are bright over the whole electromagnetic spectrum. The center is referred to as an *Active Galactic Nucleus* (AGN). In the following I will introduce the physical principles, that are able to describe observational properties of AGN. The presented information is based on the textbooks from Schneider (2008) and Krolik (1999).

2.1. Types of AGN - a historical view

AGNs can be divided into different classes based on their physical properties and by historical reasons:

Quasi-stellar radio source (Quasars) belong to the first radio sources that where identified with their optical counterpart, e.g. the radio source 3C 273 by Maarten Schmidt. As the name would suggest they appear point-like. Quasars are very bright and can so be observed out to very high redshifts (e.g. z=6). They have high variability from X-Ray to radio wavelength. Observations of the optical identifications revealed a very bluish spectrum and broad emission lines. That gave the possibility to search for optical galaxies with these properties. Most of the observed sources appeared to be only weak radio emitters, if any. These were named as *Quasi Stellar Objects* (QSOs). Since these sources show in principle the same properties as Quasars, but with weaker radio emission, they were renamed as *radio-quiet Quasars*. At present time radio-quiet Quasars and Quasars are summarized as QSOs.

Blazars are very compact radio sources, that can be distinguished into *BL-Lacertae* (BL Lacs) and *Optically Violently Variables* (OVV). BL Lacs are named after the prototype of this class: BL Lacertae. Both exhibit high variability at very high energies, especially for γ emission. The optical emission is strongly polarized. OVVs show broad emission lines, whereas BL Lacs lack these. However, as the luminosity of a BL Lac is in a low state emission lines can be observed, what leads to a classification as a OVV during these epochs. This suggests that both classes are very similar and can be summarized as the so called Blazars.

Seyfert Galaxies are named after Carl Seyfert, who observed bright quasi-stellar objects, with a point-like nucleus in 1943. They exhibit lower luminosity compared to QSOs, but a very similar optical spectrum and are most of the time identified with spiral galaxies. They show a very bright core and broad emission lines. This class can be divided into two subtypes, similar to these already introduced: Seyfert 1 and Seyfert 2. In Seyfert 1 broad permitted and narrow forbidden lines can be observed, while Seyfert 2 exhibit only narrow lines and have a weaker continuum. There can be a lot of intermediate classes between Seyfert 1 and 2, since some sources can be mostly classified as Seyfert 2 but show additional some broad lines. In sum Seyfert galaxies are very similar to QSOs besides the differences in luminosity.

Low-ionization nuclear emission-line region galaxies (LINER) are very similar to Seyfert 2, but show a slightly different spectrum. Meaning that the strongest lines are that from low-ionization.

Radio Galaxies have a strong radio emission, that can outshine the emission of the host galaxy, that is in most cases an elliptical one. Optical classification divides them into *Broad Line Radio Galaxies (BLRG)* and *Narrow Line Radio Galaxies (NLRG)*, similar to the separation into Seyfert 1 and 2. Therefore radio galaxies could be denoted as radio-lout Seyferts. The prototype of this class is Centaurus A, that is the closest AGN. In contrast to Quasars extended radio emission up to several kpc can be observed. Besides the division due to the optical spectrum, radio galaxies can be split based on the observed extended structure following Fanaroff & Riley (1974). FR 1 have a very dominating, bright core and show two jets, whereas FR 2 have usually a single sided jet, are weaker and dominated by lobes. It follows that the luminosity with distance from core decreases in FR type 1 and increases in FR type 2.

2.2. AGN: towards unification?

As suggested by Antonucci (1993) as well as Urry & Padovani (1995) and is common understanding in present time all classes of AGN as described in the previous section can be summarized in one unified model, as can be seen in Fig. 2.1. The standard model of AGNs consist of a super-massive black hole

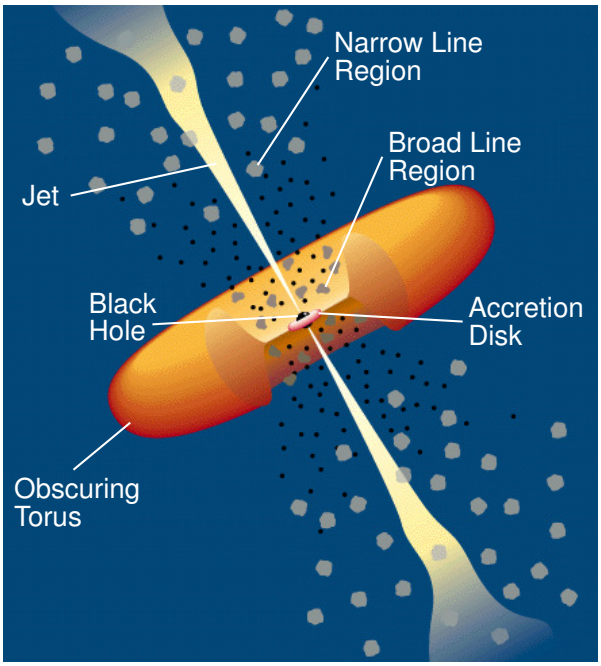

Figure 2.1.: *Unification Model for a radio-loud AGN. Credit: (Urry & Padovani (1995))*

(SMBH) with a surrounding accretion disc and dust torus. Perpendicular to the accretion disk jets are emitted. Jets can be described as *relativistic collimated beam of matter*. Interaction with the interstellar medium can lead to so called *lobes*, that are at the very end of the jets.

AGNs are very energetic and can outshine a whole galaxy. The only possible physical process that can lead to an amount of released energy that big is accretion. Eddington luminosity is the maximum luminosity that is possible due to accretion. It can be derived as:

$$L_{\mathrm{Edd}} = \frac{4\pi G M c m_p}{\sigma_T} = 1.3 \times 10^{38} \mathrm{erg\,s^{-1}} \frac{M}{M_\odot} \tag{2.2.1}$$

E.g. Boettcher et al. (2012). Jets, as are observed in many AGNs, can only be produced in the surrounding of massive objects, that possesses an accretion disk. Objects that are very near to a

massive object aren't capable to maintain their shape and will form an accretion disk around it. As long as the angular momentum of the accretion disk is preserved the matter will stay in orbits around the massive object.

Observations have shown that around the accretion disc seems to be a torus, that obscures the emission from the inner region of jet, the accretion disk and gas clouds around. As the observational frequency gets higher, as less obscured is the emission. Let the massive object from now on be a SMBH, even if all the following models apply to other massive objects like neutron stars, too. Theory suggests that there exists a strong magnetic field around the SMBH, that is locked to the accretion flow. How it is initially formed isn't fully understood, yet. As the accretion disk rotates, the magnetic field lines get twisted and so the initial poloidal magnetic field gets toroidal. Charged particles will encounter the Lorentz force, that is in the absence of an electric field:

$$\frac{\mathrm{d}\mathbf{p}}{\mathrm{d}t} = \frac{e}{c}\mathbf{v} \times \mathbf{B}, \tag{2.2.2}$$

where $\mathbf{p} = \gamma m_e \mathbf{v}$. The particles will spiral along the magnetic field. This results in matter that will move along the field lines and away from the accretion disk. Until now it isn't clear whether the particles are hadronic or leptonic. As a consequence the accretion flow losts angular momentum and this leads to accretion onto the SMBH - there exists other mechanisms that can in the end start the accretion onto a massive object. The field lines rotate, it follows that the gas will be accelerated as moving outwards. The combination of outflowing material and the formed toroidal magnetic fields leads to a *self-collimation* of the jet.

As can be seen in Fig. 2.1 there can be observed narrow and broad emission lines, depending on the distance of the observed region from the central engine. The so called *Broad Line Region (BLR)* is located between accretion disk and torus and consists of clouds of matter. The emission lines are very broad due to the high angular velocity. The widths are of the order of $\mathcal{O}(1000\,\mathrm{km\,s^{-1}})$.

The Narrow Line Region (NLR) is located further away from the black hole, starting at about 100 pc. The medium is less dense and more uniform than in the BLR. Due to its greater distance the gas is colder and following the line widths are narrower ($\mathcal{O}(100\,\mathrm{km\,s^{-1}})$). For this region strong permitted and narrow forbidden lines can be observed. From the previous considerations the different classes of AGN, e.g. Seyfert galaxies or Blazars, can be described by simply observing the AGN from different angles. As the torus is in the line of sight, the BLR will be obscured and with that no broad emission lines can be seen. This is the case for Seyfert 2, Liner 2 or NLRG. Blazars have a jet pointing directly towards the observer.

The mechanisms that take place around objects as massive as black holes and that are able to form jets can be theoretically described by magnetohydrodynamics (MHD). The underlying physical process can be probed by numerical simulations. By modifying the initial parameters that way that an object similar to observations is produced, properties affecting the formation of the source can be found out.

Observations of galactic systems with bipolar jets often show asymmetric shapes. For example velocity asymmetries were found for the galactic T Tauri star RW Aur in the optical wavelength regime (see e.g Woitas et al. (2002) or Hartigan & Hillenbrand (2009)). In extragalactic jets on parsec and kiloparsec scales, observed asymmetries can be explained by relativistic effects, in most cases, and no evidences for an intrinsic asymmetry are found. Simulations by Fendt & Sheikhnezami (2013) are capable to produce asymmetric jets. By adding asymmetries in the disk pressure distribution to an otherwise symmetric accretion disk, asymmetries for jet and counterjet could be produced (See Fig 2.2). Not only turned the asymmetry out to be long lasting also the asymmetry seamed to get reversed, leading to a less massive jet compared to the counter jet.

2.3. Modeling a jet

I described the physical principles needed to describe AGN in the previous sections. For the end of this chapter the emphasis is on the description of AGN jets. The common understanding follows the models of Blandford & Königl (1979) and Königl (1981).

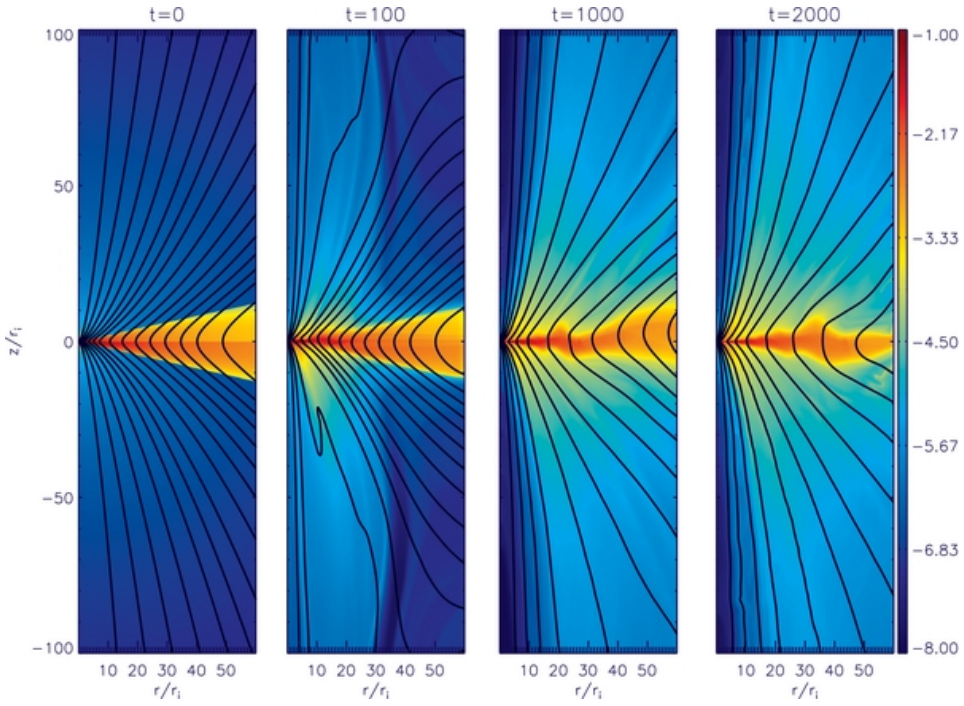

Figure 2.2.: *Simulation by Fendt & Sheikhnezami (2013) producing an asymmetric jet. Shown is the bipolar jet-disk structure. The only added asymmetry lies in different thermal scale heights for the disk hemispheres. From left to right the evolution for dynamical times t= 0, 100, 1000, 2000 of the mass density (colors) and the poloidal magnetic field (lines) are shown. The disk is horizontal in the middle.*

The basic properties of the jet are the same for both models. The jet is assumed to be narrow, evolves conical and has a constant velocity $\beta_{\rm jet}$. The energy density n of the continuously ejected electrons follow a power law $n_{\rm e} \propto r^n$ along the jet axis r. The magnetic field behaves the same, therefore following a power law $B \propto r^b$. In the following the physical principles responsible for the jet emission as well as observational properties due to relativistic effects will be discussed.

2.3.1. Forces on charged particles in a magnetic field: synchrotron radiation

The most important process that leads to radio emission is synchrotron radiation. Maxwells equation show that a charged particle that is accelerated emits radiation. This happens for example in a magnetic field. I will in the following introduce some useful quantities and describe the physical principle of the production of synchrotron radiation as well a its observables. For more details see Rybicki & Lightman (2004).

For the case of absent electric field a relativistic moving electron will sense the Lorentz-Force as was already introduced in Eq. 2.2.2. For the moment we assume that γ is constant, thus no radiation is emitted. From Eq. 2.2.2 it follows that there is only acceleration perpendicular to the **B** field. By comparing the forces it becomes clear that the electron describes a circular motion around the magnetic field lines with the angular frequency:

$$\omega_{\rm B} = \frac{eB}{\gamma m_e c}. \tag{2.3.1}$$

In the non-relativistic case the frequency $\omega_{\rm L} = \gamma\omega_{\rm B}$ is called angular Larmor frequency, that leads to a Larmor frequency of $\nu_{\rm L} = \omega_{\rm L}/2\pi = 2.8\,{\rm MHz} \cdot \frac{B}{1{\rm G}}$. The in this way accelerated electron radiates and

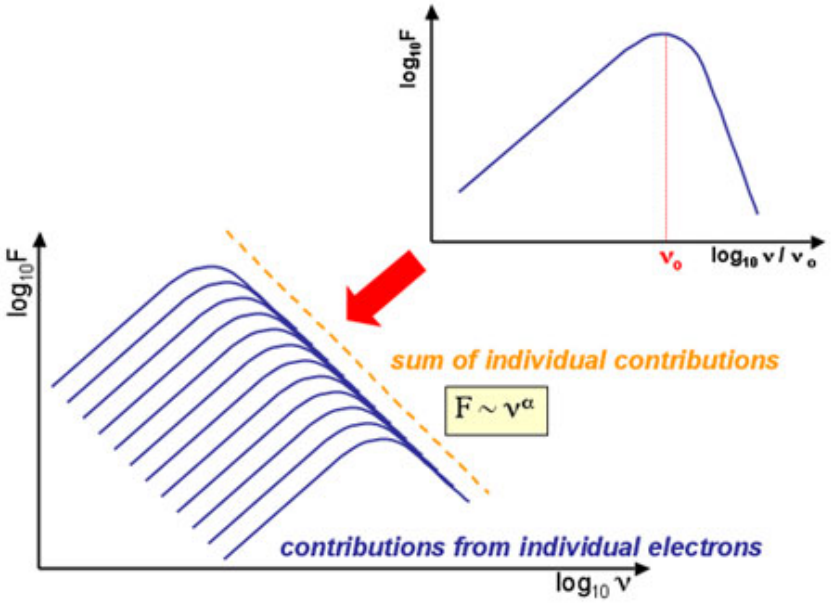

Figure 2.3.: *Upper right: synchrotron spectrum of individual electrons; lower left: superposition of electron power law energy distribution results in a power law spectrum. Credit:* http://astronomy.swin.edu.au/cosmos/s/synchrotron+emission

the emitted power per electron can be derived as

$$P_{\mathrm{em}} = \left(\frac{2}{3}\right)^2 r_0^2 c\beta^2\gamma^2 B^2 \tag{2.3.2}$$

Due to relativistic effects the emission is beamed into a cone with opening angle $\approx \gamma^{-1}$. So one expects to see pulses of the emission every time when the cone strikes the observer. Doing some more calculations, the spectrum of a single electron (see Fig. 2.3) will have the characteristic frequency

$$\omega_{\mathrm{c}} = \frac{3}{2}\gamma^3\omega_{\mathrm{B}}\sin\alpha = \frac{3\gamma^2 eB\sin\alpha}{2mc} \tag{2.3.3}$$

,where α is the pitch angle, the angle between field and velocity. If a power-law distribution of electrons is assumed the superposition of the synchrotron spectra result in a power-law spectrum (see Fig. 2.3). Since the electrons will have velocity components parallel to the magnetic field, too, the resulting trajectory of the electron will be a helical motion around the magnetic field **B**. The power law shape of the spectrum can be described by a spectral index α:

$$S_\nu = \nu^\alpha \tag{2.3.4}$$

Observations show a turn-over in the synchrotron spectrum. This is due to frequency dependent absorption processes. The synchrotron photons can be absorbed in the emitting electron plasma itself, this effect is called *synchrotron self-absorption*. The resulting spectrum depends on the energy of the photons and with that is frequency dependent:

$$P_\nu \propto \begin{cases} B^{-\frac{1}{2}}\,\nu^{\frac{5}{2}} & ; \quad \text{low frequencies} \\ \nu^{-\alpha} & ; \quad \text{high frequencies} \end{cases} . \tag{2.3.5}$$

The turn-over frequency, also known as *synchrotron self-absorption frequency*, denotes the frequency at which the optical depth becomes 1:

$$\tau_\nu(s) = \int a_\nu(s')\mathrm{d}s' = 1\ . \tag{2.3.6}$$

If the optical depth is $\tau_\nu > 1$ the plasma is optical thick, or opaque, whereas $\tau_\nu < 1$ mean optically thin, or transparent to radiation. $a_\nu = \nu^{-\frac{p+4}{2}}$ is called the absorption coefficient, in this case for synchrotron self-absorption, where p denotes the electron spectrum.

As the jet expands, when traveling outwards, the optical depth decreases. At the location in the jet where $\tau_\nu = 1$ the jet becomes visible. This part is called *core* and is frequency dependent as the synchrotron self-absorption is frequency dependent. Observing at different frequencies will therefore result in different locations of the core, this effect is known as *core-shift*. As higher the frequency as less synchrotron self-absorption is expected. By measuring the core-shifts the spectral shape can be analyzed and with that absorption mechanisms can be examined. As a spectral index of $\alpha \leq -2.5$ is an indication for external absorption, it can be found out whether absorption mechanisms beside synchrotron self-absorption are observed (e.g. free-free absorption in a torus Kadler et al. (2004)).

2.3.2. Beaming and superluminal motion

The outflows that can be observed in extragalactic jets are moving at relativistic speeds. That leads to the conclusion that the orientation of the jet to the line of sight has an effect on the observed motion. The further the viewing angle is away from 90 degrees, the stronger "beamed" is the apparent motion.

This can have basically two effects. One is the so called "relativistic boosting". As an emitting particle travels at relativistic speeds its emission gets boosted into the direction of movement. Additional to that its frequency gets shifted due to Doppler boosting.

By a simple Lorentz transformation of the wave factor k, as seen in Equ. 2.3.7

$$k_{\mathrm{em}}^{(0)} = \gamma\left(k_{\mathrm{obs}}^{(0)} - \frac{v}{c}k_{\mathrm{obs}}^{(1)}\right). \tag{2.3.7}$$

The observed frequency can be expressed in terms of the emitting frequency ν_{em}, its viewing angle θ and velocity relative to the observer in units of speed of light $\beta = v\,c^{-1}$:

$$\nu_{\mathrm{obs}} = \nu_{\mathrm{em}}\frac{\sqrt{1-\beta^2}}{(1-\beta\cos\theta)}\ . \tag{2.3.8}$$

From that the Doppler factor can be derived as

$$D = \frac{\nu_{\mathrm{obs}}}{\nu_{\mathrm{em}}} = \frac{1}{\gamma(1-\beta\cos\theta)}\ . \tag{2.3.9}$$

The spectrum can be approximated by a power law. In Eq. 2.3.10 the spectral index α defined through $S_\nu \propto \nu^\alpha$ was used. Finally we can use the Lorentz invariance of the flux density $S_\nu \propto \nu^{-3}$ to compare the flux densities of the approaching

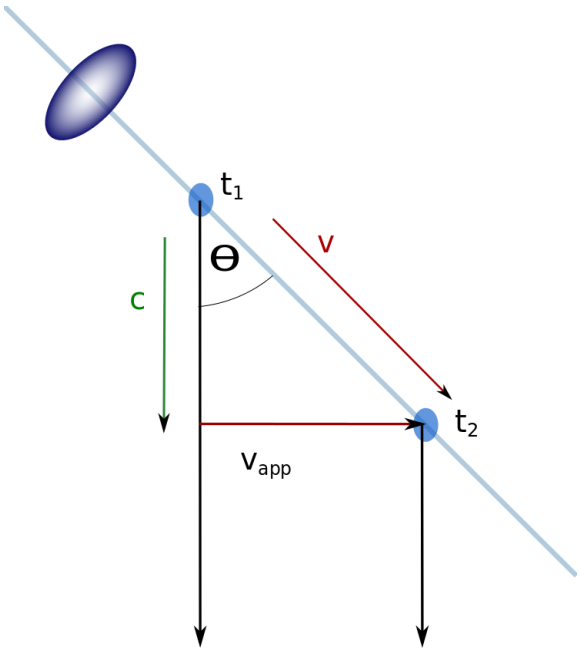

Figure 2.4.: *Superluminal motion: Seen is a "blob" traveling at speed v close to c, that emits light in instants t_1 and t_2. Due to small angle to the line of sight speeds faster than c can be observed.*

and the receding jet, called counter jet:

$$S(\nu_{\rm obs}) = D^{3-\alpha} S(\nu_{\rm em}). \tag{2.3.10}$$

For the case of a continuous jet the factor gets $2-\alpha$. These equations show that the observed flux density depends on the angle to the line of sight of the jet. As smaller the angle θ as larger becomes the Doppler factor and with that the difference between emitted and observed flux density. As the intensity of the approaching jet increases, that of the receding one decreases and in the extreme case only one jet can be observed. This opens the possibility to derive the angle of the jet to the line of sight by determining the jet-to-counter jet flux ratio through:

$$\frac{S_{\rm approaching}}{S_{\rm receding}} = \left(\frac{1+\beta\,\cos\,\theta}{1-\beta\,\cos\,\theta}\right)^{2-\alpha}. \tag{2.3.11}$$

The second effect due to relativistic motion is shown in Fig. 2.4 and is called "superluminal motion". The out moving material, called "blobs" travel with the velocity $\mathbf{v}$. But due to the inclination angle θ the apparent velocity $\mathbf{v_{app}}$ (in that case that of the proceeding jet) gets higher as:

$$v_{\rm app} = \frac{\Delta s}{\Delta t} = \frac{v\sin\,\theta}{1-\beta\cos\,\theta}\,. \tag{2.3.12}$$

Facing above equations, by determining the apparent velocity the angle to the line of sight can be derived out of the flux ratio. The usually used method for this is shown in Chapter 4 for the target source NGC 1052.

2.3.3. Temperatures in radio astronomy

Radio astronomers like use temperatures to express observational quantities. This way the power can be related to the temperature a blackbody would have if radiating the power per frequency interval and unit area. The characteristic spectrum a blackbody radiates is given by the Planck formula:

$$u_\nu\,{\rm d}\nu = \frac{2\,h\nu^3}{c^2}\frac{1}{e^{h\nu/kT}-1}\,{\rm d}\nu \tag{2.3.13}$$

where u_ν is the power per unit area per unit frequency interval and $h = 6.626\times10^{-34}\,{\rm J\,s}$ the Planck constant. The Rayleigh-Jeans approximation to the Planck formula gives the power assuming low frequencies. Including an amplifying factor g^2, as is the case for the received power, one gets:

$$P = g^2 k_{\rm B}\,T\,\Delta a\nu. \tag{2.3.14}$$

With this formula it is possible to define a *system temperature* $T_{\rm sys}$ and an *antenna temperature* $T_{\rm ant}$, with corresponing powers $P_{\rm sys}$ and $P_{\rm ant}$. $T_{\rm ant}$ represents the power of the source of interest and $T_{\rm sys}$ gives all noise terms from the receiver, the antenna and everything else that is around, like atmosphere or galactic background.

A radio image can be approximated by a model of 2 dimensional Gaussian shaped functions fitted directly to the data with FWHMs $a_{\rm min/maj}$. The resolution of an image can be defined with the so called beam, that depends on the observing telescope and frequency. Another quantity in use is the brightness temperature. Following Kovalev et al. (2005) it can be defined as

$$T_b = \frac{2\ln 2}{\pi k_b}\frac{S_{\rm core}\lambda^2(1+z)}{a_{\rm min}a_{\rm maj}}, \tag{2.3.15}$$

where $S_{\rm core}$ is the flux density of the core and $a_{\rm min/maj}$ are the FWHMs of the Gaussian component in direction of the beam axes.

The brightness temperature gradient along the jet axis can be approximated by a power-law $T_b \propto r^s$ with the power-law index $s = l + n + b(1 - \alpha_s)$ as can be seen in Kadler et al. (2004). b is the scale factor for the magnetic field. α_S is the spectral index for the initially injected electrons, l gives the jet diameter along the jet axis and n scales the electron energy density along the jet axis.

2.3.4. Final remarks on the models following Königl and Blandford

As was shown in the previous sections most of the observed quantities can be described with a power law. Blandford & Königl (1979) derived possible quantities of the power law parameters as described by Kadler et al. (2004) depending on the initial assumptions of the jet geometry. As a conical jet is assumed, the index describing the jet opening angle is $l = 1$. By giving more flexibility to the initial conditions, as taking into account that different regions of the jet can have different spectral indices, Königl (1981) gave a wider range of possible values for the spectral indices. Table 2.1 summarizes the given values following Blandford & Königl (1979) and Königl (1981) respectively.

Table 2.1.: *Values for the power law spectral indices*

power law index	Blandford & Königl (1979)	Königl (1981)
b	-1	$-1 \geq b \geq -2$
α	-0.5	$0 \geq \alpha \geq -1$
n	-2	$-0.6 \geq n \geq -2$
l	1	1
s	-2.5	$-1.4 \geq s \geq -3$

2.4. The LINER galaxy NGC 1052

Table 2.2.: *selected properties of NGC1052; Notes:* [a] *Denicoló et al. (2005)* ; [b] *listed by NED (Nasa extragalactic database) with* $H_0 = 71\,\mathrm{km\,s^{-1}\,pc^{-1}}$; [d] *Ho et al. (1997);* [e] *Beasley et al. (2002)*

Coordinates (J2000):	RA $02^h41^m04^s.7985$, DEC $-08°15'20''.751$ [e]
Redshift:	0.00537 [a]
Distance:	19.6 Mpc [b]
Linear scale:	$0.095\mathrm{pc\,mas^{-1}}$ [b]
Spectroscopic type:	LINER [d]

At large scales the radio-image of the radio-loud AGN NGC 1052 at 1.4 GHz (with the VLA) reveals two lobes spanning over 3 kpc and a dominant central feature ((Wrobel, 1984)). Its distance of 19 Mpc makes it one of the closest AGNs in our direct neighborhood. Compared to other near AGNs like M 87 and Cen a it is a small system, but the orientation of its twin-jet is close to the line of sight. Consequently, the center of emission can be constrained directly out of the image. NGC 1052 has a black hole mass of $M \sim 10^{8.2}\,M_\odot$. Due to its strong emission lines in the optical spectrum it was classified as a LINER galaxy (prototypical LINER galaxy) ((Mayall, 1939),(Fosbury et al., 1978),(Ho et al., 1997)). Kellermann et al. (1998) derived at 15 GHz a luminosity of $1.3 \times 10^{23}\mathrm{W\,Hz^{-2}}$.

In Fig. 2.6 one can see, that at higher frequencies, starting at 8.4 GHz, a new component B occurs. At lower frequencies this region is totally free-free absorbed. The center of the AGN is thought to be between component A and B. As going to higher frequencies the absorption gets smaller and disappears totally at 43 GHz. This was found by Kadler et al. (2004) who analyzed the source at 5, 8.4, 22 and 43 GHz. The "core" is the position at which the jet becomes optically thin. The distance of the core from the center is frequency dependent and is given by $r_c \simeq \nu^{-\frac{1}{k_r}}$, for a conical jet geometry, where k_r depends on the spectral index α, and the power law indices b and n for the magnetic field and the

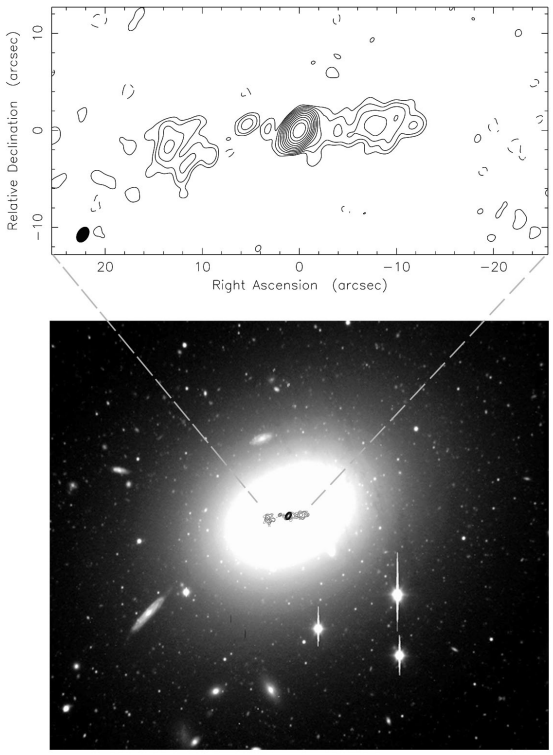

Figure 2.5.: *Comparison of the optical image (bottom) to the radio. Credit: Forbes et al. (2001), Kadler et al. (2002)*

density of the emitting particles, respectively (see, e.g. Lobanov (1998)). For large k_r synchrotron self-absorption can not be the only process leading to an absorption of the synchrotron emission. For the eastern jet Kadler et al. (2004) derived k_r to be 3.9 ± 0.8 above 22 GHz and for the western jet k_r is with 6.8 ± 2.7 between 22 GHz and 43 GHz even higher. These values can be explained by a large fraction of free-free absorption in the western jet and a small fraction in the eastern jet. The already mentioned spectral index $\alpha\,(S \propto \nu^{\alpha})$ was derived. For the core of the western jet a spectral index well above 2.5, the theoretical upper limit for synchrotron self-absorption, was achieved. These results support the analysis of Kellermann et al. (1999) and Vermeulen et al. (2003) leading to free-free absorption in the central region.

Vermeulen et al. (2003) conducted VLBI kinematic studies at 15 GHz. The structure of the two jets can be described by a large number of two-dimensional Gaussian components with an outward motion of nearly the same speed of about $\beta = 0.26$ ($\mathrm{H_0} = 65\,\mathrm{km\,s^{-1}Mpc^{-1}}$).

More recent analysis by Böck (2012) supports these results. Kinematic studies at 15, 22 and 43 GHz give a speed of $v = 0.230 \pm 0.011\mathrm{c}$.

By assuming an initially symmetric jet-system, the similar speeds lead to the conclusion, that beaming effects have to be very small. From that it is clear, that the jet orientation has to be very close to the plane of the sky.

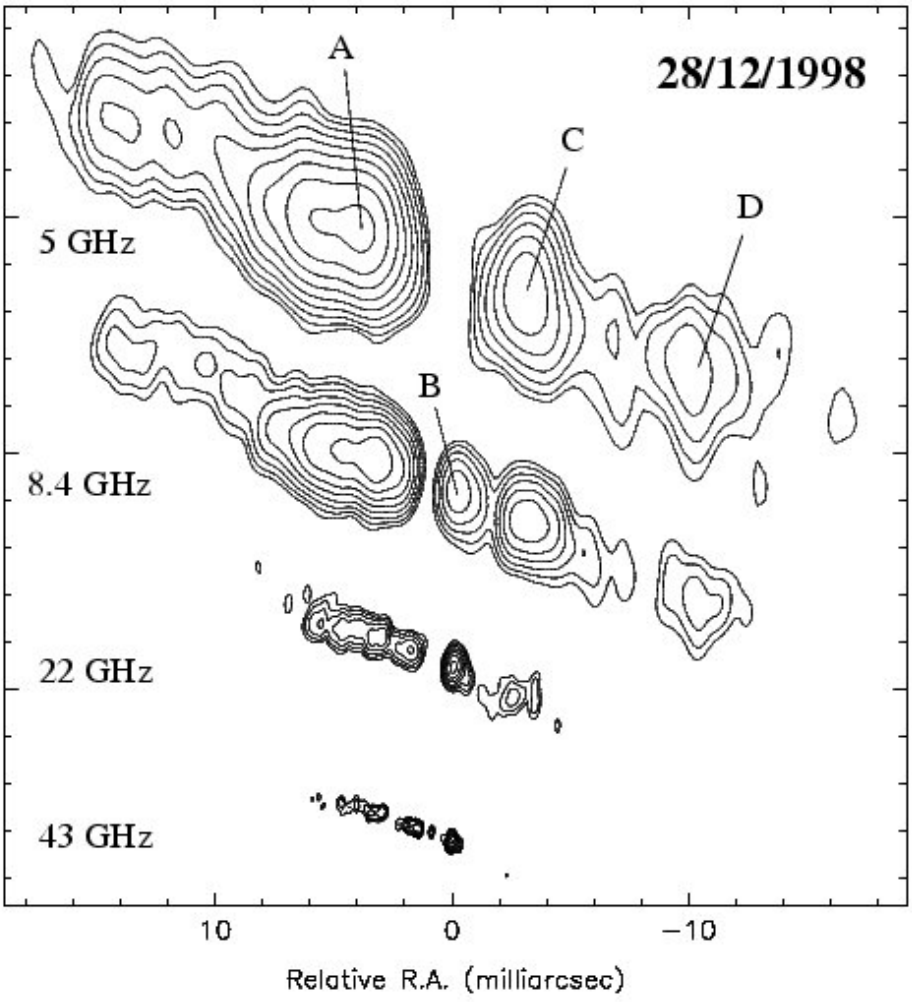

Figure 2.6.: *Comparison of the radio maps at 5, 8.4, 22 and 43 GHz. Kadler et al. (2002)*

3 | Concepts of radio interferometry

The big advantage of radio astronomy are the long wavelengths. The absorption trough the atmosphere is only small and therefore the telescopes can be located on the ground. A brief introduction on the principles of radio aperture synthesis and Very Long Baseline Interferometry (VLBI) is given. All equations and discussions in this chapter are based on Burke & Graham-Smith (2009),Thompson et al. (2001) and selected lectures summarized in Taylor et al. (1999).

Compared to optical astronomy one big advantage of radio astronomy is that we don't need any perfectly shaped mirrors or ccds to collect the incoming light and to produce a picture out of it. The signal is converted into electronic signals, what gives the chance to manipulate the received signal any time after the observation was taken. It is possible to combine data that where taken from telescopes at far distances, even if one antenna is on earth and one in outer space.

The first section will introduce basic principles to describe a single radio dish and what observational quantities are needed to describe the output of the telescope, it is based on Pacholczyk (1970). Following Clark (1999) and Thompson (1999) section 2 will discuss the mathematics behind the correlation of an electric field and how the correlation function is changed by the properties of the radio dish. Section 3 will then explain how this correlation function is actually measured wit a radio interferometer. In the end the processes needed to regain the brightness distribution out of the measured correlation function is discussed. Basic calibration strategies are described, following, e.g., Fomalont & Perley (1999) and AIPS, the program in use to calibrate the data, is presented (NRAO, 2011), with special emphasis on a technique called *phase-referencing* (see e.g. Beasley & Conway (1995)). The last steps in producing an image out of an interferometric observation are described in section 4.2, based on Briggs et al. (1999) and Cornwell et al. (1999).

3.1. Basic single dish

The simplest and cheapest possibility to receive electro-magnetic radiation at m and cm wavelength is a simple dipole antenna. It is usually used for observations at low frequencies, e.g. some tenth up to some hundred of MHz. For higher frequencies it is convenient to use a parabolic dish to collect as much radiation as possible and to focus it onto the receiver. Second possibility is per se more receptive for a by the telescope defined solid angle, this will be later known as the antenna pattern.

Assuming a source with an intensity I_ν per frequency band $\mathrm{d}\nu$, that is radiated into a solid angle $\mathrm{d}\Omega$, is observed. From that the absorbed energy of a surface element $\cos\vartheta\,\mathrm{d}\sigma$ is:

$$\mathrm{d}W_\nu\,\mathrm{d}\nu = \frac{\mathrm{d}E_\nu}{\mathrm{d}t}\mathrm{d}\nu = I_\nu \cos\vartheta\,\mathrm{d}\Omega\,\mathrm{d}\sigma\,\mathrm{d}\nu \tag{3.1.1}$$

ϑ is the angle from the normal vector of $\mathrm{d}\sigma$ to the direction of $\mathrm{d}\Omega$.

Equation 3.1.1 is the same for an emitting antenna, although in this case $\mathrm{d}W_\nu$ would be the power emitted by the antenna. It is crucial to understand, that an antenna always receives an elector-magnetic wave with the same pattern of the field distribution as would be emitted. For example a dipole antenna emits a dipole-field with a set polarization, as a result the dipole can only receive radiation with this

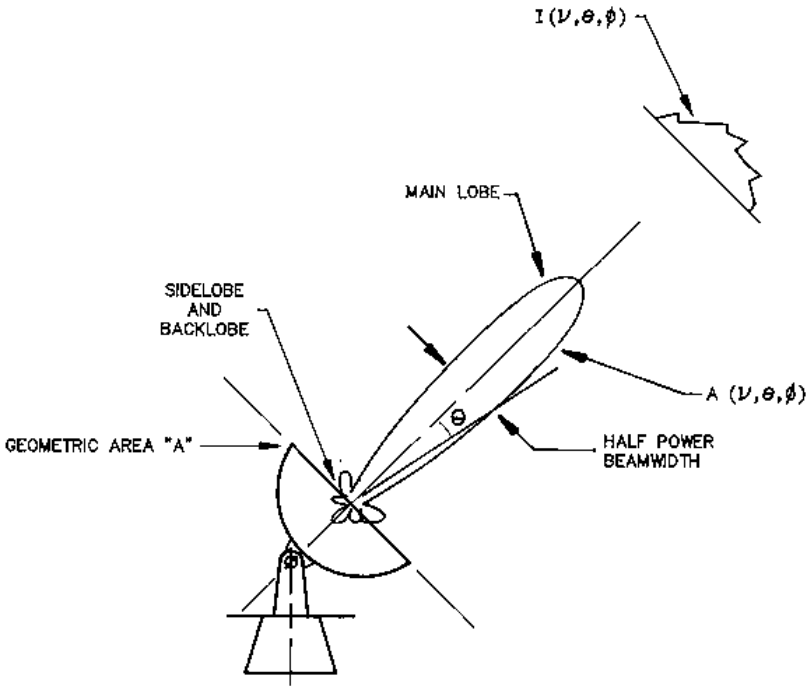

Figure 3.1.: *The beam pattern of a parabolic antenna. (Napier, 1999)*

same polarization.

Until now the receiving area $\cos\vartheta \mathrm{d}\sigma$ that receives the radiation was thought to be flat. To get closer to a more real antenna this surface element needs to be replaced by the antenna pattern P_ν times the effective area A_e. The so modified formula is shown in Eq. 3.1.2. Here the already discussed effect of polarization selection leads to an additional factor $\frac{1}{2}$.

$$W_\nu \,\mathrm{d}\nu = \frac{1}{2} A_e \,\mathrm{d}\nu \iint_\Omega I_\nu(\vartheta,\phi)\, P_\nu(\vartheta,\phi)\,\mathrm{d}\Omega. \tag{3.1.2}$$

The integration of Equ. 3.1.2, where different cases can be looked at, can be summarized as follows:

$$W_\nu \,\mathrm{d}\nu = \frac{1}{2} A_e \,\mathrm{d}\nu I_\nu \Omega. \tag{3.1.3}$$

For the case of observing an extended source with uniform brightness distribution we can set Ω to the so called *beam area* of the antenna:

$$\Omega_A = \iint_{4\pi} P_\nu(\vartheta,\phi)\,\mathrm{d}\Omega. \tag{3.1.4}$$

The pattern of the antenna can be seen in Fig. 3.1. In the case of a source with an extent much smaller than the beam area Ω can be replaced by the source size Ω_S.

All formula are given to understand the received signal of one antenna. For the end of this section I will introduce some further useful quantities that are frequently used when dealing with radio astronomical data.

Such a quantity is the apparent Flux, that is:

$$F_\nu = \iint_\Omega I_\nu(\vartheta,\phi) P_\nu(\vartheta,\phi)\,\mathrm{d}\Omega \tag{3.1.5}$$

The second often used quantity is the Brightness $I_\nu = \frac{F_\nu}{\Omega_A}$, which is normally referred to as the Flux per beam. Another possibility is to look at the Flux that is radiated by the source, simple by replacing $P_\nu(\vartheta, \phi)$ by $cos\vartheta$ in Eq. 3.1.5.

3.2. Theory of radio interferometry

Now above assumptions will be transferred to a two-element array of radio antennas. The first question that arises is what is the advantage of using two telescopes over one and what information are coming out of it. The simple answer to that is a mathematical theorem, the van Citter-Zernike theorem, that applies to any source, that is spatially incoherent. It is probably known from optics and can be transferred straight forward to radio interferometry. In that context it says, that the *spatial autocorrelation function is equal to the Fourier-transformation of the source brightness distribution.* This means, by measuring the spatial correlation function the brightness distribution can be reconstructed.

It is sufficient to express the radiation field of the source in complex quantities, i.e. the electric field $\mathbf{E}((\mathbf{r}))$. Before looking at some equations there are a few simplifications that are possible. The polarization of the field will be ignored, so the field can be expressed with a scalar quantity and it will be assumed to look only at a quasi-monochromatic component $E_\nu(\mathbf{r})$. In addition astronomical objects are normally far away so far field approximations is possible. This implies that it is impossible to observe the 3-dimensional structure of the source, but only the brightness-distribution on a sphere at some distance $|\mathbf{R}|$. At least the space between the source and us have to be empty for the moment.

All these assumptions lead to an expression of the electric field at point $\mathbf{r}$ as in Eq. 3.2.1.

$$E_\nu(\mathbf{r}) = \int \mathscr{E}_\nu(\mathbf{R}) \frac{e^{2\pi\, i\nu|\mathbf{R}-\mathbf{r}|/c}}{|\mathbf{R}-\mathbf{r}|} \mathrm{d}S \tag{3.2.1}$$

,where $\mathscr{E}_\nu$ is the projected field on the sphere.

In Eq. 3.2.3 the correlation of the electric fields defined as in Eq. 3.2.1 at the points $\mathbf{r_1}$ and $\mathbf{r_2}$ is shown. The separation $\mathbf{r_1} - \mathbf{r_2}$ is called the baseline of the two-element-interferometer. It was used, that the source is spatially incoherent, and so the factor $< \mathscr{E}_\nu(\mathbf{R_1}) * \mathscr{E}_\nu(\mathbf{R_2}) >$ is different from zero only if $R_1 = R_2$. Where the asterisk denotes a convolution.

$$V_\nu(\mathbf{r_1}, \mathbf{r_2}) =< E_\nu(\mathbf{r_1}) * E_\nu(\mathbf{r_2}) > \tag{3.2.2}$$

$$= \int < |\mathscr{E}_\nu(\mathbf{R})|^2 > |\mathbf{R}|^2 \frac{e^{2\pi\, i\nu|\mathbf{R}-\mathbf{r_1}|/c}}{|\mathbf{R}-\mathbf{r_1}|} \frac{e^{2\pi\, i\nu|\mathbf{R}-\mathbf{r_2}|/c}}{|\mathbf{R}-\mathbf{r_2}|} \mathrm{d}S. \tag{3.2.3}$$

At this point it is appropriate to introduce the unit vector $\mathbf{s} = \frac{\mathbf{R}}{|\mathbf{R}|}$, that substitute $\mathrm{d}S$ with $|\mathbf{R}|^2\Omega$, and the intensity $I_\nu =< |\mathscr{E}_\nu(\mathbf{R})|^2 > |\mathbf{R}|^2$. That leads to

$$V_\nu(\mathbf{r_1}, \mathbf{r_2}) \approx \int I_\nu(\mathbf{s}) e^{-2\pi i\nu \mathbf{s}(\mathbf{r_1}-\mathbf{r_2})/c} d\Omega \tag{3.2.4}$$

It should be pointed out that the resulting formula for the correlation function only depends on the difference $\mathbf{r_1} - \mathbf{r_2}$. The actual location of the telescopes has no impact on the so called spatial coherence function V_ν.

For the example of a two-element interferometer it is possible to keep one telescope at a specified position and changing that one of the second. This leads to a sampling of the coherence function, which can be easily done by the rotation of the earth. For an easier description it is useful to change the coordinate system in units of wavelength so that $\mathbf{r_1} - \mathbf{r_2} = \lambda(u, v, w \equiv 0)$, in this way the inverse of the baseline will be approximately the resolution in radians. For a better understanding Fig. 3.2 illustrates the now used coordinates. The third component is set to zero and the (u, v)-plane is normal

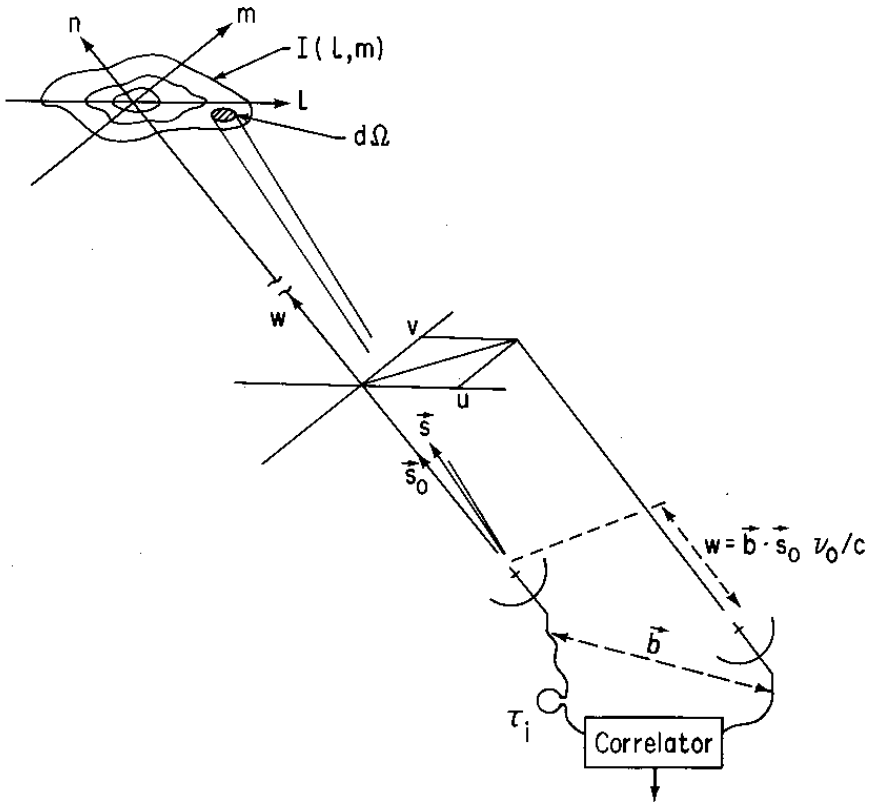

Figure 3.2.: *The two antennas are separated by the baseline-vector* **b**, *projected onto the* (u, v)*-plane. The emission from the brightness distribution I(l,m) arrives at the second antenna with a path difference* w *(Taylor et al., 1999).*

to the direction to the source, that is $\mathbf{s_0}$, above the earth. Additional, $\mathbf{s}$ have to be transformed: $\mathbf{s} = (l, m, \sqrt{1 - l^2 - m^2})$, where l and m are the direct cosines and define the coordinates of the source. It follows that in this way modified Eq. 3.2.3 becomes:

$$V_\nu(u, v, w \equiv 0) = \iint I_\nu(l, m) \frac{e^{-2\pi i(ul+vm)}}{\sqrt{1 - l^2 - m^2}} \mathrm{d}l \, \mathrm{d}m \tag{3.2.5}$$

By including a finite source size, hence the radiation only comes from a small part on the sky $\mathbf{s} = \mathbf{s_0} + \sigma$, with $\mathbf{s_0} = (0, 0, 1)$, a term $exp(-2\pi i w)$ has to be included in the above equation. The vector $\mathbf{s_0}$ is called the *phase tracking center*. By absorbing the term including w to the left hand side of the equation it follows:

$$V_\nu(u, v) = \iint I_\nu(l, m) e^{-2\pi i(ul+vm)} \mathrm{d}l \, \mathrm{d}m \, . \tag{3.2.6}$$

The inversion of the correlation function gives the *real brightness distribution*:

$$I_\nu(l, m) = \iint V_\nu(u, v) e^{2\pi i(ul+vm)} \mathrm{d}u \, \mathrm{d}v \tag{3.2.7}$$

From that it seems that all that is needed is to measure the correlation function and so it is possible to reconstruct the source of interest. But looking back at the previous section it should stand out, that the properties of the antenna are not included, yet, as well as the fact, that it is impossible ti measure the correlation function at every point of the (u, v)-plane.

First the reception pattern $\mathscr{A}_\nu(\mathbf{s})$ of the antenna should be included. Than Eq. 3.2.6 becomes

$$V_\nu(u,v) = \iint \mathscr{A}_\nu(\mathbf{s}) I_\nu(l,m) e^{-2\pi i(ul+vm)} \mathrm{d}l\, \mathrm{d}m. \tag{3.2.8}$$

$V_\nu(u,v)$ is called the *complex visibility*.

In addition, a sampling function $S(u,v) = \sum_k \delta(u-u_k, v-v_k)$ should be introduced. It is one only when data are taken. So Eq. 3.2.7 leads to the so called *dirty image*:

$$I_\nu^D(l,m) = \iint S(u,v) V_\nu(u,v) e^{2\pi i(ul+vm)} \mathrm{d}u\, \mathrm{d}v \tag{3.2.9}$$

By comparing this with Eq. 3.2.7 it should be noticed, that the *dirty image* is the convolution of the *true brightness distribution* with the synthesized beam (also known as point spread function), that is:

$$B(l,m) = \iint S(u,v) e^{2\pi i(ul+vm)} \mathrm{d}u\, \mathrm{d}v \tag{3.2.10}$$

Now everything is given to start learning how the actual observation takes place and what are the routines to make the needed deconvolution of above equations to get in the end the true brightness distribution. The quantity, that can be measured, is the complex visibility function. But therein lies the problem. For the above equations the simplest mathematical way to get to the desired equations was by using complex quantities. But complex quantities are not *measured*. So in the following section I will have a look at what the actual response of a simple two-element interferometer is to the given brightness distribution.

3.3. The two-element interferometer and beyond

A basic two-element-radio-interferometer is seen in Fig. 3.3. Assuming a planar wavefront in direction $\mathbf{s}$ arriving at the instruments, the signal at the second telescope will be delayed due to geographical circumstances as $\tau_g = \frac{\mathbf{bs}}{c}$, where $\mathbf{b}$ is the baseline, that is, related to the previous section, the spacing $\mathbf{r_1} - \mathbf{r_2}$. The output of the two combined antennas is similar to that seen in Eq. 3.1.3. The correlation

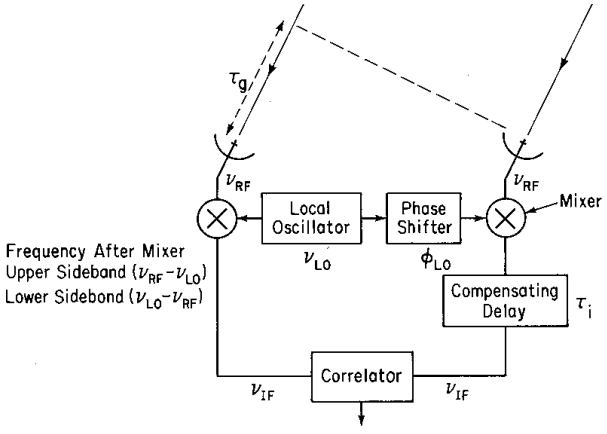

Figure 3.3.: *The signals at the two telescopes separated by b_λ arriving at different times. Before correlating these, an instrumental time delay can be inserted at one antenna (Taylor et al., 1999).*

of the two signals modulated by the fringe term $\cos(2\pi\nu\tau_g)$ is:

$$r = \Delta\nu \int_{4\pi} A(\mathbf{s}) I(\mathbf{s}) \cos\left(\frac{2\pi\nu\mathbf{bs}}{c}\right) \mathrm{d}\Omega. \tag{3.3.1}$$

In this case the problem of the antenna only to receive one polarization is ignored. The coordinate system was already changed to that in direction $\mathbf{s}$ to the source. Include again the already known phase tracking center through $\mathbf{s} = \mathbf{s_0} + \sigma$, trigonometric addition theorems are needed to get the final output of the correlator.

$$r = \Delta\nu \cos\left(\frac{2\pi\nu\mathbf{bs_0}}{c}\right) \int_S A(\sigma)I(\sigma) \cos\left(\frac{2\pi\nu\mathbf{b}\sigma}{c}\right) \mathrm{d}\Omega \tag{3.3.2}$$

$$-\Delta\nu \sin\left(\frac{2\pi\nu\mathbf{bs_0}}{c}\right) \int_S A(\sigma)I(\sigma) \sin\left(\frac{2\pi\nu\mathbf{b}\sigma}{c}\right) \mathrm{d}\Omega\,. \tag{3.3.3}$$

Combining the last equation with the already known visibility function as in Eq. 3.2.8, but written in the same coordinates as in Eq. 3.3.3, and inserting the normalized antenna pattern $\mathscr{A}_\nu(\sigma) = A(\sigma)/A_0$ results in:

$$V = |V|e^{i\phi_V} = |V|\left(\cos\phi_V - i\,\sin\phi_V\right) \tag{3.3.4}$$

$$= \int A_0 A(\sigma)I(\sigma) \left[\cos\left(\frac{2\pi\nu\mathbf{b}\sigma}{c}\right) - i\,\sin\left(\frac{2\pi\nu\mathbf{b}\sigma}{c}\right)\right] d\Omega\,. \tag{3.3.5}$$

The separation into real and imaginary parts lead to the final equation:.3.3.6:

$$r = A_0\Delta\nu|V| \cos\left(\frac{2\pi\mathbf{bs_0}}{c} - \phi_v\right). \tag{3.3.6}$$

In Fig. 3.3 the response to a point source moving through the antenna beams of a two-element interferometer is seen. The cosine fringe term from Eq. 3.3.1 gives the output fringes modulated by the primary-beam of the individual elements, that is colored red, in this case identical elements.

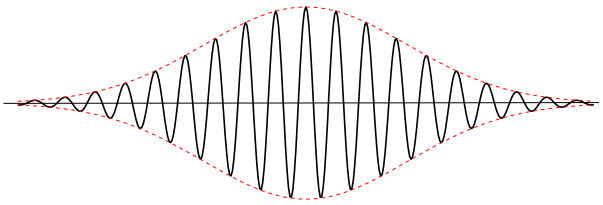

Figure 3.4.: *Fringe pattern of a 2-element radio interferometer. The sinusoidal fringe pattern is due to earth rotation (if the telescopes don't follow the source), modulated by the primary beam of the single apertures.*

All equations were only given for one frequency, but normally the observation take place including a finite passband. To understand the effect that arises, it is useful to compare it to a simple experiment known from optics, a slit. The fringe pattern behind a single slit has an amplitude modulation. As the electric field passes the slit, the resulting field is modified, due to the convolution of the incoming electric field with the shape of the slit. Since the Fourier transformation of a rectangular function is a sinc-function this is the searched modulation-function. Transferred to the signal of a radio interferometer it follows that the fringe pattern is modified by a sinc-function: $\mathrm{sinc}(2\pi\Delta\nu\tau_g)$. It follows that maximum visibility amplitude is observed by looking at the center of the sinc-envelope, the so called *delay center*. From the phase of the sinc-function we see that this is the case for zero geometrical delay. To achieve this a compensating instrumental delay has to be inserted in the signal path of the *leading* antenna, the one without geometrical delay.

The resulting effect is very similar to the already introduced modulation due to the antenna primary beam. For compensating the effect of the primary beam one has to track the source with each antenna over the sky. To compensate the effect of the bandwidth pattern one has to insert an instrumental delay.

For the end of this section I want to introduce some radio interferometric arrays. The whole discussion only looked at a two-element interferometer, but it is obvious that the best sampling function can be achieved with a big number of antennas, that are comprising the interferometer. The Fourier component of the visibility function is calculated for every pair of antennas, that means that all formula above can be applied to the case of an array of telescopes.

Figure 3.5.: *The Very Large Array (VLA); Image courtesy of NRAO/AUI.*

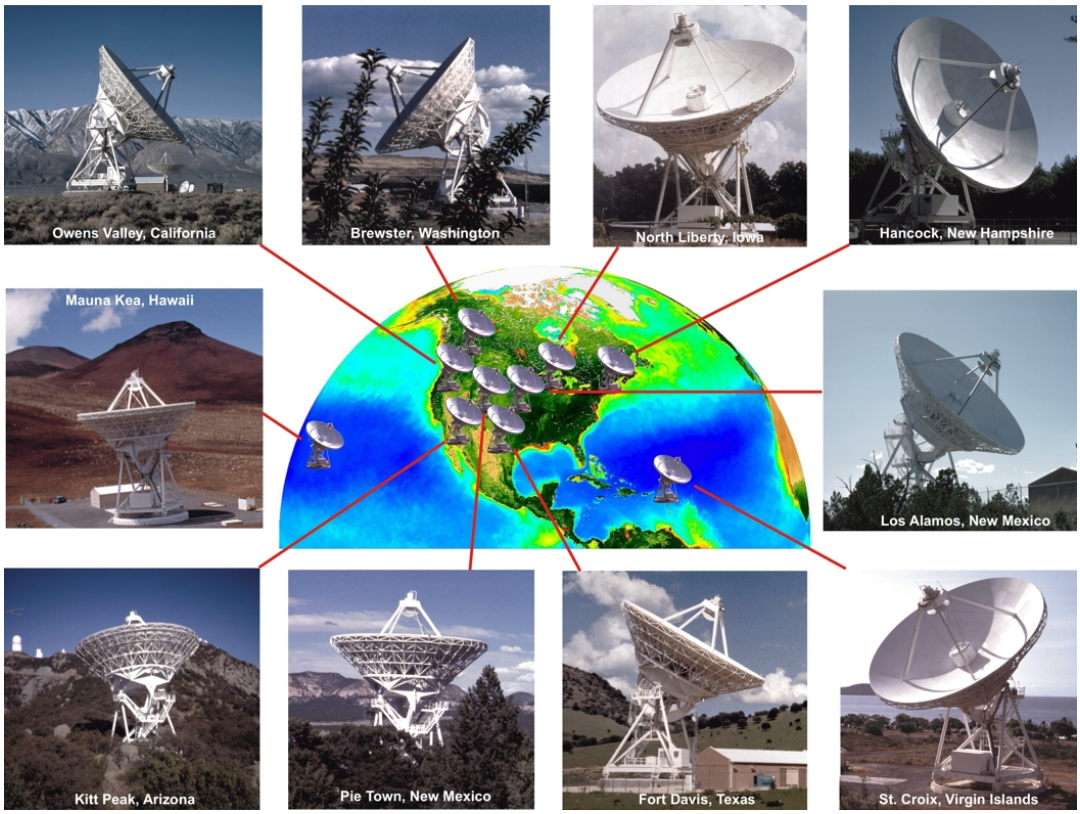

Figure 3.6.: *The Very Long Baseline Array (VLBA); Image courtesy of NRAO/AUI.*

A prominent example is the Karl G. Jansky Very Large Array (VLA) in Sorocco, New Mxico, USA,

as seen in Fig. 3.3 in its closest configuration. The array has 27 identical radio antennas with a dish diameter of 25 m. The antennas can be transported over a system of three Y-shaped rails. Different configurations with different (u, v)-coverages makes it possible to have the best possible (u, v)-coverage for the desired observation. The maximum antenna separation is 36.4 km for the widest configuration (A) and 1 km for the closest one (C).

The next possibility to go to even higher resolutions is by combining telescopes that are even farther away. For example the Very Long Baseline Array (VLBA) as seen in Fig. 3.3. It consists of 10 identical 25 m antennas on baselines up to 8000 km. Contrary to the VLA the single telescopes of the VLBA aren't connected. They are spread over the whole USA with the longest baseline from Hawaii to Virgin Islands. If an observation at the VLBA takes place, all data is saved on disk and as the observational session is finished all discs are collected at the correlation station, where the combination of the single observations take place.

3.4. Calibration of the VLBI data

3.4.1. Amplitude and phase calibration

An observation isn't perfect. There are a lot of possible errors, that modify the visibility amplitude and phase. Just to summarize some of them: Any positional inaccuracy, e.g. for the antenna position or the pointing position, will lead to additional phase offsets. The inserted delay will only correct for the geometrical delay of the delay-tracking center, but depending on the width of the passband there can occur loss of coherence. The inserted delay itself may not be set correctly and introduce an additional delay error. As there are different intermediate Frequency bands (IFs) the signal paths in the electronics can differ from one band to another and introduce phase offsets between the single bands. The correlation model may not be perfect. Until know we ignored everything that is between the source and us, but depending on the observed frequency different parts of the atmosphere have to be taken into account.

All these errors are much more difficult to solve when going from a *relatively small* connected array like the VLA to Very Long Baseline Interferometry (VLBI) like it is the case for the VLBA. As further away the telescopes are as more different is the atmosphere and ionosphere above the single antennas. Especially for high radio frequencies this can lead to the need of very good tracking of the changes of absorption and refraction coefficients of atmosphere and ionosphere.

This was just a little list of problems that can arise. This leads to the need to calibrate the data, that comes out of the correlator. The first steps (see Block Diagram 3.4.1) are made in the Astronomical Image Processing System (AIPS).

At this point we will have a look again at Eq. 3.2.8. For an array of antennas each baseline $i - j$ leads to the *true* visibility function:

$$V_{ij}(t) = \iint_{-\infty}^{\infty} \mathscr{A}_\nu(l, m) I_\nu(l, m) e^{-2\pi i(u_{ij} l + v_{ij} m)} dl\, dm. \tag{3.4.1}$$

But the *observed* visibility is a modification of the *true* one as

$$\tilde{V}_{ij}(t) = \mathscr{G}_{ij}(t) V_{ij}(t) + \epsilon_{ij}(t) + \eta_{ij}(t), \tag{3.4.2}$$

where $\mathscr{G}_{ij}(t)$ is the baseline-based complex gain, $\epsilon_{ij}(t)$ the baseline-based complex offset and $\eta_{ij}(t)$ the stochastic complex noise. We can assume that the errors of one baseline are only due to errors from one of the antennas of this baseline and doesn't depend on any other antenna.

In the perfect case the inserted delay cancels out the geometric delay of the phase tracking center fully. It follows that structural information of the Brightness distribution lie in the measured phase difference. Because of that it is difficult to find phase offsets in the target sources visibility data. That is the reason why a calibrator source needs to be observed in most cases. Ideally the flux and position of that are very well defined. By measuring at least once at the observation one phase calibration source,

its position can be referenced to the sources position in the visibility data. All errors in delays can be tracked with the strong calibration source. Since the errors should most probable be the same for the target source the correction done on the calibrator can be transferred to the source of interest. This is especially very important if the source is weak or differ a lot from a point source.

There are at least two possibilities to correct for delay errors. One could insert an additional delay to the correlator data, until the maximum in coherence is reached. The second opportunity is to look at the impact a delay offset has on the phase. When looking at phase versus frequency a slope will be seen due to a delay error. This slope can be fitted and so the phase can be flattened.

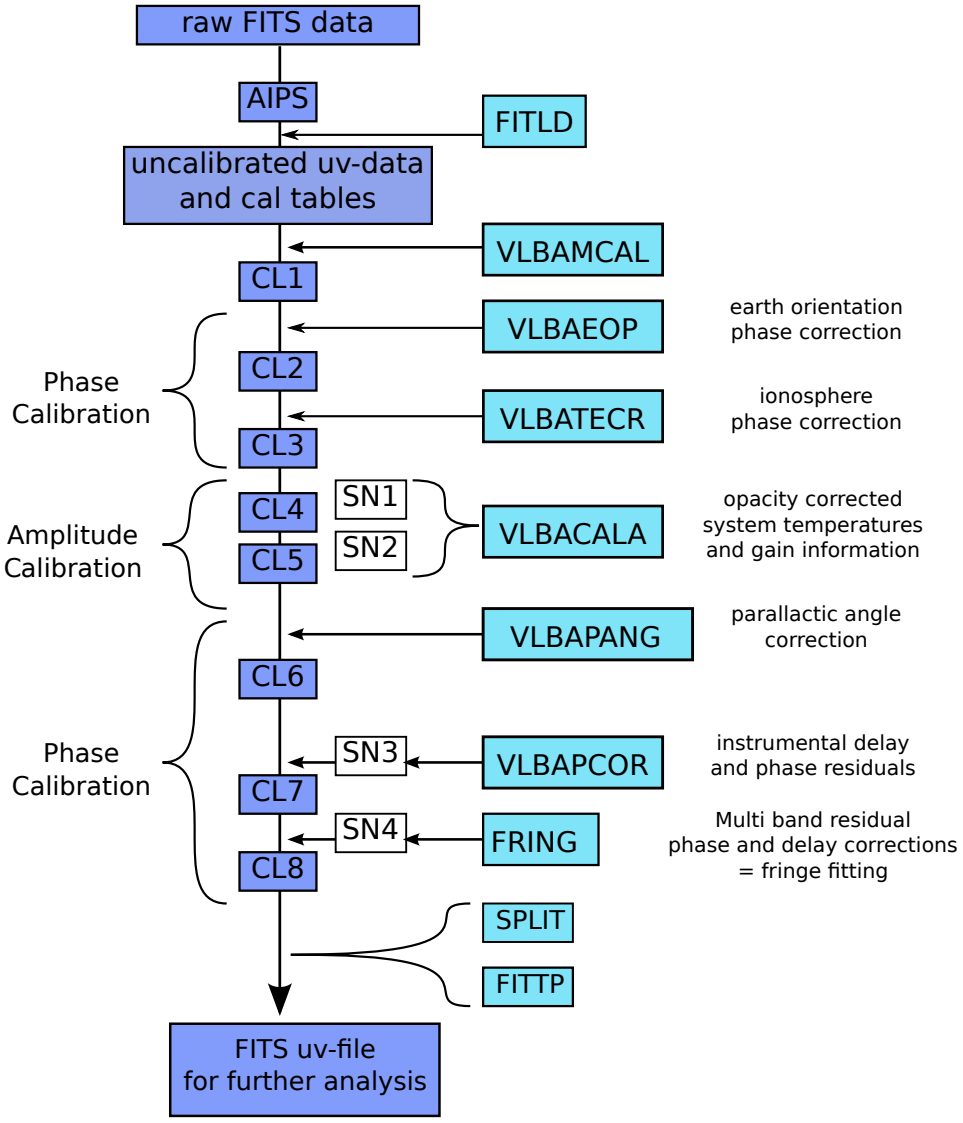

Figure 3.7.: *Block diagram of the calibration routine that is done in AIPS*

In the following I will shortly summerize the steps that need to be applied in AIPS for a proper calibration of the data. It was already explained that there are a lot of problems that lead to additional delays. Since the phase is connected to the delay as $\phi_{\mathrm{corr}}(t,\nu) = 2\pi\nu\Delta\tau(t)$ a delay error will result in a phase error. All errors in the correlated phase can be summarized as in Eq. 3.4.3

$$\phi_{\mathrm{corr}} = \phi_{\mathrm{V}}(t,\nu) + \phi_{\mathrm{inst}}(t,\nu) + \phi_{\mathrm{geom}}(t,\nu) + \phi_{\mathrm{atm}}(t,\nu) + \phi_{\mathrm{iono}}(t,\nu). \tag{3.4.3}$$

ϕ_V is the true visibility phase, ϕ_{inst} the sum of all residual instrumental phase error, ϕ_{geom} the residual error due to imperfect calculation of source and antenna position and ϕ_{atm} and ϕ_{iono} are the residual errors due to different path length of the signal in atmosphere and ionosphere at the single antennas.

To correct for all these possible errors the correlated data will pass a whole series of single correcting algorithms. The corrections that must be applied depend on the observational task. For example it depends on the observed frequency whether the different constituents of the atmosphere have a big impact on the correlated visibility phase or amplitude. For greater frequency bands the passband model needs to be as accurate as possible and was probably not modeled correctly in the correlation model. Since it would take a long time to introduce every possible calibration step I will introduce only the calibration that was applied to the observation that was analyzed in this thesis. A more comprehensive introduction can be found in Taylor et al. (1999), or in the AIPS COOKBOOK (NRAO (2011)) for the different calibrations strategies and routines that can be followed in AIPS.

The raw visibility data is loaded into AIPS, meaning the data that directly comes out of the correlator. Depending on the observing array there may to be applied array specific corrections in the beginning. These are mostly to get the data in a form that is correctly interpreted by AIPS. The data in AIPS is organized in catalogs. Each catalog is a single data file and each catalog consists of a collection of tables. For example the first catalog entry is the input data file including the whole observation inclusive all calibrator sources, in it the results from every calibration steps are saved in the form of attached tables. The second and third catalog entry may be produces after the whole calibration is finished and consists of single source data, e.g. the target source and one calibrator source.

AIPS is a collection of a lot of different small programs, that are called *tasks*. Every task has parameters that control the input data to the task and how the output data will be manipulated, these parameters are named *adverbs*. For example there are a lot tasks that are meant to examine different aspects of the visibility data, e.g. *POSSM* plots the the visibility phase and/or amplitude versus frequency, that gives the chance to look for fringe rates in the visibility phase. The last group of a sample of commands are *verbs*, that have only a small number of input parameters. An important verb is *prthi*, it shows the history that is saved to the catalog file. In it every task that was applied until then is listed, including the adverbs that were set. The verb *imh* prints an overview on the loaded catalog (that is selected by the use of the verb *getn xx*, were *xx* is the number of the catalog entry) and its attached tables. An example of the observation BR099G at 43 GHz, after the pre-calibration steps were finished, is shown in the following:

```
 >imh
AIPS 1: Image=MULTI     (UV)         Filename=BR099G_Q    .UVDATA.   1
AIPS 1: Telescope=VLBA               Receiver=VLBA
AIPS 1: Observer=BR099               User #=   12
AIPS 1: Observ. date=13-NOV-2005     Map date=23-JUL-2014
AIPS 1: # visibilities    101611     Sort order  TB
AIPS 1: Rand axes: UU-L-SIN  VV-L-SIN  WW-L-SIN  TIME1  BASELINE
AIPS 1:            SOURCE  FREQSEL  INTTIM  GATEID  CORR-ID
AIPS 1: ----------------------------------------------------------------
AIPS 1: Type    Pixels   Coord value     at Pixel     Coord incr   Rotat
AIPS 1: COMPLEX      3   1.0000000E+00       1.00  1.0000000E+00    0.00
AIPS 1: STOKES       1  -2.0000000E+00       1.00 -1.0000000E+00    0.00
AIPS 1: FREQ        16   4.3185521E+10       0.53  5.0000000E+05    0.00
AIPS 1: IF           8   1.0000000E+00       1.00  1.0000000E+00    0.00
AIPS 1: RA           1    00 00 00.000       1.00       3600.000    0.00
AIPS 1: DEC          1    00 00 00.000       1.00       3600.000    0.00
AIPS 1: ----------------------------------------------------------------
AIPS 1: Coordinate equinox 2000.00
AIPS 1: Maximum version number of extension files of type HI is   1
AIPS 1: Maximum version number of extension files of type FQ is   1
```

```
AIPS 1: Maximum version number of extension files of type AT is   1
AIPS 1: Maximum version number of extension files of type CT is   1
AIPS 1: Maximum version number of extension files of type OB is   1
AIPS 1: Maximum version number of extension files of type AN is   1
AIPS 1: Maximum version number of extension files of type CL is   8
AIPS 1: Maximum version number of extension files of type CQ is   1
AIPS 1: Maximum version number of extension files of type GC is   1
AIPS 1: Maximum version number of extension files of type IM is   1
AIPS 1: Maximum version number of extension files of type MC is   1
AIPS 1: Maximum version number of extension files of type PC is   1
AIPS 1: Maximum version number of extension files of type SU is   1
AIPS 1: Maximum version number of extension files of type TY is   1
AIPS 1: Maximum version number of extension files of type WX is   1
AIPS 1: Maximum version number of extension files of type NX is   1
AIPS 1: Maximum version number of extension files of type SN is   4
AIPS 1: Maximum version number of extension files of type PL is   1
AIPS 1: Keyword = 'OLDRFQ  '  value =  2.22104900D+10
AIPS 1: Keyword = 'SUBARRAY'  value =            1
```

In the beginning all the important information about the observation is listed, as the observing telescope (in this cas the VLBA), the date of the observation, the number of used intermediate frequencies and so on. In the second half all tables that are attached to the catalog file are given. The most important one are the history file (HI), that is read out by *prthi*, the antenna file (AN), in which all used antennas with names and coordinates are saved, the calibration tables (CL) and the solution tables (SN). The first CL table contains the initial visibility data that comes out of the correlator. Each following CL table is comprised of the initial visibility data, but with some calibration applied. The SN tables are produced by some task, e.g. *FRING*, that applies a fringe fitting to solve for delays and rates, these solutions are written to a solution table. This SN table can then be applied to a CL table i to produce a new CL table $i+1$. That is done with the task *CLCAL*. There are a lot of advantages in this approach. The user can decide what set of SN tables is to be applied, from what calibration source the solutions should be used and to what sources the solutions should be applied. It can be specified that the solutions should only be calibrated of a certain time range or only a subarray of the antennas. For a lot of calibration steps there will not be solutions for the time or frequency, etc. of every data point. CLCAL will have to interpolate solutions to solve every data point. There are different algorithms for this, depending on what it is to be calibrated a certain algorithm will be the best choice. For example if the phase differences are greater than 180 degree, there will occur phase ambiguities. In that case a linear phase connection using the rates would be much more useful than only using the phases itself, what wouldn't account for these ambiguities.

In the following I will introduce the steps that were made in AIPS as seen in Fig. 3.4.1 to correct the visibility data of the data set that was analyzed in this thesis. The darker blue blocks list all created CL tables and the bright blue blocks indicate the used tasks to get a new CL table. For all steps it is indicated whether the applied tasks corrects for the visibility phase or amplitude. Since the observation that was the scope of this thesis was made with the VLBA, the task package programmed for the VLBA was used.

After the data a read into AIPS, there were applied some corrections needed to be done for the VLBA with **VLBAMCAL**, it removes redundant calibration records. Then the actual calibration starts.

VLBAEOP fixes the earth orientation parameters. The geometric delay had to been compensated in the correlation process. For that the rotation of the earth had to be known very precisely, but it is likely that the model for the earth rotation wasn't perfect or in the extreme case wrong. VLBAEOP corrects for the errors that were introduced in the first place. This is especially very important for any astrometry or phase referencing projects.

VLBATECR may be applied to correct for delays that were introduced in the ionosphere. For that information on the electron content in the ionosphere are used. Whether this is useful or not depends on the observing frequency, the low frequency (up to some GHz) are mostly influenced.

VLBACALA corrects the visibility amplitude. It applies the tasks *APCAL*, that generates solutions for amplitude gain calibration and can corrects for atmospheric opacity, and *ACCOR*, corrects for errors in sampler thresholds. Especially for VLBI experiments the atmosphere can have a strong influence on the data, since the atmospheric introduced errors are different over each antenna as these are far away from each other.

The opacity is the integral over the absorption coefficient α over the high h from the observer.

$$\tau_\nu = \int_0^\infty \alpha(\nu, h)\mathrm{d}h \tag{3.4.4}$$

(see e.g. Thompson et al. (2001))

The opacity correction can be get by recording measurements of the weather at each station. By measuring the average temperature of the atmosphere T_{amb}, the receiver noise T_{rec} and the uncorrected system temperature T_{sys}.

$$\tau = \log\left(1 - \frac{T_{\mathrm{sys}} - T_{\mathrm{rec}}}{T_{\mathrm{amb}}}\right) \tag{3.4.5}$$

In the process of gain calibration the visibility amplitude will change to Jansky, that is $1Jy = 10^{-23}\frac{erg}{cm^2 sHz}$.

VLBAPANG corrects for the antenna parallactic angles.

VLBAPCOR corrects for instrumental delay and phase residuals. There can be *slopes* in the single IFs due to different signal paths through the electronics or clock offsets. To align the phases the best method is to use so called *pulse cals*. These are inserted pulse signals during the observation into the signal paths. VLBAPCOR searches these pulses and removes this way the differences between the single intermediate frequencies. If no pulse cals exists, the correction for instrumental residual phases have to be done by fringe fitting on a short calibrator scan.

FRING fitting of the data: remove global frequency- and time-dependent phase errors. It solves for group delay, phase and phase rate. The algorithm used is the *global fringe fitting* described by Schwab & Cotton (1983). The correction applied are antenna-based and all baselines could be used simultaneously. The default is needs at least three antennas for a solution. The adverbs manipulating the routine are very extensive, meaning I will not explain all possibilities. It is essential to decide how solutions are used. In principle there are three possibilities: find a single solution for each IF; find a combined solution for all IFs, find a combined solution and additional correct for multi-band delays, that is including the frequency derivative of the delay. The first method can be used to correct for single band delays if calibration with the help of pulse-cals doesn't work, the other two are used for the last process of phase correction, the global fringe fitting. Although the third possibility is the best choice.

SPLIT is used to divide the multi-source data file into single-source data sets, that can be further used to produce maps of the visibility data. **FITTP** is a task to read out the single-source data to a fits-file.

3.4.2. Imaging

When all calibration steps in AIPS are done, the image can be reconstructed. At this point the Visibility data are as far corrected as possible and we can in principle start with the Fourier inversion to get the brightness distribution of the source. All the following processes that reconstruct the brightness distribution were made in the DIFMAP software (Shepherd et al. (1994)).

It is sufficient to divide through the reception pattern of the antenna $\mathscr{A}_\nu$ at the end of the analysis.

So we will look in the following at the *modified brightness* $\mathscr{A}(l,m)I(l,m)$. Having again in mind that we measure the complex visibility only in some points of the (u,v)-plane and so introduced the sampling function, we should look at a sampled visibility function:

$$V^S(u,v) = \sum_{k=1}^{M} \delta(u-u_k, v-v_k) V^O(u_k, v_k) \tag{3.4.6}$$

,where V^O is the observed visibility function. From equations 3.2.9 and 3.4.6 we see that $I^D = \mathscr{F}V^S = \mathscr{F}(SV^O) = \mathscr{F}S * \mathscr{F}V^O$, where $\mathscr{F}$ denotes a Fourier transformation and a $*$ a convolution.
It is useful to look at the complex visibility this way since the computer has only numerical capabilities to approximate a Fourier transformation. In this case the possibilities are a *direct Fourier transformation* and the *fast Fourier transformation* (FFT).
We aren't able to reconstruct the source of interest as it is, but we can build a model that represents the source as good as possible. In the process called *imaging* one builds a model $\hat{I}$ of the source that consist e.g. of delta peaks, that represents the brightness distribution as is possible due to the resolution of the interferometer.

To be able to apply the FFT the data needs to be gridded. That is defining a rectangular matrix, of which the cells have interpolated visibility data assigned.
Additional to that the data points will be weighted. This will modify the shape of the beam, so it is for example easier to compare observations with initial different beams. There are different possibilities of weighting the data. That is the use of a taper that leads to a downgrading of the data points at the edges of the $(u.v)$-coverage. This can be for example a gaussian taper as $exp(-r^2(2\sigma^2)^{-1})$. Another possibility is the so called density function, that weights by the reciprocal of the local data density. The most used extreme kinds are the *natural weighting*, where all data points have the same weighting and so the best signal to noise ratio can be reached. *Uniform weighting* that weights $\propto 1/N(k)$ where $N(k)$ is the number of points in a specified area around the k^{th} data point.This results in less weighting of the points near $(u = v = 0)$. In the second case the highest resolution is reached.

As already mentioned we will only be able to build a model of the brightness distribution, so the this way modified discrete visibility looks as:

$$\hat{V}(u,v) = \sum_{p=1}^{N_l} \sum_{q=1}^{N_m} \hat{I}(p\Delta l, q\Delta m) e^{-2\pi i(pu\Delta l + qv\Delta m)} \tag{3.4.7}$$

, where $\Delta m, \Delta l$ are the separation of the grid elements. Before going to the deconvolution process known as *CLEAN* I want to indicate that all modifications like the gridding and the weighting will have an impact also on the dirty image as well as the synthesized beam.

The CLEAN algorithm is a possibility to do the deconvolution of the data. It was introduced by J.Högbom (1974).

The process consists in principle of five steps. In the dirty image I^D the intensity peak is searched; The dirty beam multiplied with the peak strength times the loop gain (defined by the user) is subtracted from the peak position; Until the flux of the peak is below a user-defined limit the routine will continue with the first two steps; The so found model $\hat{I}(p\Delta l, q\Delta m)$ is recorded and convolved with the CLEAN beam, that is an elliptical Gaussian fitted to the central lobe of the dirty beam); last the remaining residuals of the dirty image are added to the CLEAN image. To have a better control over the algorithm so called CLEAN *boxes* are commonly used. That is defining a window in that CLEAN is allowed to search for peaks.

This model can now be used to improve the visibility data and so the resulting image more. For that we have a short look at a process called *self-calibration*. In that the archived model is used to divide the visibility data by it to construct a hopefully point-like source. The process of self-calibration is similar to the initial calibration explained before. Instead of using a calibration source the target source itself is used. Then the data are solved for the complex gains and the visibilities are corrected.

By an iterative process of building a CLEAN image and self-calibration it is possible to get a model

of the source with good signal-to-noise ratio. But one need to be careful. It is easy to interpret emission into the image that isn't there and then to calibrate the visibility data that way that the data fit well to the incorrect model. It is a good advise to only model emission that you trust in, since emission that is really there will not disappear and can be modeled in a later iteration.

3.4.3. phase referencing – characteristic features of the calibration process

The theoretical background for the described methods in this section is based on Thompson et al. (2001) and references therein, as on Beasley & Conway (1995).

As discussed in Chapter 3, the visibility function depends only on the relative distance of the two correlation points, not on their absolute position (see. (Beasley & Conway, 1995)). This distance is represented by the baseline length of two telescopes (their separation), the absolute position of the telescopes isn't needed. Meaning it is possible to sample a large part of the visibility function with the VLBA, as was used for this experiment, with the help of earths rotation and a larger number of antennas. Every error in the antennas position will therefore result in an error in the separation of the telescopes, what can be observed as an phase error.

As the source is tracked over the sky, the instrumental delay will be adjusted to met the phase tracking center. If the positions of antenna and source are perfectly met, the only remaining geometric delay results from radiation that is not located at the phase tracking center and can therefore not being corrected. This is the case for an extended source. During the calibration all parameters of errors were assumed to be antenna based, this removes every information about absolute position of the source (cf. Beasley & Conway (1995)).

As one tries to compare different epochs (i.e. different observations over time) of the same source it would be good to know how the images can be aligned. This gives a higher accuracy to all comparative analysis.

Eq. 3.4.3 showed that the error in phase can be expressed by the sum of the single errors. If the source itself is faint a strong calibrator is needed to correct for the phase offsets. For all calibration steps explained in section 3.4 but the fringe-fitting the errors can be estimated for the calibration source and then transfered to the target source. This works because of the assumption that all errors are antenna and not baseline related and the introduced delays are the same for calibrator and target source. This assumption can be met as far as the distance from target to calibration source is small enough so that both wavefronts pass the same atmospheric fluctuations and that both signals go through the same instrumental paths.

This is already a kind of phase-referencing as the phase errors are estimated for one source and referenced to another source in the hope that the errors are the same for both. The calibration was made until CL table 7 in Fig. 3.4.1, hence all calibration including instrumental corrections were applied. From that it follows that (hopefully) the residual instrumental phase error ϕ_{inst} and atmospheric phase error ϕ_{atm} are removed, as far as it is possible by modeling of the electron content in the ionosphere. The phase calibration sources for correcting instrumental delays (e.g. with the use of VLBAPCOR) are only observed at the beginning and end of an observation, since these errors are not expected to change dramatically over the observation. In principle it would be enough to observe the phase calibrator only one time of the observation, e.g. at the beginning. However, a second observation gives the chance to control that the correction wouldn't be any different for sure.

The goal of the phase-referencing analysis is to obtain a reference position to align the maps of all observations. This is archived by alternately observing the target source and a phase-referencing calibration source. The errors that needed to be corrected change during the whole observation. Therefore there need to be made more observations of the phase-referencing calibrator as before for the phase-calibrator that corrects instrumental delays. Instead of performing the fringe fitting on all sources and producing that way CL table 8 in Fig. 3.4.1 the fringe fitting will be made on the phase-referencing calibration source. The solutions will be interpolated and applied to the target source. Therefore the phase-referencing calibration source and the target source are observed alternately as can be seen in Fig. 4.6. The calibration source is e.g. observed at times t_1 and t_3 and the target source at time t_2. Using Eq. 3.4.3 the phase-errors for both sources for all three times can be expressed as in equations

3.4.8 and 3.4.9. The geometric phase error was divided into a component for the antenna and one for the position of the source. The superscript C indicates an error in the calibrator phase and a T one in the target phase.

$$\phi_{\rm cal}(t_{1/3}) = \phi_{\rm C}(t_{1/3}) + \phi^{\rm C}_{\rm pos}(t_{1/3}) + \phi^{\rm C}_{\rm ant}(t_{1/3}) + \phi^{\rm C}_{\rm inst}(t_{1/3}) + \phi^{\rm C}_{\rm atm}(t_{1/3}) + \phi^{\rm C}_{\rm ion}(t_{1/3}) \tag{3.4.8}$$

$$\phi_{\rm targ}(t_2) = \phi_{\rm T}(t_2) + \phi^{\rm T}_{\rm pos}(t_2) + \phi^{\rm T}_{\rm ant}(t_2) + \phi^{\rm T}_{\rm inst}(t_2) + \phi^{\rm T}_{\rm atm}(t_2) + \phi^{\rm T}_{\rm ion}(t_2) \tag{3.4.9}$$

The task FRING is used on the calibration source using CL table 7 to obtain solutions for the phase errors at times t_1 and t_3. Using both solutions the phases are interpolated to time t_2. The interpolated phases are indicated by $\tilde{\phi}$. For the equations 3.4.8 to 3.4.10 all phase-errors are still included, as if no calibration had happened yet.

$$\tilde{\phi}_{\rm cal}(t_2) = \tilde{\phi}_{\rm C}(t_2) + \tilde{\phi}^{\rm C}_{\rm pos}(t_2) + \tilde{\phi}^{\rm C}_{\rm ant}(t_2) + \tilde{\phi}^{\rm C}_{\rm inst}(t_2) + \tilde{\phi}^{\rm C}_{\rm atm}(t_2) + \tilde{\phi}^{\rm C}_{\rm ion}(t_2) \tag{3.4.10}$$

The in this way interpolated phase solutions at the observing time of the target source can now be subtracted from the phases of the target source:

$$\phi_{\rm target} - \tilde{\phi}_{\rm Cal} = (\phi_{\rm T} - \phi_{\rm C}) + (\phi^{\rm T}_{\rm pos} - \phi^{\rm C}_{\rm pos}) \tag{3.4.11}$$

The following approximations are made: The source structure will not change and so remains in the visibility phase. The data processing for the target source is made in the same electronics as for the calibration source, so we can set $\phi^{\rm T}_{\rm inst}(t_2) = \tilde{\phi}^{\rm C}_{\rm inst}(t_2)$. The same applies to antenna positional errors, so $\phi^{\rm T}_{\rm ant}(t_2) = \tilde{\phi}^{\rm C}_{\rm ant}(t_2)$. For the phase-referencing calibration source the same applies as for the phase-calibrators: it is essential that the calibration source is not far away from the target source. If that's the case, the atmosphere and ionosphere between the two sources and the antennas are the same, so the errors should be the same as well and we can set $\phi^{\rm T}_{\rm atm/ion}(t_2) = \tilde{\phi}^{\rm C}_{\rm atm/ion}(t_2)$.

What is left is the difference in source structure of target and calibration source, as long as the calibrator source has extended structure. The last point is not preferable, but as going to higher frequencies as closer the two sources have to be and as more difficult it is to find a point-like calibration source. Since as the frequency gets higher the resolution gets higher and the calibrator source that works for a lower frequency may now be extended. The phase information on the calibrator source structure would distort the resulting phase-referenced map. To overcome this problem it is useful to retain the source information for the calibrator source by previous self calibration and subtract it from the calibrator phase before obtaining the delay and rate solutions during fringe fitting. The source information can be achieved by following the standard routine as described in Section 3.4 and 3.4.2.

The routines described until this point are visualized in Fig. 3.8. The figure is adjusted to the phase-referencing experiment analyzed in this thesis. For the *generally* phase-referencing observation a strong calibration source would be observed and the target source is normally weaker. This would change the symbols in the block diagram, so that the calibration source would be the star and the target source the polygon. In the case of the phase-referencing observation of NGC 1052 the phase-referencing calibrator was weaker than the target source NGC 1052. Consequently the role of phase-referencing calibrator and target source was reversed. In the following I will call the star the phase-referencing calibration source and the polygon the target source.

The processes above the line indicating the end of the pre-calibration process including the production of CL table 7 are exactly the same as described in Section 3.4. Everything below the line corresponds to the procedures changed for phase-referencing. If the calibrator source is point-like the structure of the source does not have to be subtracted from the calibrator phase. In this case CL table 8 wouldn't be produced and with that the step producing SN table 5 would be skipped. After the production of CL table 7 the fringe fitting on the calibration source follows directly to produce a SN table, that would be applied to the target source to produce CL table 9. The visibility data can be read out and a phase-referenced map can be produced. At this point it is essential not to apply any kind of phase-calibration as this would remove all positional phase information and only left the structural phase information. The produced map of the target source is shifted from the image center. That shift is related to the

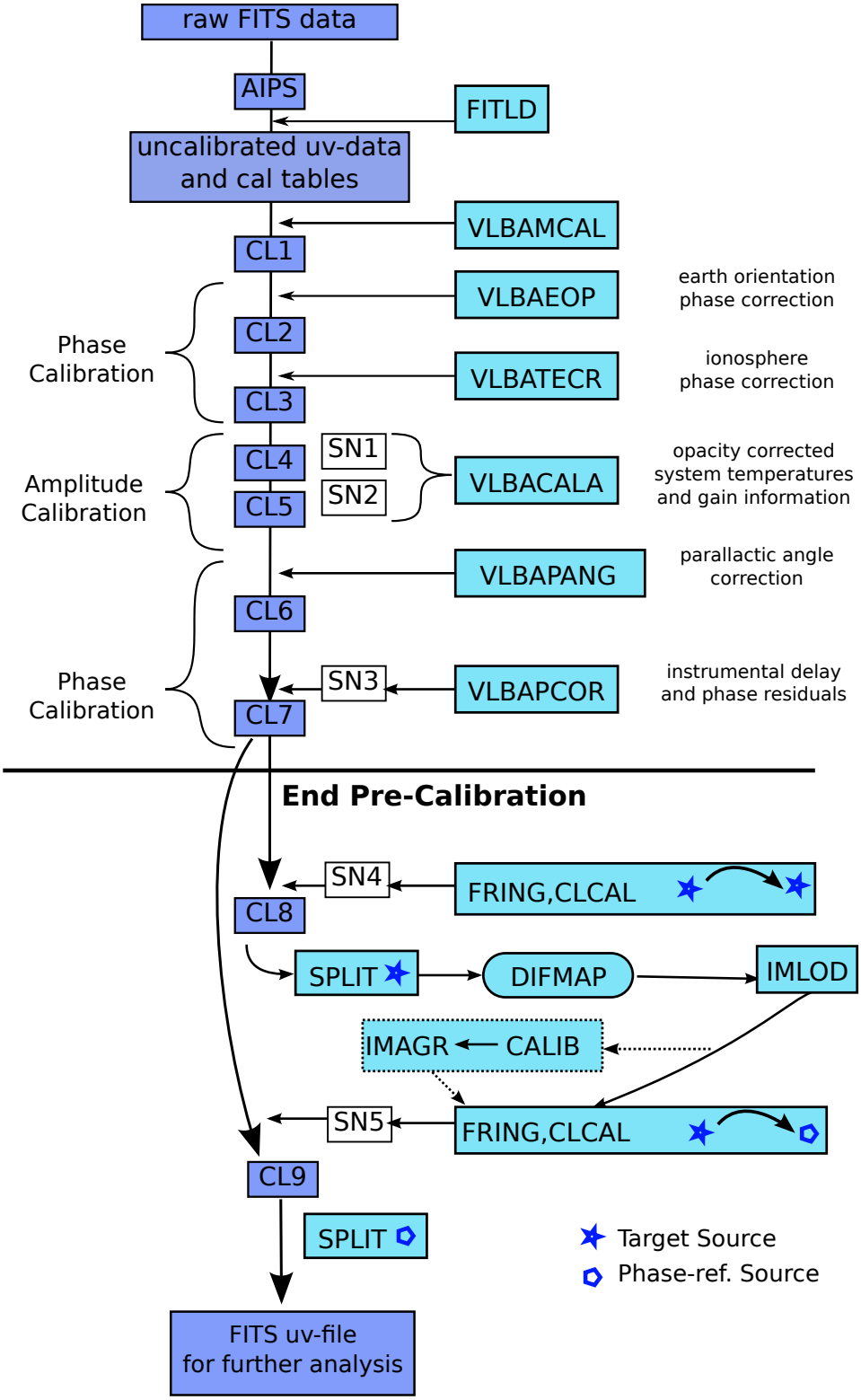

Figure 3.8.: *Block diagram of the calibration routine that is done in AIPS as is needed for phase-referencing. Before and after the whole block of alternating observations the phase calibrators where observed.*

residual phase error $\phi^{\rm T}_{\rm pos} - \phi^{\rm C}_{\rm pos}$ that is left in the visibility phase and can now be used to align the target source maps for all analyzed phase-referencing observations.

If the calibrator has an extended structure one has to follow the path producing CL table 8 and in the end SN table 5 and CL table 9. To remove the phases due to the structure of the calibrator a model of the source needs to be produced. This is in principle achieved by following the whole process as described in sections 3.4 and 3.4.2 with the exception that only *FRING* solutions for the calibrator are used. This goal can be reached by using the interpolation *self* in the task *CLCAL*. During the imaging process a map of the calibrator is produced in the program DIFMAP. This map is loaded back into AIPS with the task *IMLOD*. In principle this map could be directly used to subtract the source structure phases, what can be done with the the task FRING. To be on the safe side the imaging and self-calibration algorithms in AIPS could be used exclusively or following the process in DIFMAP. The procedure for self-calibration in AIPS is the task *CALIB* and that for imaging *IMAGR*. By including these two tasks one would assure that FRING reads the information correctly, since there would be no errors that could be introduced by converting the DIFMAP produced image to the data format used in AIPS.

4 | Results & discussion

The principles of radio interferometry and the related imaging methods were discussed in the previous chapters. In the following I will first present results from a recently calibrated data set of NGC 1052 (Baczko, 2012) at 86 GHz observed with the Global mm-VLBI Array (GMVA), that revealed a bright central feature and the first-ever detection of the twin-jet system at this band. To address the question whether the central feature is the center of the AGN a multi-wavelength observation campaign as initiated in 2005 (see e.g., (Ros & Kadler, 2008)) will be discussed.

4.1. Highest resolution image of NGC 1052 at 86 GHz

In October 2004 observations of NGC 1052 at 86 GHz (corresponding to 3.5 mm wavelength) were carried out by the Global mm-VLBI Array (GMVA). An overview of the array is seen in Fig. 4.1. Effelsberg, Pico Veleta, Plateau de Bure and Metsähovi were combined with eight antennas of the VLBA. The calibration of the visibility data in AIPS will be shortly explained (see also (Baczko, 2012)). The higher the observing frequency becomes, the more challenging is the calibration of the data, as the radiation is more influenced by atmospheric turbulences.

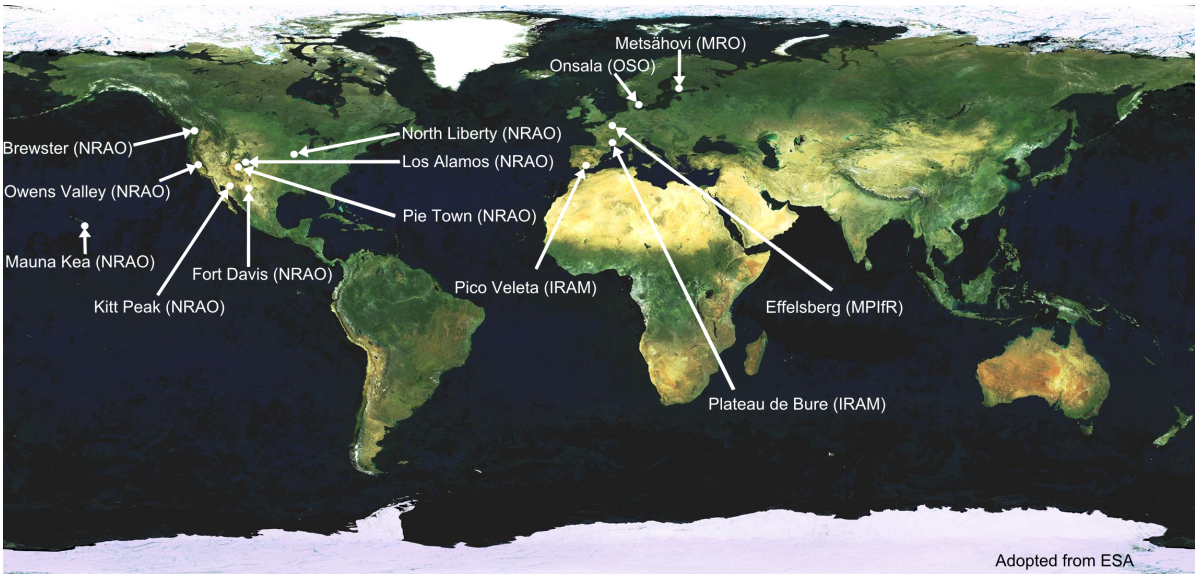

Figure 4.1.: *The Global mm-VLBI array with telescopes used for the 3 mm observation of NGC 1052.*

Given the spread of the array and the low declination of the source, the common visibility by all antennas is limited to a few hours. Fig. 4.2 shows the observing times for all used telescopes for the observed data prior to flagging and calibration in AIPS. Each observing telescope is listed and the time

of observations are indicated by dots. A small window of about 2 hours was available for telescopes in Europe and the eight available VLBA dishes for simultaneous observations.

NGC 1052 is located at a declination of −8 degrees and the array is mostly spread in the East-West direction, which results in a very elliptical beam that has a high resolution in the direction of the two-sided jet. The resulting *uv*-coverage is shown in Fig. 4.3.

4.1.1. The calibration

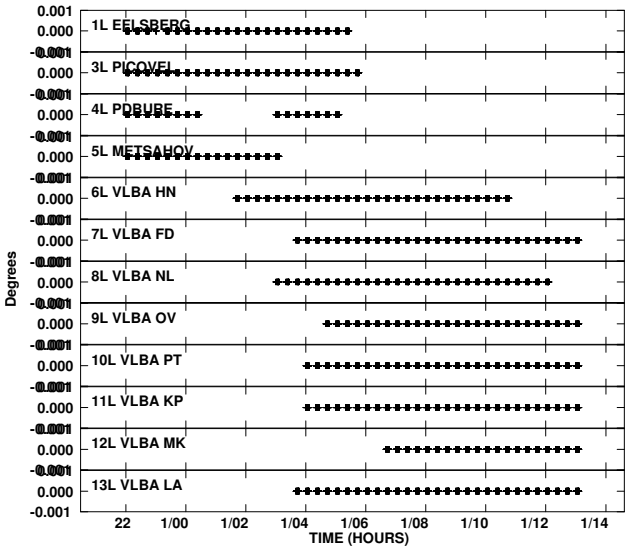

Figure 4.2.: *Plot to illustrate the time coverage of the observation for each antenna. Plotted is the phase versus the time (in units of observation days), prior to calibration*

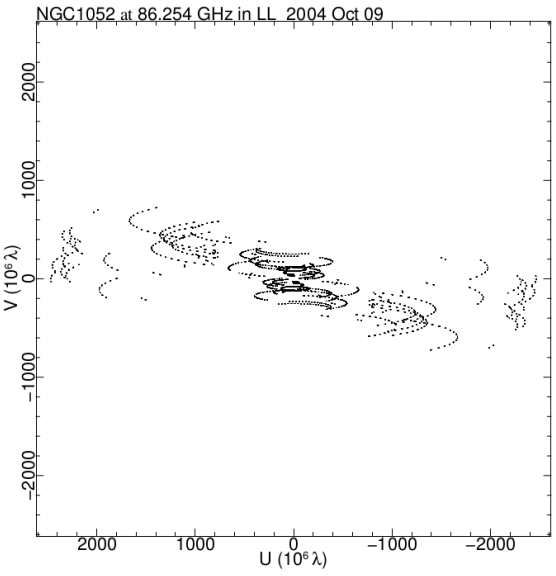

Figure 4.3.: *uv-plot of the observations of NGC1052 in our GMVA experiment. It shows interferometric data from all baselines during the observation. Each point corresponds to a given baseline at a given time.*

The calibration routine is similar to standard VLBI calibration as described in Sect. 3.4. Due to the challenges that arises at a high observing frequency of 86 GHz, standard calibration needs some modifications. The calibration strategy was based on Martí-Vidal et al. (2012). In the following I will discuss the changes that are to be applied to the block diagram 3.4.1, the diagram describing the modification procedure is shown in A.1. The principal differences are:

- The VLBA specific tasks were not used, since the array includes non-VLBA antennas.
- The amplitude correction was applied after the fringe search.
- The phase was only corrected for parallactic angles, instrumental delay, and residual phase and delay by fringe fitting, but not for earth orientation phase and the ionosphere.

The use of *pulse-cals* was not possible in this observation, since not all participating 86 GHz stations have this method implemented. In this case the sub-band correction was achieved by *fringe-fitting* on a short calibrator scan to determine the relative phase, and applied to all visibilities in the experiment. The fringe-fitting was performed on the calibration source 0235+164, since for NGC 1052 no strong fringes were detected. Another difference to standard procedures is how to address the data corresponding to the transatlantic baselines. To align all phases and delays in Europe as well as in the USA at least two reference antennas were needed and FRING was run three times to correct the single sub-bands. First on the European baselines, then on a common transatlantic baseline, and in the end on the VLBA baselines. For the first one Pico Veleta near Granada (south of Spain), for the second one Effelsberg, that is located near to Bonn (Germany), and for the third one Los Alamos in New Mexico (USA) was

used, since it is located nearly in the center of the VLBA antennas. Unfortunately, it was not possible to remove the phase slopes for each sub-band in this way. To calibrate the data a ParselTongue script was used, as described in Martí-Vidal et al. (2012). The basic ideas are the same, but an iterative process was applied to find good starting values for the delays and rates on that further analysis led to flat phases.

After this combined fringe fitting, solutions for all sub-bands were determined for all times and antennas.

The amplitude correction had to be applied again with the help of a ParselTongue script following Martí-Vidal et al. (2012), since the collected information about the weather at each antenna was not in a format that could be directly imported to AIPS. The script derived $T_{\rm rec}$ and the system temperature was corrected for opacity. The so derived values were read into AIPS and the task APCAL was applied to determine the amplitude scale of the recorded visibility data.

4.1.2. Results – the highest resolution image of the twin-jet system in NGC 1052

After the visibility data were pre-calibrated in AIPS, imaging was made in DIFMAP (Shepherd et al., 1994) as described in Sect. 3.4.2, resulting in the map as shown in Fig. 4.4. This map was produced using natural weighting to regain the maximum possible sensitivity. The highest resolution is obtained out of the uniform weighted map and results in an uniform beam of $(353 \times 58)\mu$as in position angle of $-9.33°$. This is the first time the twin-jet of NGC 1052 was detected at 86 GHz.

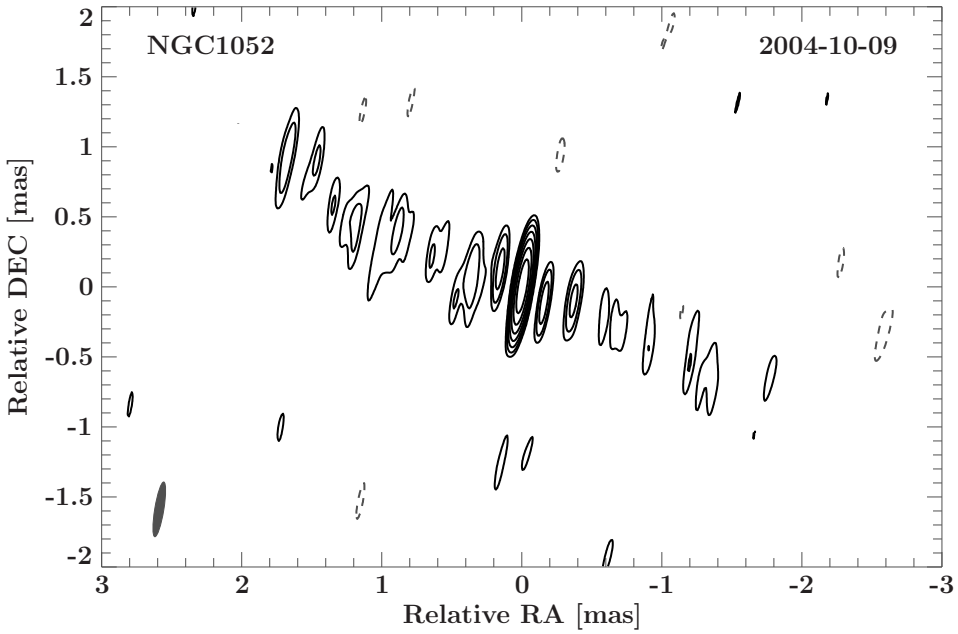

Figure 4.4.: *First detection of the double-sided jet in NGC 1052 at 86 GHz (natural weighted hybrid map).*

A fit of a two-dimensional Gaussian component to the central feature was applied, but was unresolved. A theoretical resolution limit was derived, following Lobanov (2005) with $\beta = 1$ for the uniform weighted map. The upper limit on the resolution limit along the position angle of the Gaussian central component was derived to $0.0214\,\text{mas} \times 0.0036\,\text{mas}$ to yield an upper limit of the emission region along the jet angle (64°) of $8.6\,\mu$as. That leads to a theoretical resolution of 6.2 lt-dy in east-west direction. If assuming that the central radio feature includes both jet bases, and with that the black hole, too, the distance between black hole and jet base is smaller than $25\,R_S$ (Schwarzschild radii). From that, a lower limit for the brightness temperature of the central component of $T_b > 5 \times 10^{11}$K was derived.

For studying the most compact regions in the centers of AGN the most important target is M 87, so far. It is at a distance of about 16.7 Mpc (Blakeslee et al., 2009), has a black hole mass of $6.6 \pm 0.4 10^{10} M_{\odot}$ (Gebhardt et al., 2011) and an inclination angle to the plane of the sky between 15° and 45° (Acciari et al. (2009), Ly et al. (2007)). Due to the higher mass of the central engine, the Schwarzschild radius of M 87 is larger and so the same angular distance corresponds to less Schwarzschild radii as in the case of NGC 1052. Maps of both sources with the same resolution in arc-seconds would result in a higher resolution in means of Schwarzschild radii for M 87. In addition its distance to the observer is about 3 Mpc shorter, meaning an observation at the same frequency would result in a higher spatial resolution of M 87.

However, the smaller inclination angle of M 87 leads to an one-sideness of the jets. So, the location of the central engine has to be derived, as is possible by determining the infinite-frequency location of the jet base, using the so-called core-shifts. This was done by Hada et al. (2011), who derived the central engine to be within 14-23 R_S of the core at 7 mm, assuming a conical geometry. The so defined location of the black hole supports the assumption that the faint feature seen on the eastern side of the jet (e.g. Ly et al. (2007)) is the counter-jet. Doeleman et al. (2012) observed at 1.3 mm and derived the size of the jet base to be $40 \pm 1.8\,\mu$as, what corresponds to $5.5 \pm 0.4\,R_S$. Compared to derived resolution limits for NGC 1052 the projected sizes are comparable.

This difference in inclination angle is a big advantage of NGC 1052. The line of sight is assumed to be close to 90°[1] as the flux density ratio of both jets for the 3 mm map is almost equal. Both jets are seen, even at a low wavelength of 3 mm. It follows that the location of the central black hole can be derived directly out of the image. The 3 mm-map (see Fig. 4.4) reveal both jets and one bright central feature.

To test whether the central feature is indeed the center of the system two methods are applied to the observational data at 22 and 43 GHz. One is is the so called *phase-referencing* to recover the absolute position of the images, lost during the hybrid mapping process. After this the source images at different frequencies/epochs can be aligned. The second one is a kinematic analysis to verify the location of the center from that matter is ejected.

4.2. Multi-frequency campaign – phase-referencing observations at 22 and 43 GHz

The observation of NGC 1052 took place between March 2005 and April 2009 simultaneously at 22 and 43 GHz. The experiment was conducted as a phase-referencing experiment with the VLBA. The phase-referencing calibrator was J0243−0550 and further calibrators were III ZW 2 and B0420−014. An example (u, v)-coverage of the observation BR130E at 43 GHz is seen in Fig. 4.5.

The observational strategy for phase-referencing NGC 1052 can be seen in Fig. 4.6. As was discussed in section 3.4.3 for phase-referencing the solutions for phase, delay and rate are derived for a reference source and will be applied to the target source, therefore it is needed to interleave scans in this way. The observations took place at two frequencies (22 and 43 GHz), for which the receiver in use was changed between two blocks of observation. First a block of 5 observations took place at 22 GHz, after that one block at 43 GHz then again at 22 GHz and again at 43 GHz until the end of the observational session. During each block the target and phase-referencing sources where observed alternately. NGC 1052 is indicated as the star, J0243−0550 as the pentagon. The typical observational strategy of a phase referencing experiment was changed that way as NGC 1052 was used as the phase-referencing source, since it is brighter than the calibrator source J0243−0550. This means that fringe fitting was made on NGC 1052 and the resulting solutions were applied to J0243−0550 to produce a phase-referencing map. For higher frequencies, additional delays due to the atmosphere have a big influence, that is the reason why the analysis was first done for the data at 22 GHz. After that fringe fitting at 43 GHz was challenging, thats why I will focus on the 22 GHz data in the following.

[1] Earlier studies from Böck (2012) derived a lower limit for the inclination angle to: $\theta \geq 78.8°$ out of a kinematic analysis of NGC 1052 at 15, 22, and 43 GHz.

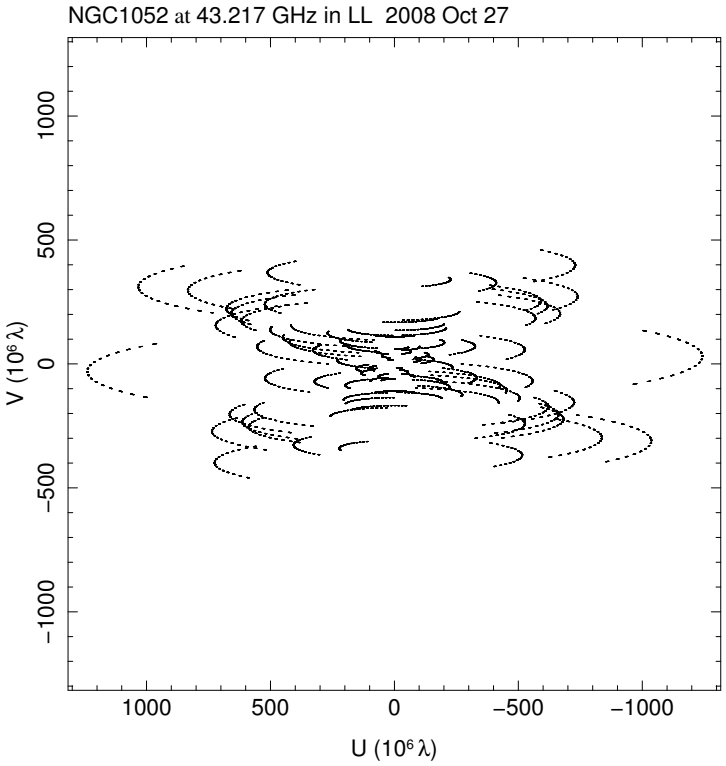

Figure 4.5.: *(u, v)-coverage of observation BR130E at 43 GHz.*

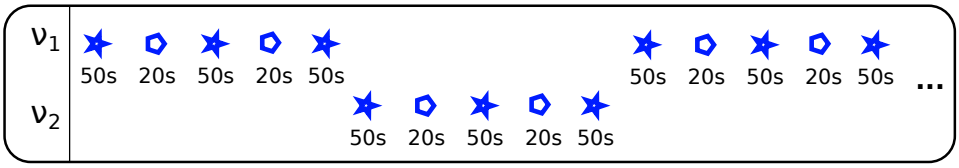

Figure 4.6.: *Strategy of dual-frequency phase-referencing observations.*

The target source NGC 1052 is non point-like so it is necessary to subtract the source structure phase from the data to obtain structure-free phases,delays and rates at the fringe fitting process. The calibration steps for this phase-referencing experiment are shown in Fig. 3.8. The first calibration steps were applied, including phase corrections due to the atmosphere, the earth orientation parameters, parallactic angles and instrumental delay and phase residuals, and the calibration of the amplitude (producing Cl table 7). At this stage fringe-fitting is the only remaining calibrations step and it is special for phase-referencing observations. NGC 1052 was used to find solutions for phase,delay and rate via FRING. As NGC 1052 is non point-like these solutions were applied to the source itself to produce a map that could be used to subtract the source structure phase from the data. For this step the calibrated visibility data were red out of AIPS to DIFMAP. A standard routine of hybrid imaging was applied, as described in Sect. 3.4.2, to produce the needed map of the source structure of NGC 1052. With the task IMLOD this image could be read back into AIPS.

With FRING it is possible to give an image to the task as input. FRING subtracts the phases due to the source structure first and then derives the solutions (following Fig. 3.8 the here produced table is SN 5). To play it safe the map from DIFMAP could be first self-calibrated again with the task CALIB and then a new map with the task IMAGR could be produced. This process should not change the structure itself but certainly the data is in a format that is correctly interpreted by FRING. The

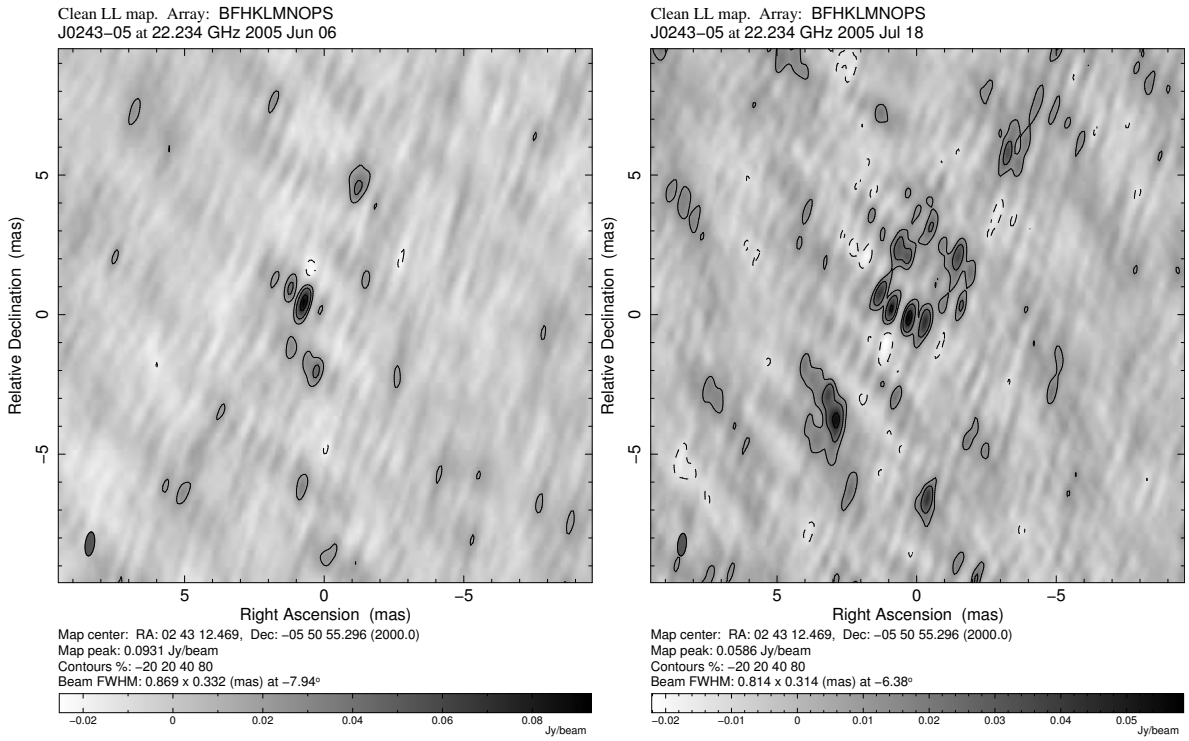

Figure 4.7.: *Phase referenced map for observation BR099C (left) and BR099D (right) without the use of clean windows.*

solutions for the phases of NGC 1052 were interpolated to the times of observation of J0243−0550 to produce the phase-referenced visibility data (CL 9).

The uv-data were read out again into DIFMAP to produce the phase-referencing map. At this point it was very important not to do any kind of phase-calibration, as this would destroy the phase-positional information due to the residual separation of the target and phase-referenced source with respect to their catalog positions used for correlation. To produce an image out of the phase-referenced visibility data three attempts of fitting the emission were applied. Two were using the CLEAN algorithm as described in the imaging process (see Sect. 3.4.2) but without self-calibration. For one of these the point-sources were fitted to the whole map, for the other areas to fit were defined by defining clean windows. The last was made by fitting a Gaussian component to the map peak. From all these methods it was possible to find the position of the peak in the map, whereas the use of clean windows should not be needed here as the phases should be calibrated good enough for phase-referencing to work. The position relative to the map center represents the residual distance between the target and phase-referencing source. To align the observations of NGC 1052, the resulting positions of J0243−0550 in RA and Dec are used to shift the images of NGC 1052 used as input for the phase-referencing. The values for the 22 GHz observation are shown in Tab. 4.1.

An example for a phase-referencing map is presented in Fig. 4.7 , the rest are presented in the appendix (see figures A.3 to A.4). Fig. 4.7 gives an impression on the quality of the phase-referenced images. For Fig. 4.8 the same uv-data as in Fig. 4.7 were used, but this time with self-calibration assuming a point-source starting model and after that ten cycles of clean and self-calibration. This shows that indeed the source structure of J0243−0550 is recovered in the phase-referenced uv-data and it proves that self-calibration removes the information on the separation of the two sources. Without the use of self-calibration the maps are very noisy. A big problem can be seen for BR099D. It is difficult to define what structure in the clean map is the main shifted peak. For the values shown in Tab. 4.1 the location of the maximum flux value where used, even if the difference was only marginal.

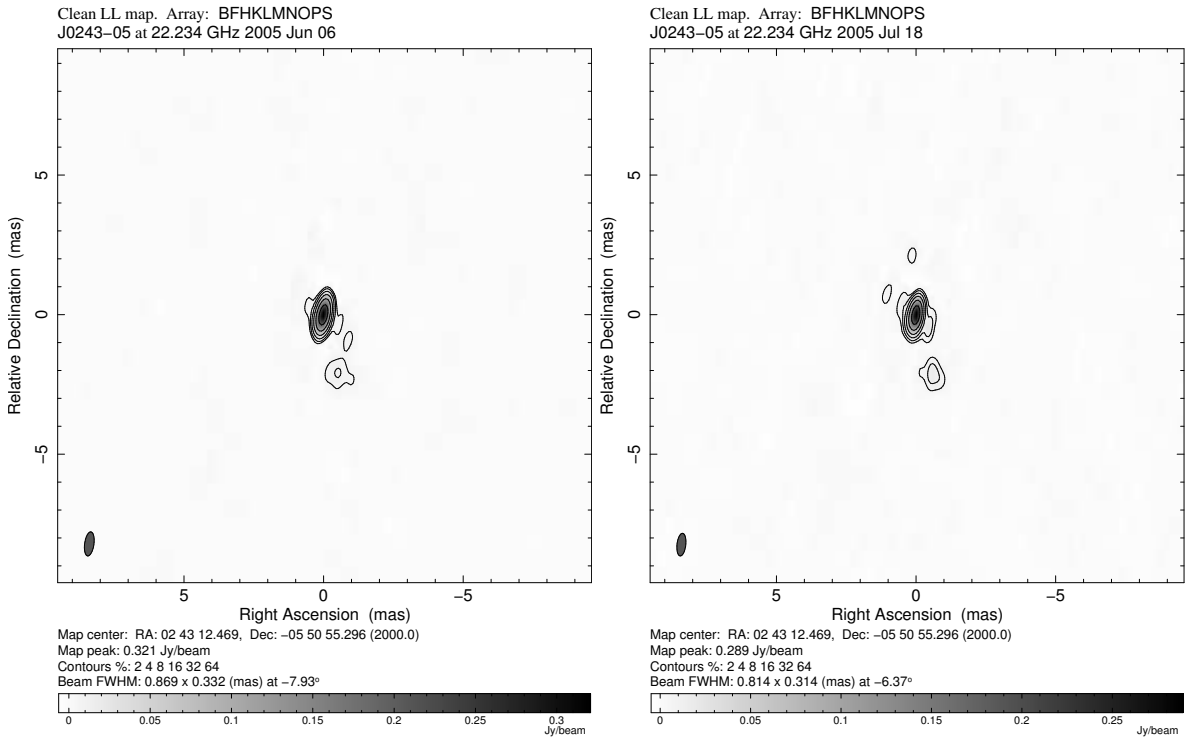

Figure 4.8.: *Self-calibrated images for observation BR099C (left) and BR099D (right) without the use of clean windows. Produced from the same datasets as Fig. 4.7.*

Table 4.1.: *Positions of the Map peak in the phase-referenced maps at 22 GHz. The three used methods for finding the map peak position are shown. The values in columns with* cw *were determined including clean windows, with* ncw *without clean windows and* gc *represents Gaussian components. X and Y are Ra and Dec in mas. The last two columns give the mean values of x and y.*

Obs.code	date [yr]	$x_{\rm cw}$ [mas]	$x(ncw)$ [mas]	$x_{\rm gc}$ [mas]	$y_{\rm cw}$ [mas]	$y_{\rm ncw}$ [mas]	$y_{\rm gc}$ [mas]	$\bar{x}$ [mas]	$\bar{y}$ [mas]
BR099C	2005.4	0.68	0.75	0.72	0.38	0.38	0.42	0.72	0.39
BR099D	2005.54	0.23	0.30	0.28	−0.15	−0.23	−0.10	0.27	−0.16
BR099E	2005.65	1.73	0.75	1.36	1.35	0.00	0.43	1.28	0.59
BR099F	2005.76	1.28	1.73	1.24	0.38	0.83	0.4	1.42	0.54
BR099G	2005.87	0.38	0.38	0.37	0.45	0.53	0.55	0.38	0.51
BR130B	2008.45	0.75	0.68	0.73	−0.38	−0.38	−0.39	0.72	−0.38
BR130C	2008.56	1.95	1.95	1.92	0.60	0.60	0.60	1.94	0.60
BR130D	2008.67	0.23	0.15	0.25	−1.35	−1.35	−1.35	0.21	−1.35

For the methods using a clean window (located at the peak position) or a Gaussian circular component the resulting values are very similar except for BR099E. This does make sense since these methods should lead to comparable results, both are fitting the main peak. But setting clean windows does not prevent the residual map to show secondary peaks. By allowing the fitting of delta peaks in the whole map, depending on the errors in the image, there will be emission fitted where there may be no real emission. Due to that it is difficult to define which position should be used.

The mean values resulting from the three methods in Tab. 4.1 are not compatible within them. Applying these shifts to the maps of NGC 1052 does not provide a satisfactory alignment. They are even shifted in North-South direction away from the axis given by the jet directions. The results when

shifting with the negative of the mean values are seen in Fig. A.5. For BR099F the x_{ncw} value was excluded and a shift of -1.25 in RA was applied. The peak position obtained without the use of clean windows resulted in this case in a different shift as obtained by the other two methods. Between the two peaks there is no emission feature in the phase-ref map, therefore a mean value including x_{ncw} would not lead to a reasonable shift.

There could be some explanations for these results. Noise prevents a clear identification of the location of the image peak. So it is possible not to use the main peak, but for example the second highest peak at a more reasonable distance from the center. For BR099D that would be at $x = RA = 1.28$ mas and $y = Dec = 0.75$ mas. Still these shifts are about 0.5 mas away from that for BR099C. But they are very similar to BR099E. For BR099F it is difficult to apply the same procedure. There are peaks at $(x, y) = (1.20, 0.30)$ mas, $(1.12, -1.35)$ mas, $(-2.70, -3.00)$ mas and $(0.23, -0.45)$ mas where the flux of the clean boxes only differ from 0.050 to 0.073 Jy. The same method could be used for the other observations. But it is not possible to get shifts that lead to a consistent map of NGC 1052 over the observations.

The second possibility is that there are still too large errors in the phases so that it is impossible to differentiate the signal from the noise. Especially for the attempt of phase referencing each remaining residual error can distort the result. An additional source of errors may be in the modeling of the atmosphere. The data were corrected for introduced delays resulting from turbulences in the ionosphere. It was corrected for the opacity and the change from correlation coefficients to an amplitude in units of Jansky was made. This is a simplistic correction for the whole time of the observations, but does not include variations during the observing sessions in temperature, humidity, etc. The variations in the troposphere can especially be a problem at shorter wavelengths. There arise additional delays due to a different wet component over time (compare e.g. Thompson et al. (2001)). The introduced errors are dependent of the zenith angle. VLBI uses telescopes that are far enough away from each other so that the elevation of the source will be different for each telescope. The only method to correct these delays is by modeling the atmosphere, ionosphere and troposphere, as it changes with zenith angle. This correction was not applied to this experiment. It is possible that the errors introduced in this way distort the signal so that it is not possible to get useful results out of this phase-referencing experiment.

4.3. Twin-jet morphology at 43 GHz

For all following sections the 43 GHz data from the multi-frequency observation campaign between 2005 and 2009 were analyzed to find out whether the central feature, that is seen in the 86 GHz map, is indeed the center of emission for both jets. As shown by Kadler et al. (2002) at 43 GHz the torus in NGC 1052 is opaque to radiation, which leads to the conclusion that it is likely to have a look at the same emission regions as for the observation at 86 GHz, but with a lower resolution.

I discuss here the evolution of the source over the 4 years by comparing stacked images and overall flux density. The second step will be to discuss the evolution of the flux for the whole source, the core, the eastern and western jet, with special emphasis on the flux ratios of both jets. The eastern jet of NGC 1052 is interpreted to be the jet (pointing towards us) and the western jet as the counter jet. These terms follow Kadler et al. (2002), who analyzed observations in which the flux density of the eastern jet was higher than that of the western jet. These data suffered from the observed absorption at higher frequencies in the western jet. I decided not to define a jet and counter jet but to use the terms western and eastern jet.

I performed the calibration and imaging steps as described above (AIPS, section 3.4.1 and imaging in DIFMAP, section 3.4.2). Meaning an iterative process of CLEAN and amplitude and phase self-calibration was followed until the final clean maps were produced.

The whole data set including both frequencies were already used by Böck (2012), together with 15 GHz data from the MOJAVE team (Lister et al. (2009)). Böck (2012) followed the same standard routines in AIPS, but the clean maps were produced using an automatic imaging script. During the analysis a big percentage of the observations seemed to lack a clean model describing the visibility data with the utmost precision. Some tests of *re-imaging*, namely, manual re-imaging in DIFMAP, revealed

Table 4.2.: *Image parameters for all analyzed observations at 43 GHz with natural weighting. The RMS is taken from* DIFMAP

obs. code	clean map parameters					
	RMS [mJy beam^{-1}]	$S_{\rm peak}$ [Jy beam^{-1}]	$S_{\rm tot}$ [Jy]	$b_{\rm maj}$ [mas]	$b_{\rm min}$ [mas]	PA [°]
BR099A	0.68	0.33	0.80	0.46	0.20	6.25
BR099C	0.74	0.41	1.17	0.69	0.20	-16.85
BR099D	0.60	0.52	1.00	0.52	0.18	-11.36
BR099E	0.91	0.47	1.51	0.51	0.18	-12.80
BR099F	0.99	0.48	1.30	0.49	0.19	-8.47
BR099G	0.50	0.26	0.80	0.50	0.18	-9.89
BR099I	0.82	0.32	0.78	0.51	0.20	-8.11
BR119A	0.86	0.40	0.83	0.52	0.20	-8.12
BR119B	0.81	0.41	1.04	0.48	0.18	-7.16
BR120A	0.71	0.21	0.74	0.61	0.26	10.05
BR120B	0.56	0.24	0.69	0.41	0.17	-3.73
BR120C	0.46	0.25	0.49	0.40	0.16	-5.15
BR120D	0.53	0.30	0.64	0.51	0.17	-8.27
BR120E	0.47	0.26	0.56	0.53	0.18	-12.30
BR120F	0.86	0.29	0.63	0.88	0.49	21.76
BR120H	0.52	0.21	0.73	0.54	0.19	-11.98
BR120I	0.51	0.27	0.58	0.48	0.20	-4.82
BR130A	0.56	0.30	0.70	0.42	0.16	-6.07
BR130B	0.54	0.27	0.63	0.50	0.21	-2.34
BR130C	0.79	0.36	0.64	0.47	0.20	-4.37
BR130D	0.63	0.31	0.69	0.59	0.25	-5.82
BR130E	0.51	0.11	0.78	0.44	0.18	-4.77
BR130F	0.59	0.22	0.72	0.76	0.32	15.87
BR130G	0.67	0.26	0.69	0.99	0.37	22.77
BR130H	0.53	0.15	0.64	0.44	0.18	-3.25
BR130I	0.45	0.16	0.65	0.43	0.16	-7.43

additional emission regions in the maps not recovered by the automatic mapping script. This was performed for all data sets (in other words, automatic imaging served as an amplitude pre-calibration step):

The evolution of the total flux density recovered is presented in Fig. 4.9. It shows that the source is variable. The maximum change of overall flux density of 0.8 Jy occurred within 3 month, that is the flux density has halved. In the beginning the flux density rises from 0.9 Jy up to 1.6 Jy within 5 month, to follow a continuous decline to 0.65 Jy until the end of the four years of observation with a small rise again in April 2006 to 1.1 Jy. In May 2007 and one year later two sharp drops happened with following small rises.

4.3.1. The morphology

A stacked image (see Fig. 4.12) was produced (R. Schulz priv. comm.) and the flux density along the so called *ridge line* was plotted. A stacked image stands for a mean map for a set of clean maps. The ridge line is a line drawn along the maximum brightness along the jet axis and gives an impression on the main jet geometrical direction. For Fig. 4.12 the ridge line was was set to 65 degrees to the horizontal line. The clean maps can be used to study the extension of the source and emission regions.

The process of model-fitting was followed for the 43 GHz data, as is further described in Sect. 4.4, resulting in a model for each observation with a maximum number of fourteen Gaussian model compo-

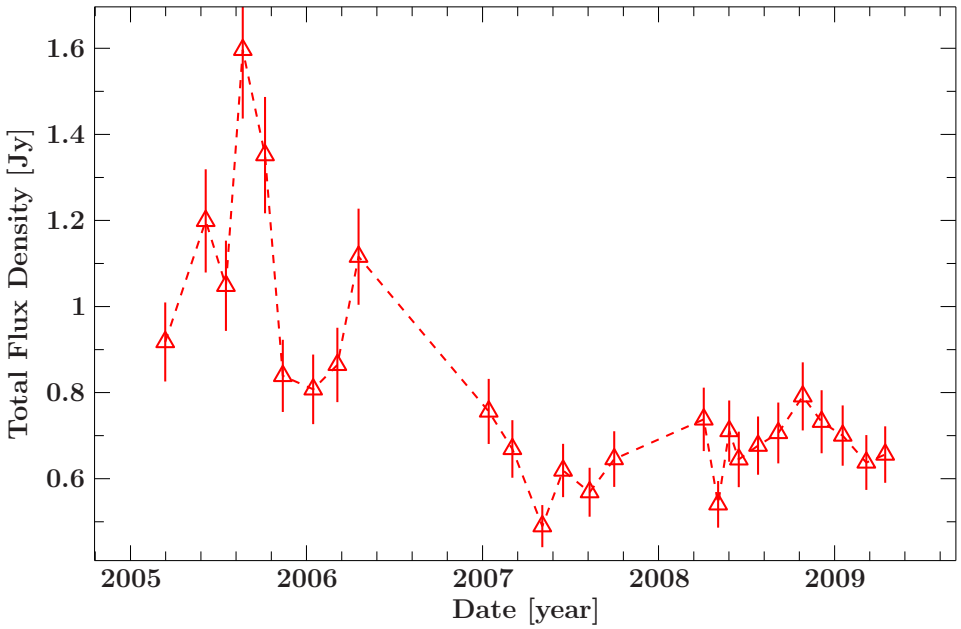

Figure 4.9.: *43 GHz total VLBI flux lightcurve.*

nents. Figures 4.10 and 4.11 show the clean maps for all observations with the corresponding models of Gaussian components plotted above. Components were cross-identified and their ejection times and locations were determined as described in Sect. 4.4.

The CLEAN maps (compare figures 4.10 and 4.11) show that the source morphology changes a lot over the four years of observation. In all epochs the central feature is the brightest. The observations were divided into three blocks: from 2005 to late 2006, for 2007 and from 2008 to April 2009. During the first block the two jets appear to be symmetrical, whereas in the second and third block the extension of the western jet is larger than that of the eastern and the source is overall more compact. In the second block the source is more compact and the number of Gaussian components is smaller.

This asymmetry becomes obvious, too, in the stacked image for all epochs, as shown in Fig. 4.12. The upper panel shows the stacked map for all 4 years of observation for the 43 GHz data. The flux density is color coded. The ridge line is shown over imposed and its flux density profile is shown at the lower panel. A bright central feature is present for all epochs in the center of the image. Both jets show a somewhat steady decline in flux density until about 3.4 mas distance from the center. Notice that the western jet, thought to be the approaching one, seems to be brighter. To the west the central feature first falls to a small local minimum. Starting at about -1 mas there is a plateau until -2 mas at which the the flux density of the western jet is nearly constant. From there, it falls linearly until the jet is not seen anymore. To the east from the central feature, the flux density falls and shows a small plateau from $\sim 0.15 - 0.8$ mas. From that it falls until the maximum extend of the eastern jet with a small rise at about 2 mas.

The differences between the first observation block (2005 to 2006) and the rest of the observation become obvious by comparing single stacked images for all three blocks (see Fig. 4.13). The first remarkable fact is the different extent of the source for the three time ranges. In the first time block both jets extend up to a relative RA of nearly 3 mas, for the third map the extent of the jets is about 1 mas less. In the second time block the structure is very compact. The eastern jet has a peak flux of about 0.035 Jy/beam near to the core at a distance of 0.6 mas and then decreases until only diffuse emission is visible beyond 2 mas RA . The western jet reveal stronger emission that decreases very fast beyond 2 mas.

For the first time block the map and the flux density plots are similar to the previous plot 4.12, but

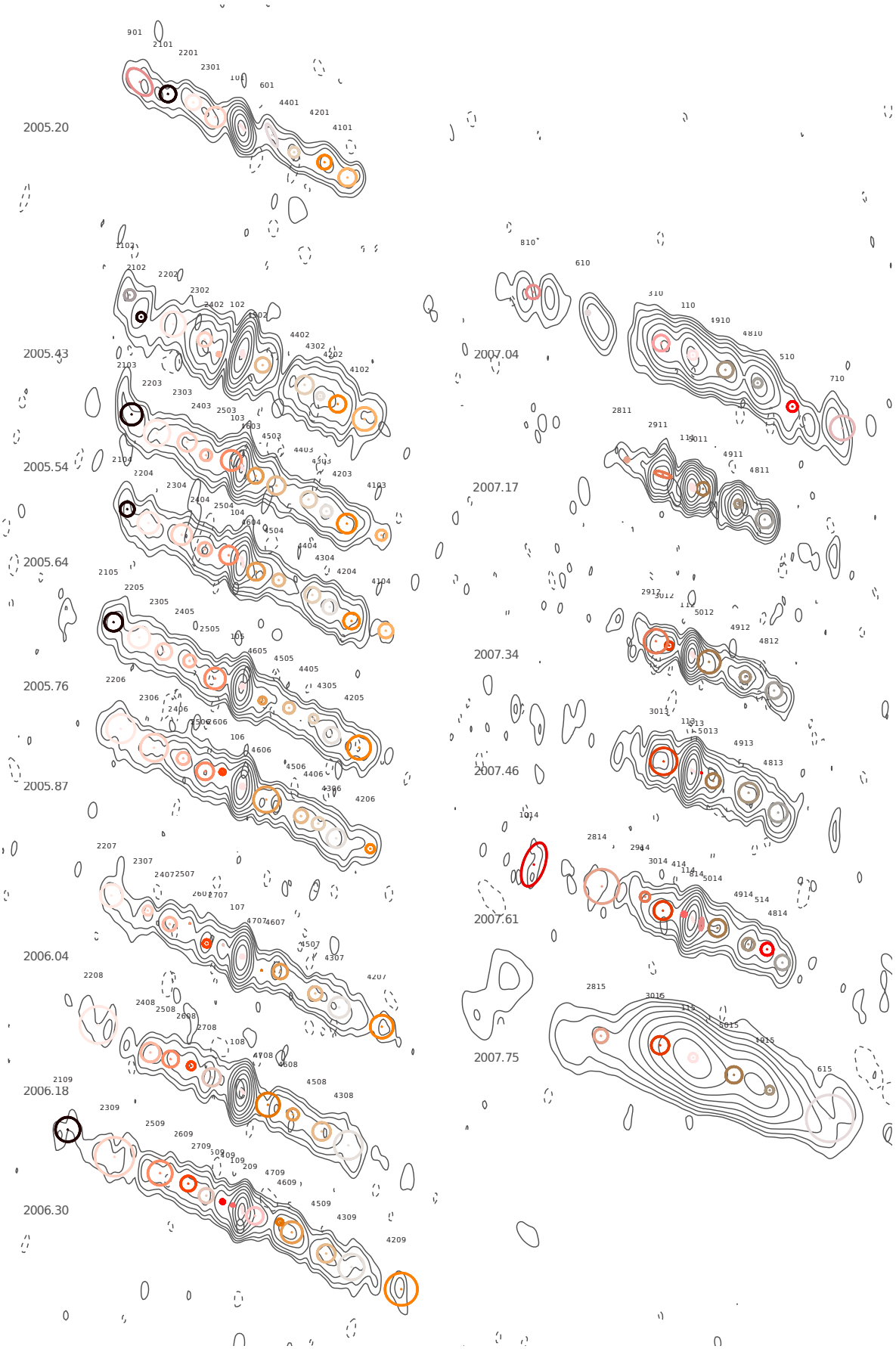

Figure 4.10.: CLEAN *contour maps with over-plotted model for the first block (left) and the second block (right). Tracked components have the same color. The date of observation is printed left of each image.*

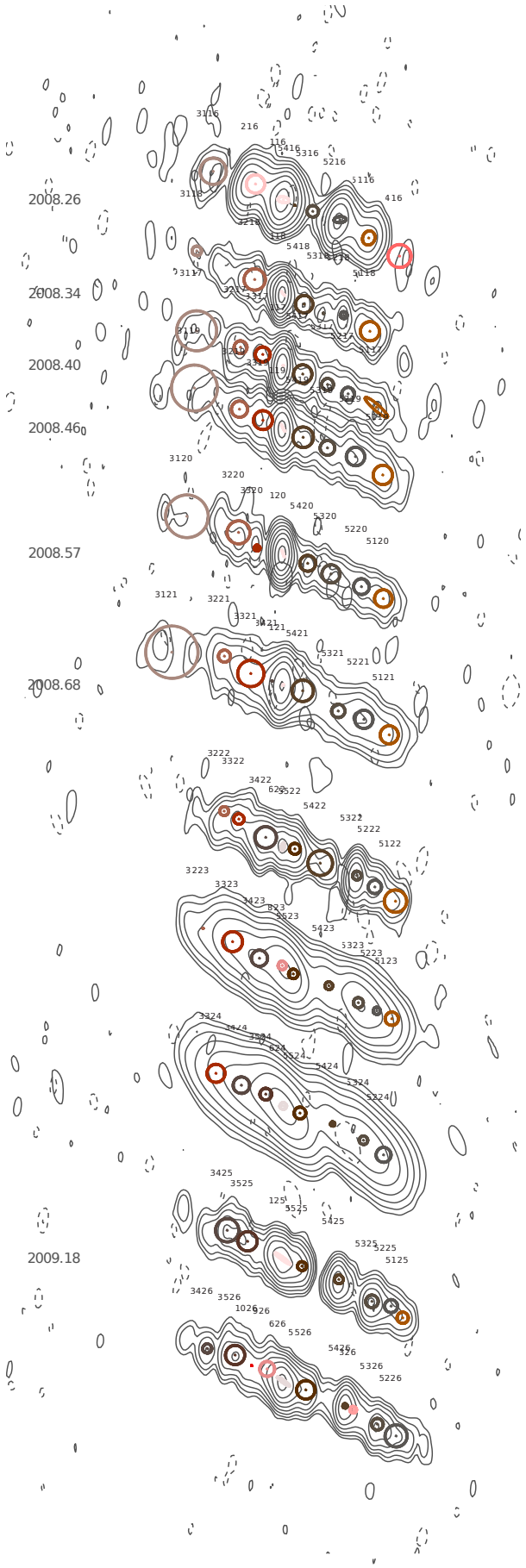

Figure 4.11.: CLEAN *contour maps with over-plotted Model for the third block. The date of observation is printed left of each image.*

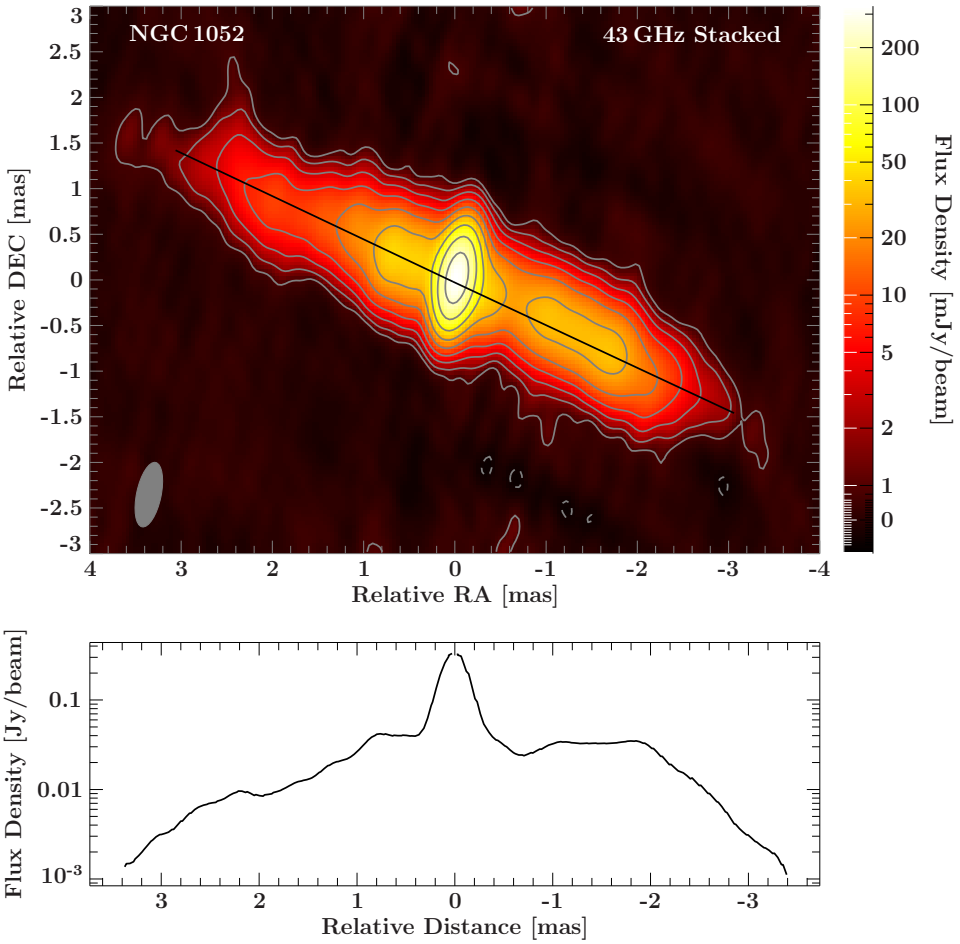

Figure 4.12.: *Stacked image for all observed epochs (upper panel). The lower panel shows a flux density along the ridge line, that is indicated in the upper panel as a line along the jet axis. In the lower left corner the resulting beam is indicated as a grey ellipse. (R. Schulz priv. comm.)*

there are some small distinctions to be made. The flux density of western and eastern jet seems to be similar, whereas the flux density in the western jet stays for a longer extent at about the same value and falls after reaching a small maximum at 2 mas with about the same gradient as in Fig. 4.12. For the second and third time-range the differences between the two jets are significant. The western jet has high flux density between 1 mas and 2 mas and falls then rapidly, whereas the eastern jet has only a small region of higher flux densities, that is closer to the central feature. The flux density falls earlier until 2 mas but not as steep, shows then a small dip before only diffuse emission is seen.

The ridge line plots show differences between block 2 and 3, too. In block 2 there is a small dip close to the core in the eastern jet, that is not seen in block 3. In addition, the flux density between -1 and -2 mas in the western jet is more continuous in block 3. In block 2 there is only a small dip at about -1 mas. These differences between the two jets over the four years of observation get obvious by comparing the single clean maps in figures 4.10 and 4.11, too.

The epochs 2007.17, 2008.82, 2009.18 and 2009.29 show very compact emission regions in both jets, that are distinguishable to each other. For all four there is at least one bright feature in the western jet between 1 and $\sim$ 1.5 mas distance from the core. The regions have all a more or less strong emission gap on the east side. For the epochs 2008.82, 2008.93 and 2009.05 a large fraction of the flux that was before in the core is now divided to both jets. In these epochs there appear components in a small

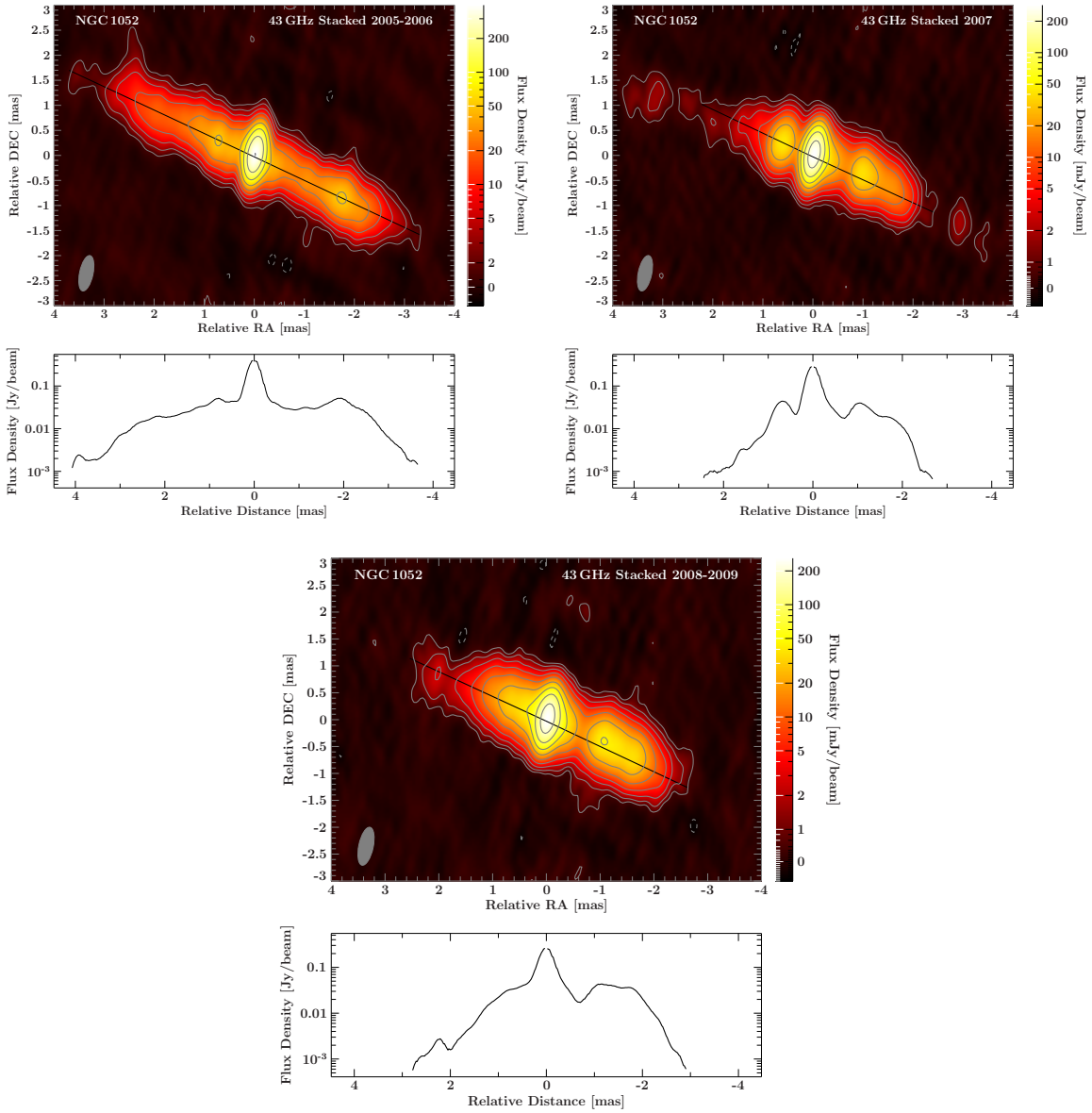

Figure 4.13.: *Stacked image for three different time-ranges, top left: from 2005 to 2006, right:2007 and bottom: 2008 to April 2009. Observed epochs in the upper panel. The lower panel shows a flux density along the Ridge Line, that is indicated in the upper panel as a line along the jet axis. (private communication R. Schulz)*

distance below ~ 0.5 mas to the core with a high flux.

This fact and the previous discussion is a strong indication for a asymmetry in the two-sided jet system. Not only here, but from the previous discussion it becomes more likely that the central emission feature is the center for both jets and as this containing the central engine and the bases of both jets.

For Fig. 4.15 the Gaussian model components were summed up for different regions of the twin-jet system over the 4 years of observation. The red curve shows the flux evolution of the whole source, the green curve that of the core, the blue one that of the western jet and the magenta one that of the eastern jet. The lightcurve shows, that for the epochs 2008.82, 2008.93 and 2009.05 the flux of the core is below that of each jet. The only possibility the core would gain more flux is to add the components of both jets that are at the shortest separation from the center to the core, but that would result in an

emission region for the core, that has an extent of ~ 0.8 mas. However, the other epochs show that the core seems to be less extended. Having a look again at the stacked images the strong emission feature in the center, that should correspond to the core, has an extent of ~ 0.7 mas. Consequently one could define that all emission that is in a distance of up to 0.35 mas from the center is to be added to the core. But one should consider that the stacked maps were produced by convolution with the same beam, that was the biggest one for all observations. Following from that it is very likely that the emission region for the central feature can be resolved to be smaller than these 0.8 mas in most epochs with higher resolution.

4.3.2. Flux density ratio of western to eastern jet

Fig. 4.14 shows the flux of the eastern jet versus that of the western jet for each image (separated in time blocks). If the brightness and velocity of both jets are initially the same, the values should lead to a line through the origin with a gradient depending on the inclination angle. If this line does not go through the origin, this is an indication for an asymmetry as there have to be some deviations from the initial assumptions.

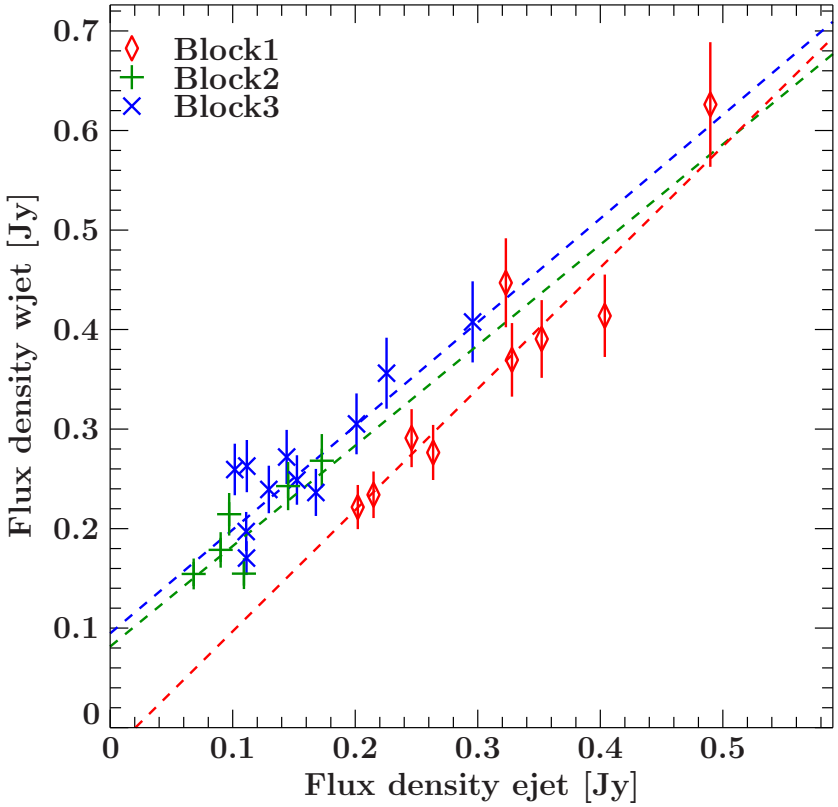

Figure 4.14.: *Flux density of western jet versus eastern jet, values see Tab. 4.3*

A linear regression fit to each block leads to similar gradients for the time blocks 2 and 3 but to a different one for block 1 (fit values see Tab. 4.3). The difference in morphology, as discussed in the previous section, is reflected in the fits. For all blocks the flux ratios are consistent with each other and show within a 1σ error no significant differences. The fit to block 1 results in a very small y-offset that is within 1σ consistent with zero and that of the other blocks only within 3σ. The fits show that there is a difference between time block 1 and the other two and this deviation is likely to result from an asymmetry as the best fit does not go through $(0, 0)$. The plot shows two points from block 1 to be consistent with the fits to blocks 2 and 3, so there might to be two epochs in time block 1 that fit better

Table 4.3.: *Fit values to flux density of western jet vs. eastern jet*

Block	Gradient	Y-offset to (0,0) [Jy]
All	0.83±0.06	0.11±0.01
Block1	1.22±0.15	-0.02±0.04
Block2	1.01±0.25	0.08±0.03
Block3	1.04±0.17	0.09±0.03

Table 4.4.: *Mean flux ratios of western to eastern jet for each block and the resulting upper limits for the angle of the jet to line of sight. Asuming $\alpha = -1$ and $\beta = 1$.*

Block	Time range	S_w/S_e
1	2005 to 2006.4	1.149
2	2007	1.850
3	2008 to 2009.3	1.770

to the overall trend of the observations between 2007 and 2009. A linear fit to all epochs result in an y-offset of 0.11 ± 0.01 from the origin and a smaller gradient as for each single block. The y-offset of this fit is within 3σ not consistent with 0. These result supports the asymmetry seen in the jets further.

Figure 4.15 shows the flux evolution for the different regions of the source (panel a), the percentage of the regions of the source on the whole flux density (panel b), and flux ratio between western and eastern jet(panel c). For these plots a flux error of 10% was assumed. The lightcurves for the two jets show a very similar evolution of the flux. In the beginning it rises from about 0.25 Jy to a value of about 0.5 Jy, falls again to its starting value, rises slightly and then falls, beside a rise during the last seven epochs. Starting at about 2006.4 the difference between western and eastern jet stays at nearly 0.1 Jy (see panel (d) in Fig. 4.15). Besides the second and fourth epoch the flux values are similar to before 2006.4. The evolution of the core is similar to that of the jets until 2008.40.

Since the absolute difference between western and eastern flux density stays nearly constant after 2006.4, but the flux changes over the following epochs, the ratio between western and eastern jet varies strongly, but all the time it is larger than one. The 43 GHz western jet is the brighter one between 2005 and 2009. By assuming that the brightness of both jets is initially the same a difference in flux density can only be explained by the orientation of the system with respect to the line of sight (compare Sect. 2.3.2). If the only explanation for a difference in flux is then the orientation of the source to the line of sight, this result would imply that the orientation of the jet-system changes during the four years.

The flux ratio of the western to eastern jet varies from nearly one up to about 2.5. Tab. 4.4 shows the mean values of flux ratio for each block.

Recalling equations 2.3.11 and 2.3.12, the inclination angle θ can be derived out of the flux density ratio, the spectral index α and the jet velocity assuming both jets to have the same intrinsic properties. The spectral index was estimated to be $\alpha_{\rm jet} \simeq -1$ (Kadler et al., 2004). By comparing the brightness temperature ratio of single components Kadler et al. (2004) estimated an inclination angle of $\sim 72°$. Böck (2012) recently performed a kinematic analysis of NGC 1052 at 15, 22, and 43 GHz and derived an averaged apparent jet velocity of $\beta_{\rm app} = 0.230 \pm 0.011$. He did not find significant differences between the velocities of the eastern and the western jet. So the apparent velocity can be assumed to be equal to the intrinsic one. He derived as well an inclination angle of $\theta \geq 78.8°$ based on the apparent velocities. Including a mean component brightness between jet and counter-jet of 2.00 to 2.15 he could give an upper limit of $\theta \leq 70°$, not compatible with the previous estimated value. These results suggest that some assumptions were wrong, e.g. some properties, like velocities and brightness, are not initially the same for both jets.

From the flux ratios derived in this work it was obvious that the inclination angle would have to change between the 4 years of observation to fulfill an initially equal flux ratio between both jets. An explanation for these flux ratios could lie in initial conditions that differ from the assumed ones: initially

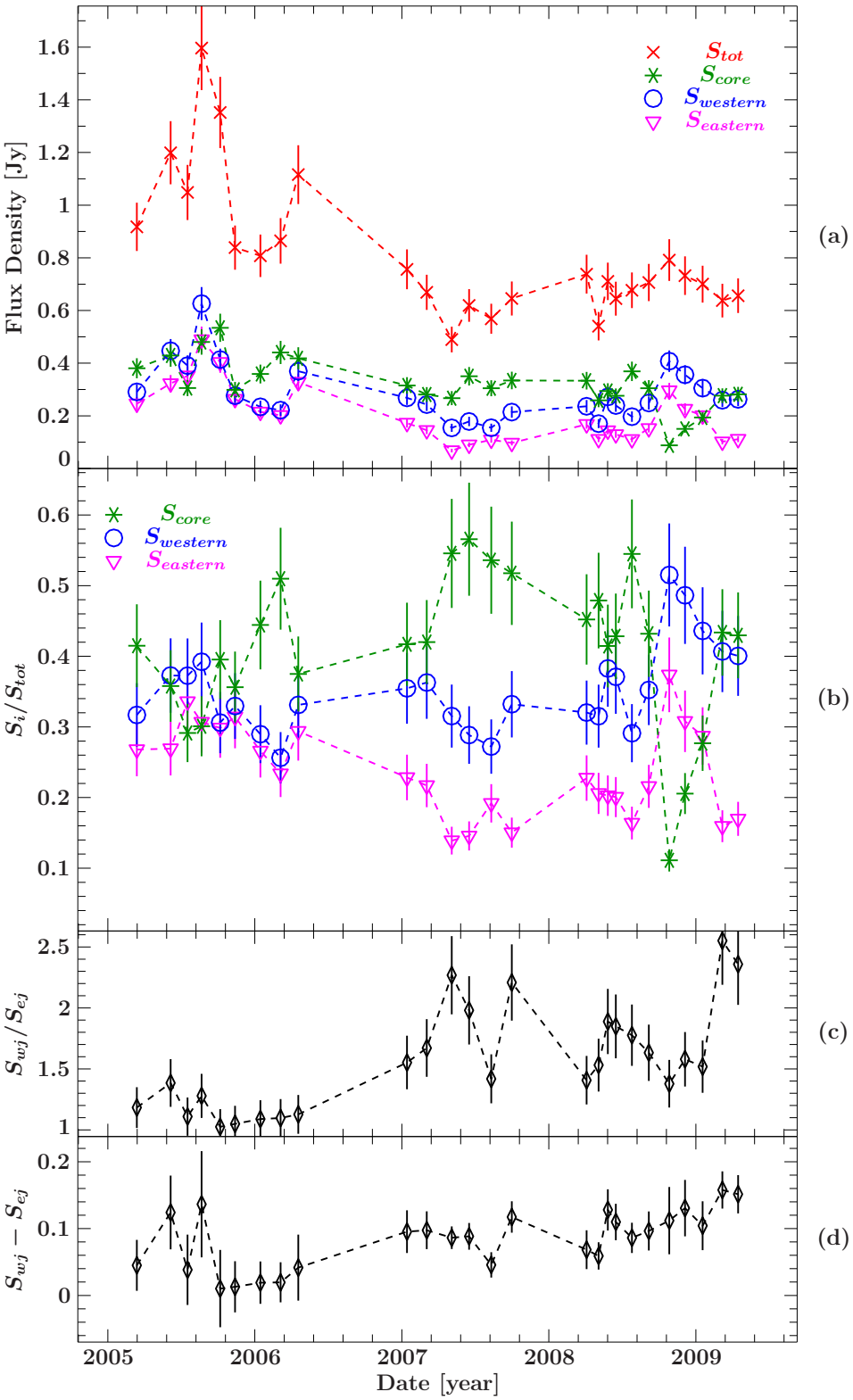

Figure 4.15.: *a) Lightcurve at 43 GHz of the total flux density recovered in the model of 2-dimensional Gaussian functions, the core flux density, the western and eastern jet; (b) the percentage of the regions of the source on the whole flux density; (c) the flux density ratio of western to eastern jet; (d) the absolute difference of flux density of western and eastern jet. The flux density values for all regions of the source are listed in Tab A.1.*

asymmetric flux ratios or different jet velocities.

Based on the different flux ratios estimated here the calculations following Böck (2012) can be repeated by using the velocities derived therein. As already mentioned it is possible that the velocities of eastern and western jet are different, contrary to Böck (2012). To verify this assumption, velocities out of the re-imaged data-set are derived in Sect. 4.4 prior to derive the jet inclination angle.

4.4. Kinematic study

The location of the ejection regions of both jets can be estimated by modeling the jet motion. The matter ejected by the nucleus can be associated to enhanced emission features moving downstream at relativistic speeds. Since both jets are visible and traceable in NGC 1052, the tracking of emission features will define the most probable date and location of the ejection event. Setting the central bright feature in the center of the source kinematic study can verify if this assumption is a good one.

The clean model that resulted from the imaging process consists of some hundreds of point sources that model the emission of the source in the best possible way. Tracing the motion of features from these CLEAN components is not easy therefore.

I replaced the CLEAN components by a model consisting of a few extended two-dimensional Gaussian shaped functions, that are fitted directly to the visibility data. The functions can be shaped as circles, so the full wide half maximum (FWHM) in both dimensions is the same, or as ellipses that lead to two different FWHMs values. In principle other fitting functions are possible, but the Gaussian functions offer a good description of the emission and Fourier transformations are computationally inexpensive. The use of self-calibration is not recommended at this point, since the structure information of the source obtained in the hybrid mapping process can be lost.

Before model-fitting starts one needs to have an initial model. There are two possibilities. One is using the DIFMAP command *startmod*. This applies one attempt of phase-calibration on a point source starting model at the map center. The command *startmod* removes the clean model, adds a default point-source starting model with a flux of 1 Jy at the map center, applies a phase self-cal and then removes the starting model. This process leads to a shift of the map so that the peak flux is in the center of the map. If a good starting model already exists, like it is the case for the clean-map, the step of *startmod* have to be skipped and the only thing to do is to remove the clean-model point sources (no further self-calibration).

After that, a model out of elliptical Gaussian components is build. This is achieved by adding components sequentially at the location of the local maxima in the residual map and applying the model fitting algorithm to the visibilities each time when a new model component is added. By following this attempt a simple model of Gaussian components is produced that describes accurate and conveniently the emission regions in the map.

The produced models for the observations at 43 GHz consisting of Gaussian components were used to derive pattern speeds in the western and eastern jet. Due to a much lower resolution in three datasets, BR099B, BR099H, and BR120G, these where excluded from the further analysis (these are not shown in the previous plots of the datasets, too).

The components were identified over the epochs by comparing the models for all observations. Figures 4.10 to 4.11 were used for this comparison. The clean maps gave the first hint on emission features moving outwards for cross-identification between adjacent observing epochs. For example in epochs 2005.43 to 2005.76 there is in the western jet a set of three components starting at about -1 mas in RA from the center. These three components stay in similar relative positions to each other and their properties (size, flux, or brightness temperature) are in a reasonable range to be assumed being the same over these four observations. As the components move down the jet, their flux density is assumed to decrease and the size to increase. The cross-identification is based on the assumption of constant speed (extrapolating the component location). A linear fit to assigned components give their apparent velocities. The trajectories can be compared and with that the initial assumption to set the brightest feature at the center of the source can be verified. The number of components, assigned to each emission

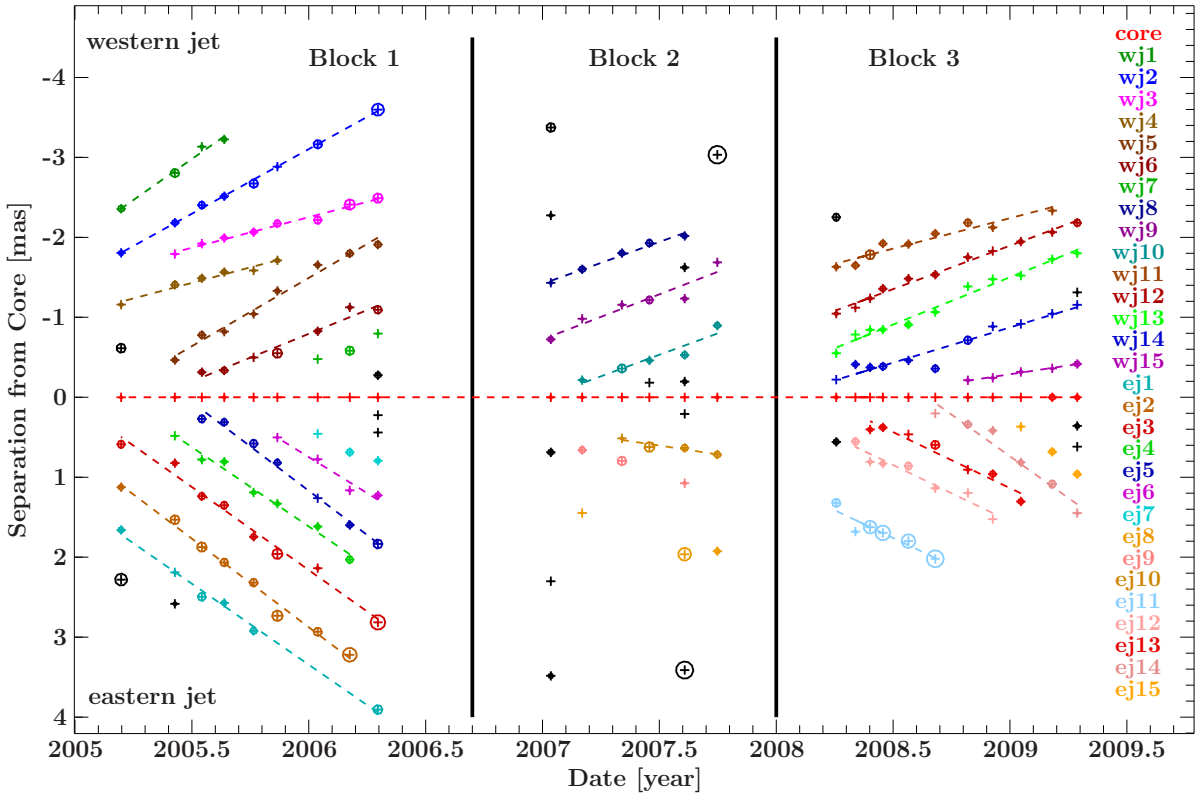

Figure 4.16.: *Separation of components from the core over time. Fit to each component is indicated by a dashed line. The eastern jet model is plotted in the lower lower half of the plot, the western jet in the upper half of the plot. Components that are not assigned are black.*

region were simplified to facilitate cross-identification.

Linear regression fits were applied to the assigned components observing date versus distance from the core (see Fig. 4.16). The observational date is on the x-axis and the separation from the central component on the y-axis. The brightest feature in each epoch was assumed to be the core of both jets. Since the core is assumed to stay at one position, so be a stationary feature, the models of Gaussian components are shifted so that the components identified as the *core* are in the center of the coordinate system. In the upper half the western jet is plotted and in the lower half the eastern jet. The size of the components corresponds to the relative sizes of the major axis of the corresponding Gaussian components. The 15 tracked components in the eastern jet are named starting with *ej* and in the western jet starting with *wj*. The individual tracked components are color coded. Fig A.2 shows the same data, but color coded is the observational date and the size of the components corresponds to the relative flux.

It can be seen, that there exists two time gaps over all four years. Since an identification of the components over the gaps is ambiguous, the observations were divided into three blocks, as is indicated by the lines in Fig. 4.16. Fig. 4.17 shows the same plot separated to the three blocks. The fitted velocities of all components are listed in Tab. A.8 and in Tab. 4.5 the resulting averaged and maximum velocities of western and eastern jet for each block and the mean value for all epochs can be seen.

The fits on the tracked components that consists only of a few epochs have larger uncertainties. As a result velocities were only derived for components that could be tracked over at least four epochs. This is a even stronger boundary as used by the MOJAVE-team (Lister et al. (2009)), who require at least components that are tracked over three epochs.The impact of that can be seen in the plots as only the

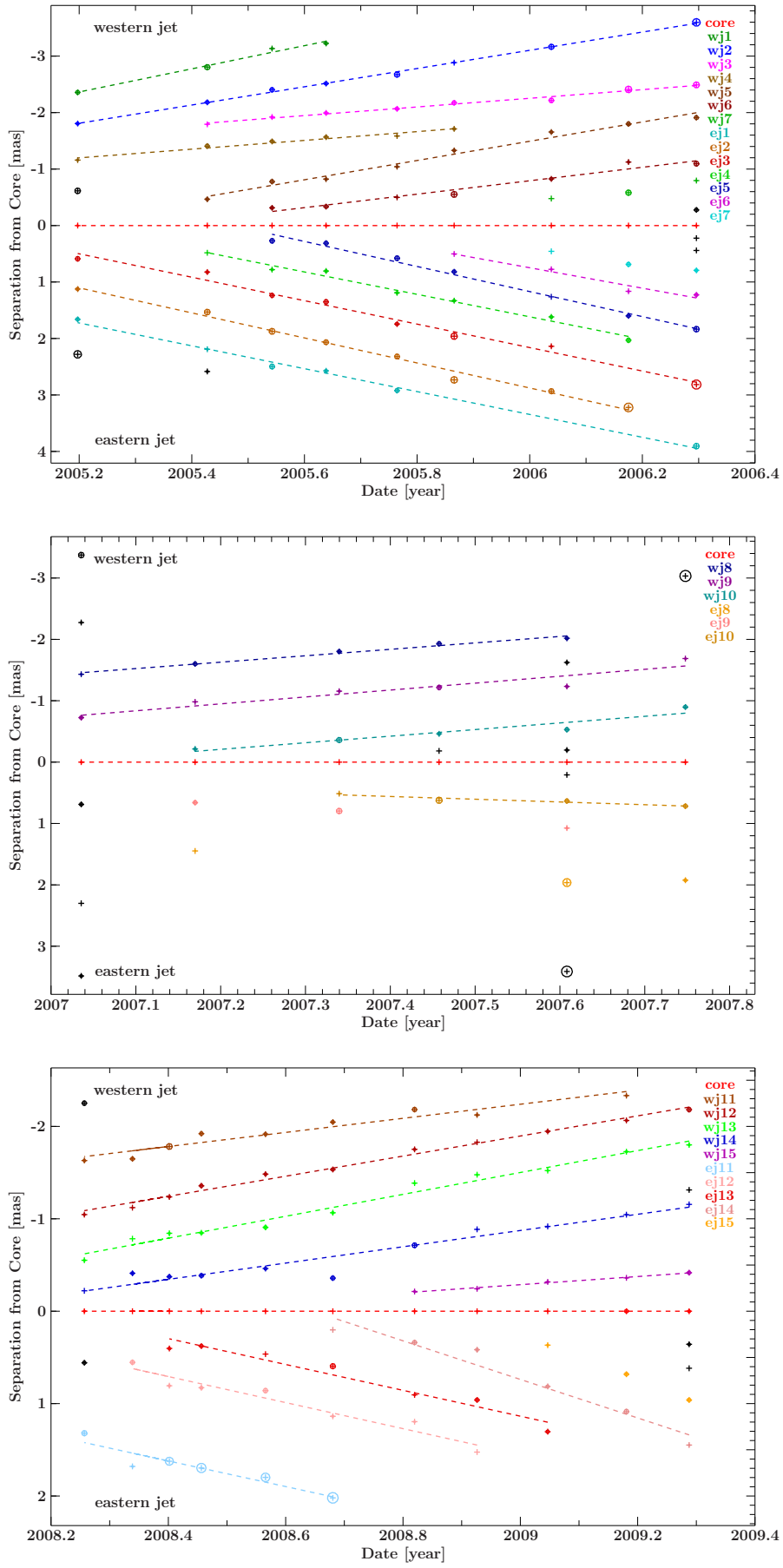

Figure 4.17.: *Separation of components from the core over time. Fit to each component is indicated by a dashed line. The tracked components are color coded. The eastern jet model is plotted in the lower lower half of the plot, the western jet in the upper half of the plot. Components that are not assigned are black.*

Table 4.5.: *Averaged velocities for the eastern and western jet for each of the three blocks as averaged values for the whole observations*

	western Jet [c]		eastern Jet [c]	
	v_{mean} [mas yr^{-1}]	β_{mean} [c]	v_{mean} [mas yr^{-1}]	β_{mean} [c]
Block 1	1.35 ± 0.73	0.40 ± 0.22	2.05 ± 0.71	0.61 ± 0.21
Block 2	1.08 ± 1.18	0.32 ± 0.35	–	–
Block 3	0.87 ± 0.66	0.26 ± 0.20	1.57 ± 1.08	0.47 ± 0.32
Mean	1.12 ± 0.46	0.34 ± 0.14	1.86 ± 0.61	0.56 ± 0.18
	v_{max} [mas yr^{-1}]	β_{max} [c]	v_{max} [mas yr^{-1}]	β_{max} [c]
Block 1	2.05 ± 3.04	0.61 ± 0.91	2.22 ± 1.46	0.66 ± 0.44
Block 2	1.13 ± 1.67	0.34 ± 0.50	0.00 ± 0.00	0.00 ± 0.00
Block 3	1.19 ± 0.89	0.35 ± 0.27	2.09 ± 1.97	0.62 ± 0.59
Mean	2.05 ± 3.04	0.61 ± 0.91	2.22 ± 1.46	0.66 ± 0.44

component trajectories that are fitted have the resulting fit plotted as dashed line.

There are only a few components in the second block that could be tracked, since, as already mentioned, the extent of the jet-system is smaller than in the other two blocks and there are only a few regions of emission. For the eastern jet this and the restriction to components that were tracked over at least four epochs, led to only one fitted velocity, that of component *ej10*. This component and *wj15* are very close to the core and have very large errors. As I don't trust these two components, they were extracted from the calculation of the mean value.

To be able to compare both jets, averaged velocities for both jets were derived for all epochs and for each of the single blocks. The averaged velocity of the western jet is $1.12 \pm 0.46\,\mathrm{mas\,yr^{-1}}$ and that of the eastern jet $1.86 \pm 0.61\,\mathrm{mas\,yr^{-1}}$. This corresponds to projected velocities of $0.34 \pm 0.14\,c$ for the western and $0.56 \pm 0.18\,c$ for the eastern jet.

The velocities are plotted in Fig. 4.19 over the mean distance of the tracked component from the core. The dashed lines show the mean velocities for each block and jet. Fig. 4.18 shows the mean velocities for each time block over the mean observation date, errors corresponding to the Gaussian error. Within a 1σ error the single as well as the mean velocities are the same for all blocks as well as for both jets. However there is a trend towards higher velocities for the eastern jet.

In addition to Böck (2012), Vermeulen et al. (2003) found no significant differences between western and eastern jet velocities (from kinematic studies at 15 GHz). Böck (2012) measured an averaged velocity of $0.74 \pm 0.06\,\mathrm{mas\,yr^{-1}}$, that corresponds to $0.230 \pm 0.011c$. Vermeulen et al. (2003) obtained a similar value of $0.78 \pm 0.12\mathrm{mas\,yr^{-1}}$.

Within 1σ the velocity of the western jet is consistent with that of Vermeulen et al. (2003) and Böck (2012), that of the eastern with 2σ. It is possible that the region observed at 43 GHz can shows other kinematics as at lower frequencies.

By extending the trajectories in direction to the core, the area of ejection has to lie within a range of about 0.4 mas around the center, so 0.2 mas distant from the center. From all these considerations the component tracked as core seems to be indeed the center of the twin-jet. If the initial assumption that the region seen at 43 GHz is the same as at 86 GHz it is very likely that the bright central feature as seen at 86 GHz is the center for both jets, too.

In the previous section it was suggested that there is an asymmetry between both jets. This was clearly seen in the stacked maps. In this section it was shown that there is only a trend to higher velocities for the eastern jet, that could not be defined better in the scope of the errors.

There is an additional asymmetry in the ejection of plasma into both jets. By following the trajectories to the center of ejection not for all ejection times of western components there is an ejection towards the eastern side, too. The first components could not be tracked over enough epochs and are starting already to far away from the core to give a clear statement. So components *wj1* to *wj4*, as well as *ej1* to *ej3* can not be associated with each other. The components *wj5* and *ej4* could be ejected at the

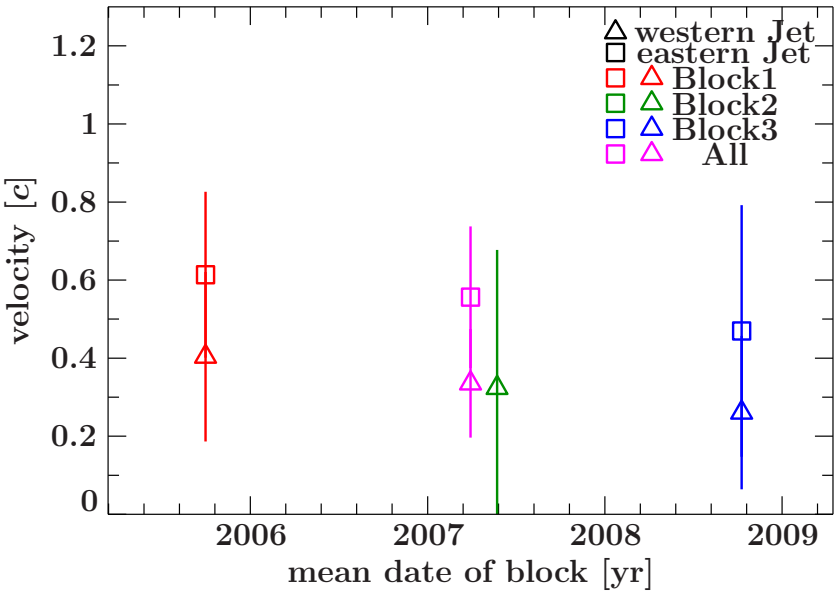

Figure 4.18.: *Mean apparent velocity versus mean epoch for each block and the whole observation.*

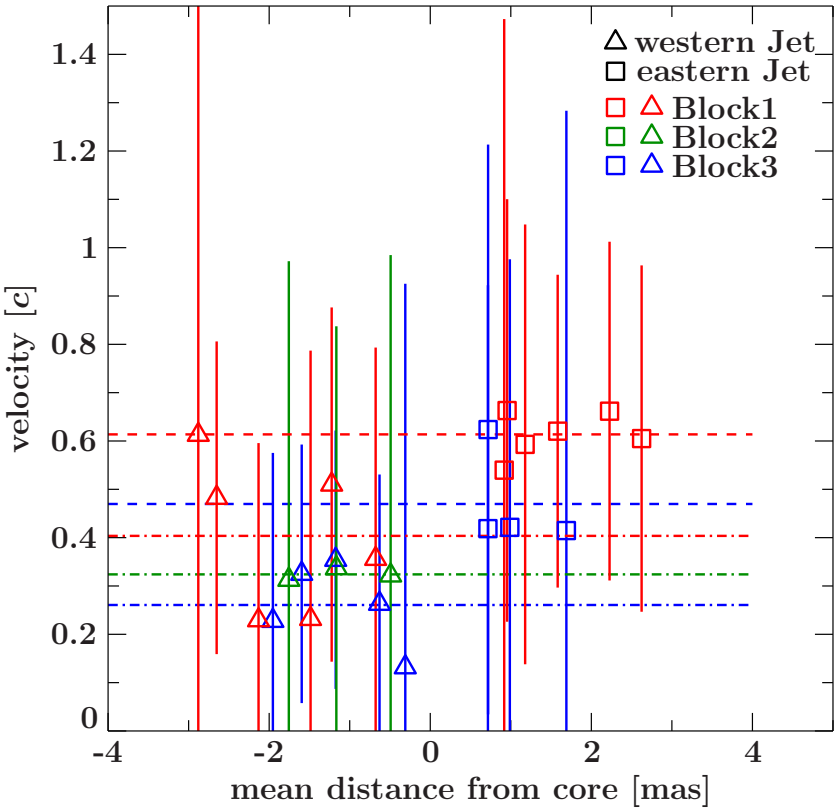

Figure 4.19.: *apparent velocity versus distance from core(top) and maximum velocity (bottom).*

same time as well as *wj6* and ej5, but following there are two components in the eastern and only one in the western jet. Having a look at the second block it gets even difficult since there is only very little

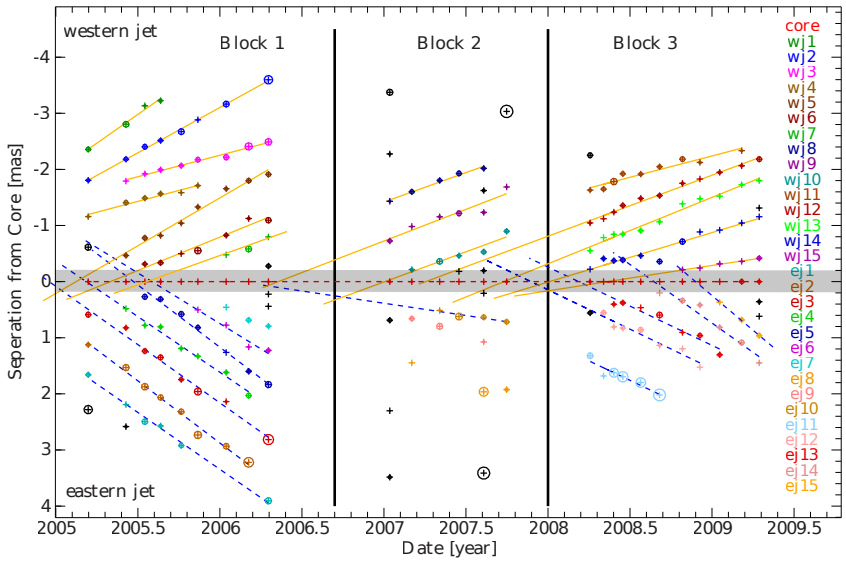

Figure 4.20.: *By extending the fitted trajectories to the center an area can be defined that is most probable to be the region of ejection (grey shaded)*

Table 4.6.: *Mean flux ratios and velocities of western to eastern jet for each time block.*

	β_{app} $[c]$	$S_{\mathrm{w}}/S_{\mathrm{e}}$
Block 1	0.509 ± 0.075	1.149
Block 2	0.229 ± 0.005	1.850
Block 3	0.365 ± 0.060	1.770

movement in the eastern jet. There is only one component that could be followed over more than three epochs (*ej10*), but as already explained its velocity is very low compared to all others. It is difficult to declare the time of ejection of that component. All others are not constrained well enough. In block three there are again more components for both jets, but there are no clear assignments. It is possible that *wj15* and *ej14* were ejected at the same time, but with very different velocities, and then there is no counterpart for *ej15*. Furthermore it is not clear whether *ej12* or *ej13* could be a counterpart to *wj14*.

All in all there are a lot components that were not ejected symmetrically into both jets.

4.5. Change of the inclination angle or asymmetry in jets?

In the previous sections mean values of velocity and flux ratio of western and eastern jet were derived for each block and jet, as can be seen in Tab. 4.6. These values can now be used to derive the angle to the line of sight out of equations 2.3.11 and 2.3.12. Here it was assumed that the velocity and the flux ratio is intrinsically the same for both jets.

The grey shaded region in each plot in Fig. 4.21 shows the possible combination of intrinsic velocity and observing angle for the given parameters. Each block and jet was looked at individually. For each time block the mean apparent velocity (solid red line) for both jets was used and the mean flux ratio per block (the flux ratio is the same for both jets). To define a possible range for the velocity the Gaussian error for the mean values was derived to give upper and lower limits, represented by the dashed red lines. For the flux ratios ten percentage of flux error was used to derive the limits as indicated by the dashed blue lines, the values resulting from the mean flux are shown by the solid blue line.

The intersection of both jets per block gives the possible values for β and θ under the assumption,

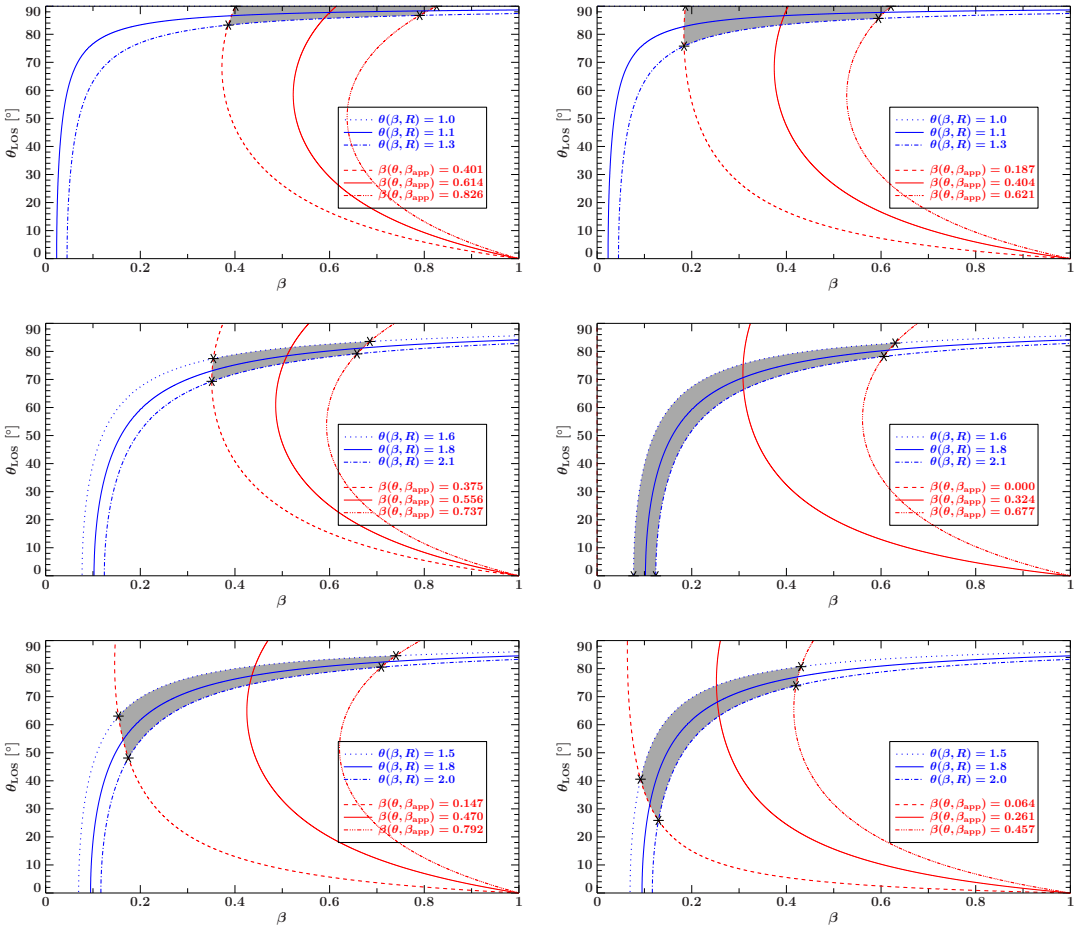

Figure 4.21.: *Angle of the jet to the line of sight θ_{LOS} depending on the intrinsic jet velocity β derived from the flux-ratio of western to eastern jet at 43 GHz (blue) and the averaged velocities constrained out of the kinematic analysis at 43 GHz (red). The given 1σ errors give the dashed lines. For the velocity a Gaussian error was derived and 10 percentage of flux error lead to the Gaussian flux ratio error. The allowed parameter space for θ_{LOS} and β is highlighted by the grey-shaded region. From top to bottom: Block 1,2 und 3. Left: eastern jet; right: western jet.*

that both jets are initially the same, in brightness and velocity. These intersections are shown in Fig. 4.22.

From the intersections in Fig. 4.22 there is an overlap for time block 2 and 3 as can be seen in Fig. 4.23, but none with block 1. For all three time blocks there is a small range in that β can be the same for all block: $\beta = [0.401, 0.429, 0.457]$. But the angle to the line of sight for the intersection of block 2 and 3 is within $\theta_{\mathrm{LOS}} = [1.589, 1.804, 2.020]$ and for block 1 within $\theta_{\mathrm{LOS}} = [1.000, 1.149, 1.312]$. To describe the observed flux densities with intrinsically the same flux density of both jets and the same velocity, the angle to the line of sight have to change. All observations can be explained with the same inclination angle of the jets and intrinsic velocity if 2σ errors for the mean velocities and flux ratios are assumed. Meaning using twice the Gaussian error for the velocity range and 20 percent of flux error. This results in larger grey shaded areas in Fig. 4.21 and in an intersection for both jets and all observations, as can be seen in Fig. 4.24. As the Gaussian error of the mean sets an already very high error, compared to the statistical standard error from the mean, a change of the angle to the line of sight between time block 1 and 2 cannot be excluded, if the initial assumed conditions are correct.

The case of the microquasar SS 433 showed that a precessing of a jet-system is possible. It is a

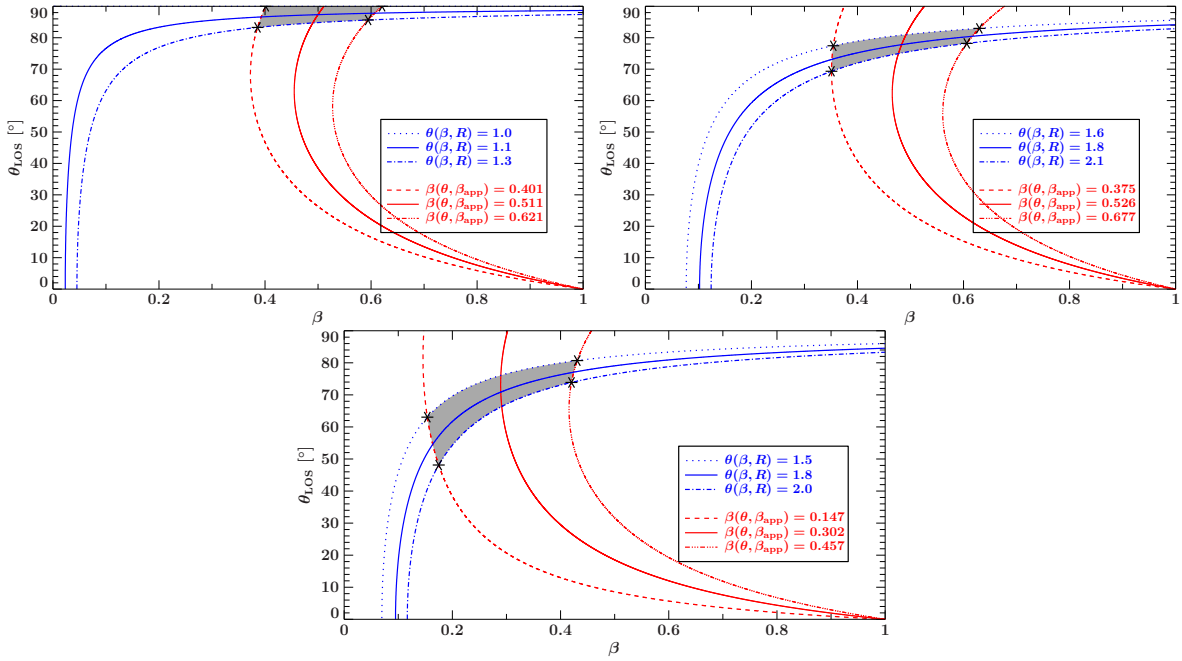

Figure 4.22.: *Angle to the line of sight. Shown are the intersections of possible areas for eastern and western jet for each block: upper left: block1, upper right: block2 , lower panel: block3. (For a more precise explanation of the plot see Caption of Fig. 4.21)*

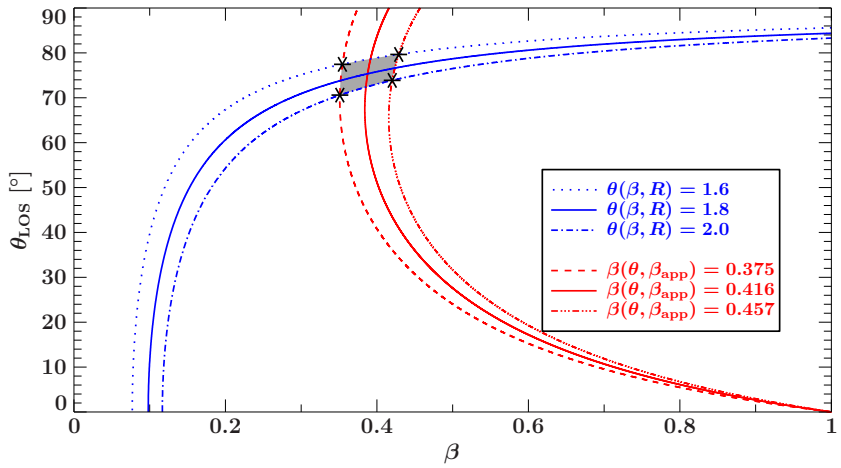

Figure 4.23.: *Angle of the jet to the line of sight θ_{LOS}. Shown is the intersection of block 2 and block 3. (For a more precise explanation of the plot see Caption of Fig. 4.21)*

well-studied X-ray binary in the optical, X-ray and radio regime. Margon & Anderson (1989) derived (out of optical line positions) a precession of the jet orientation in a cone with half-angle of 19.85° around the angle to the line of sight of 78.83°. In radio wavelength the jets with position angle of 100° show an oscillatory pattern that most probable results from a helical motion of the outflowing material (Hjellming & Johnston, 1981).

It is possible that these kind of helical motions can be observed in big counterparts to SS 433, too. The inclination angle of the jets in NGC 1052 close to the line of sight and its distance of only about 19 Mpc give the possibility to study these deviations from the standard model at high resolution and

to find similarities to smaller (galactic) jet systems like SS 433.

Having in mind the discussion in the previous sections, the morphology, flux evolution, and the kinematic analysis, it can not be ruled out that the assumption of intrinsically the same flux ratio and velocity for both jets is wrong. The stacked images showed clear asymmetries in the jets. The western-to-eastern-jet flux density ratio changed dramatically from nearly 1 to about 2.5. Furthermore, earlier studies of NGC 1052 found the eastern jet to be the brighter one (see e.g. Kadler et al. (2004) or Vermeulen et al. (2003)). All this makes it very probable that the assumptions needed to derive a parameter space for β and $\theta_{\rm LOS}$ as shown in figures 4.21 to 4.24 are not correct. For the case of an

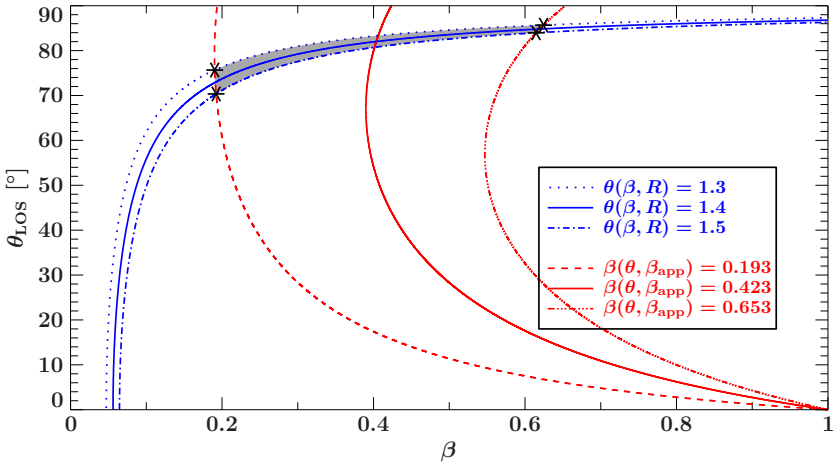

Figure 4.24.: *Angle of the jet to the line of sight $\theta_{\rm LOS}$ as a function of the jet speed. The grey shaded region show the intersection for both jets and all observations. For the mean velocities a 2σ error was assumed, as well as for the flux density, resulting in an Gaussian error for the wester-to-easter-jet flux density ratios.*

asymmetry in the jets, the next question is how it is produced. Possible explanations are an asymmetry in the magnetic field, that can result from an asymmetry in the accretion disc (As shown by Fendt & Sheikhnezami (2013)), or a change of the particle density, resulting from less emitted matter to the eastern jet. A detailed study of the magnetic field around the central engine could shed light on these possibilities.

4.6. Brightness temperature and opening angle

Measuring the brightness temperature T_b and the opening angle of the jet allows us to test the models by Blandford & Königl (1979) and its extension by Königl (1981). It is assumed that the brightness temperature as well as the opening angle have a power law dependence of the core distance with power law indices s and l, respectively. The results obtained in the previous section are used to determine the distribution of $T_{\rm b}$ and the jet width. A linear regression fit to the logarithm of the brightness temperature versus core distance delivers the power law index s and one to the major axis of the Gaussian components the power law index l. The resulting fits are shown in Fig. 4.25. In addition to the brightness temperature and opening angle the plot shows the flux for all components versus separation from the core.

I will assume that synchrotron emission is observed, with potential losses such as inverse Compton scattering, that is frequency dependent. The inverse Compton effect describes the collision of photons with energetic particles and with that an energy gain of photons. In the case of synchrotron radiation the synchrotron photons can be scattered to higher frequency by collisions with particles of the same plasma that produces the synchrotron radiation. This process is known as Synchrotron Self-Compton mechanism (SSC). The losses due to Compton scattering can lead to the so called Compton catastrophe. That is the losses higher than the radiation lead to a decrease in brightness temperature. Kellermann

et al. (1969) derived this maximum possible brightness temperature to $\sim 10^{12}$ K. As there are only values in the range between 10^7 K and 10^{10}K in the reasonable T_b range the scale does not extend up to 10^{12} K. For this reasons Fig. 4.25 shows only components with a maximum brightness temperature of 10^{12} K and only the shown values were used for the fit.

This leads to the conclusion that brightness temperatures that are higher are unlikely to describe a physical process by means of synchrotron radiation. The brightness temperature, as seen in Equ. 2.3.15, depends linearly from the flux density and is inversely proportional to the FWHMs of the Gaussian components. Especially for the core, flux densities are high and the component sizes are very small compared to all other Gaussian components in the jet. This can lead to very high brightness temperature values that can reach up to 10^{20} K or even higher values. These values can not be used to describe the power law that is expected for the brightness temperature gradients along the jet. Unresolved components in the jet should not be included in the analysis, too.

For the eastern jet and western jet, respectively, the fit results in $s_e = -1.16 \pm 0.15$, $s_w = -0.53 \pm 0.24$, $l_e = 0.35 \pm 0.15$, and $l_w = 0.10 \pm 0.14$. The T_b power law index is within $1\,\sigma$ different for the eastern and the western jet, but within $3\,\sigma$ the values are consistent. Within $1\,\sigma$ these values do not fit one of the predictions in the models, since that sets boundaries as $-1.4 \geq s \geq -3$ and $l = 1$. The eastern jet index s_{ej} fits in the models within an interval of $3\,\sigma$, but the western one not. The gradients for the opening angle did not fit the models even in a $3\,\sigma$ interval. Therefore, the strict assumption of a conical jet ($l = 1$) cannot be supported by the given results, the jet seems to be much more collimated than expected.

There is a change in the brightness temperature plot and the major axis power laws at about 1 mas. The slope starting at 1 mas seems to be steeper as below 1 mas. That suggested to have a separated look at the region between 0.2 mas and 1 mas and between 1 mas and 5 mas. The same plots as for the range from 0.2 mas to 5 mas (see Fig. 4.25) were produced for the inner and outer jet (see Fig. 4.26.) Now there are less data points for the fit for both regions, which results in larger errors, though the trend is clear. Within the scope of the errors the values of the eastern jet are consistent for both regions and with the fit to the whole dataset. The case is different for the western jet. A fit to the region starting at 1 mas leads to power law indices of $s = -2.43 \pm 0.37$ and $l = 0.73 \pm 0.37$. The gradient for the inner region is very gentle, even if the values are very vague compared to the errors. These values differ significantly from that obtained by a fit of the whole western jet. Tab. 4.7 summarizes the results.

The results for the western jet between 1 and 5 mas fit very well both the model of Blandford & Königl (1979) and that of Königl (1981). That suggests that, first the western jet behaves different than the eastern jet and second that the geometry of the western jet is different for the inner region than for the outer region.

Table 4.7.: *Brightness temperature power index s ($T_b \propto r^s$) and for the opening angle ($\theta \propto r^l$) of the jet. Fits were made at the regions of 0.2 to 5 mas, 0.2 to 1 mas and 1 to 5 mas from the center. The two latter correspond to the data shown in Fig. 4.26.*

Region [mas]	s_wj	s_ej	l_wj	l_ej
0.2 to 5	-0.57 ± 0.24	-1.16 ± 0.15	0.10 ± 0.14	0.35 ± 0.15
0.2 to 1	-0.18 ± 0.37	-0.96 ± 0.40	-0.13 ± 0.37	0.56 ± 0.40
1 to 5	-2.43 ± 0.37	-1.37 ± 0.43	0.73 ± 0.37	0.60 ± 0.42

Kadler et al. (2004) analyzed the source NGC 1052 at frequencies from 5 to 43 GHz and determined power law indices for the T_b gradient between -3.8 ± 0.3 and -4.1 ± 0.8, for the eastern jet and frequencies of 5, 8.4, 22 and 43 GHz, for the western jet no simple power-law could approximate the data. Therefore he found the T_b gradients to be consistent for all frequencies. The fit performed by Kadler et al. (2004) included data starting at a distance of $r = 2.5$ mas from the central engine whereas in this work only data points below a distance of 0.2 mas from the center were excluded.

Additionally Kadler et al. (2004) analyzed one epoch per frequency while this work presents data from 26 epochs at one frequency of 43 GHz. By including as many observations of one frequency as possible

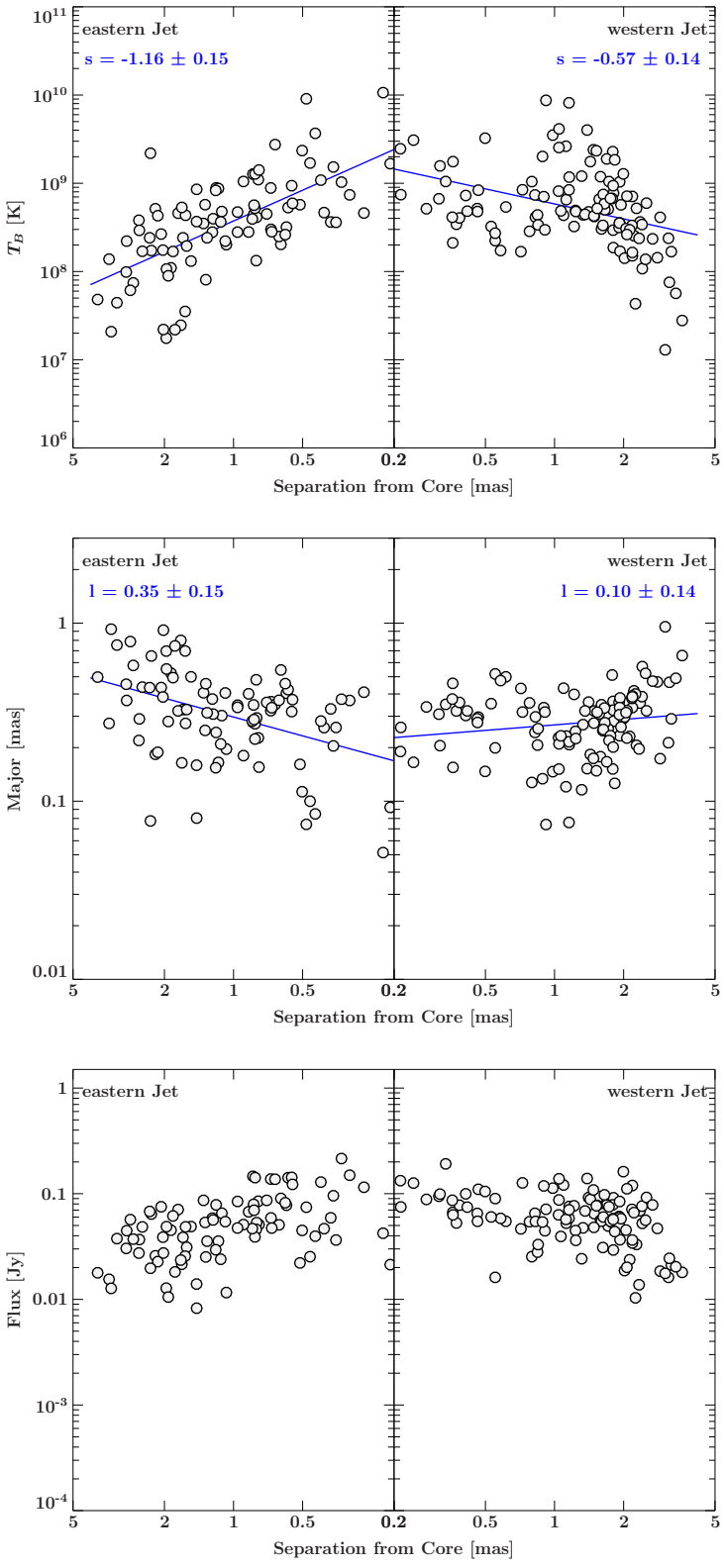

Figure 4.25.: *Brightness temperature (top, component major axis (center) and flux density (bottom) as function of the core distance for the whole jets. The fitted power law indices ($T_b \propto r^{+s}$; $b_{\rm maj} \propto r^{l}$) are shown at each panel.*

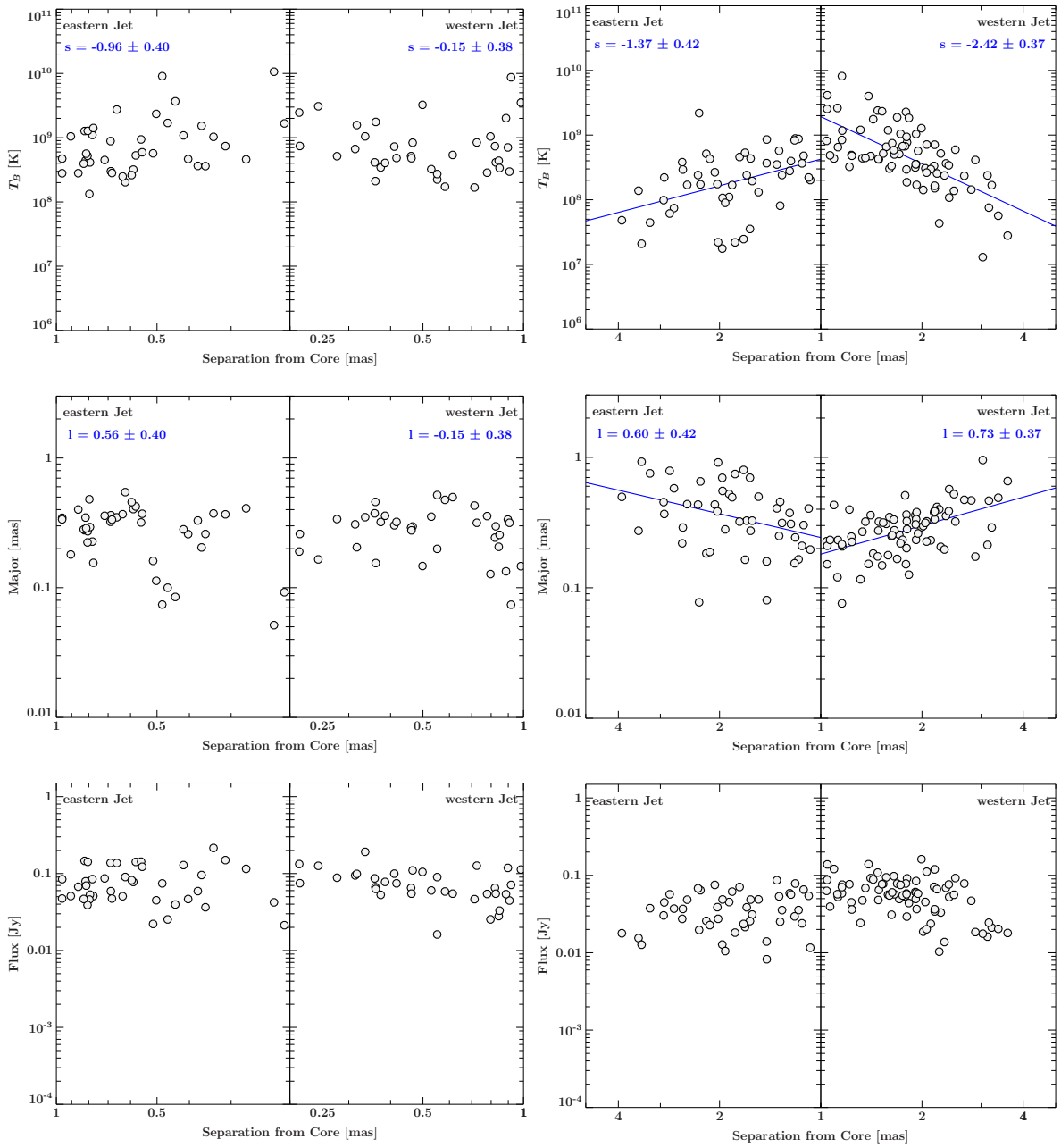

Figure 4.26.: *Brightness temperature (top, component major axis (center) and flux density (bottom) as function of the core distance for the inner (left) and the outer(right) jets. The fitted power law indices ($T_b \propto r^{+s}$; $b_{\rm maj} \propto r^{l}$) are shown at each panel.*

the statistic gets better, the resulting values represent the *mean* of the jets better. For example, it could be that the one observation that was analyzed differs in some aspects from all other observations and the results achieved are not representative for the source. On the other side, Kadler et al. (2004) analyzed the brightness temperature gradients for a multi-frequency observation. This method could reveal frequency-dependent differences. This was not the case.

From Kadler et al. (2004) and this work it seems that the power law index for the brightness temperature gradient increases with increasing distance from the core. This may be explained by a difference

of the jet properties at different distances from the core. The western jet seems to be more collimated inside the inner parsec and this can not be explained by a conical expansion, the index s is far below the predictions of Blandford & Königl (1979) and even didn't reach the range given by Königl (1981). Starting at 1 parsec distance to the core the western jet fits in the model by Blandford & Königl (1979). Namely, it stays relatively collimated but expands conically. The brightness temperature gradient fits well the prediction of the model. Further out, at regions that could not be analyzed in this thesis, the power law index s exceeds the model (Kadler et al. (2004)).

As reported in Sect. 4.3, the western jet is the brighter one for all observations. The brightness temperature plots showed that these of the western jet differ from these for the eastern jet and they are even not consistent for the western jet itself. There is a a change from $s = -0.15 \pm 0.38$ to $s = -2.42 \pm 0.37$ in the power law index at about 1 mas. The stacked map in Fig. 4.12 showed a continuous flux density from 1 to 2 mas, too. This leads to the assumption that there may be a difference in the physical processes in the jet between the region before and after 1 mas in both cases. As the ridge line plots were produced using only the model of CLEAN components and the brightness temperatures were obtained from the model consisting of Gaussian components it is likely that theses observed difference is not caused by a misinterpreting of the model-fitting.

Again, the study of the brightness temperatures at 43 GHz suggests an asymmetry in the jets. Since this can be seen in the overall morphology of the source, in the kinematic analysis and in the gradients in brightness temperature and opening angle, so that it can be assumed that this asymmetry exists for these observations at 43 GHz between 2005 and 2009.

4.7. Conclusion

This work reports first successful 86 GHz observation of the twin jet in NGC 1052. There is a very bright feature between the two jets. A detailed study of the source at 43 GHz and 22 GHz was performed to probe the nature of this bright feature and its relationship with the central SMBH, including 26 observations from 2005 to 2009. Two attempts to verify whether the central feature is the center of the two jets were performed. The first one, based on *phase-referencing*, was unsuccessful.

In contrast, monitoring of the twin-jet system over the 4 years of observation at 43 GHz show hints on the existence of one central feature between the two jets at this frequency, too. Besides that, the western jet was brighter than the eastern one. Earlier studies (see e.g., Kadler et al. (2002)) found the eastern jet to be the brighter one. In addition, the structure of the two jets changes dramatically during the four years. In the period 2005-03 to 2006-04 both jets appear to be extending symmetrically up to 4 mas, but starting at 2007, the extent of the source is smaller and reach not farther than 3 mas away from the center. Furthermore, the western jet become more prominent than the eastern one, its flux density rises higher than the twice of that of the eastern jet. The kinematic analysis show that in 2007 the eastern jet have only very few regions of emission moving very slowly. For the observations after 2008 components could be tracked for the eastern jet again. The kinematic study reveal a trend towards higher velocities for the eastern jet and constrain the center of ejection to be in the region around the central feature. Combining the derived flux density ratios and velocities I estimated the viewing angle of the twin jet system for the different time blocks and for each jet individually. There is a small range of apparent speeds with the same values for all observations. If the jets are intrinsically the same, the angle to the line of sight has to change between 2006 and 2007 from the lowest possible angle of 84° (in 2006) to the highest possible angle of 80° (for 2007 to 2009) (assuming 1σ Gaussian errors for flux ratio and velocity).

I could prove that the brightness temperature in the western jet has a power-law dependence of the core distance that is different before and after 1 mas, but that of the eastern jet is with $s = -1.16 \pm 0.15$ consistent from 0.2 to 5 mas. From 0.2 to 1 mas I derived a power-law index of $s = -0.15 \pm 0.38$ and from 1 to 5 mas an index of $s = -2.43 \pm 0.37$ for the western jet. The opening angle of the western jet changes from $l = -0.15 \pm 0.38$ to $l = 0.73 \pm 0.37$, whereas that of the eastern jet is constant with $l = 0.35 \pm 0.15$.

Summarizing this work, I verified that the central feature of NGC 1052 at 43 GHz is a stationary feature. By considering that the same region is observed at 86 GHz this conclusion can be extrapolated to the higher frequency. In addition, the source showed asymmetries in the overall structure, as well as for single parameters, such as the velocity and the brightness temperature gradient. It is possible to explain the observed parameters with a change of the angle to the line of sight. All other analyzing methods show an asymmetry of western and eastern jet. Consequently, the asymmetry seems to be the better explanation of the results. In this case there are mainly two possibilities that may lead to an intrinsic asymmetry: either the magnetic field is asymmetric, for example caused by an asymmetry in the accretion disk (Fendt & Sheikhnezami, 2013), or a change in the particle density. Further studies of the magnetic field may reveal the preferred option. For example, this is possible by deriving the magnetic field strength out of synchrotron cooling, a larger magnetic flux in the eastern jet could be the reason for the drop of flux density in the eastern jet in 2007. These calculations could be made, too, for the drop in flux density in the western jet below a distance of 2 mas from the core, that has a different slope from 2006-2007, in 2007 and from 2008-2009. From this kind of analysis a difference in the magnetic field for the western and eastern jet could be found. As the morphology of the source appears to change a lot at time scales smaller than a year, including more observations at 43 GHz would improve the understanding of the twin-jet in NGC 1052.

As the results obtained from the observations analyzed in this thesis differ from earlier studies, a good way to verify the observed asymmetry and to find the reason for it would be to conduct more simultaneous multi-frequency observations of NGC 1052 including 43 GHz and lower frequencies. As earlier studies already showed, free-free absorption is likely to happen at lower frequencies, resulting in the high absorption of the inner western jet. It is possible that there are deviations from these results at different observing dates, resulting, for example, in a higher absorption in the western jet. Further analysis of the spectral indices and the core-shift in NGC 1052 are needed to shed more light on the observed asymmetry.

5 | Summary & outlook

4 years of observation at 43 GHz of the Liner radio-galaxy NGC 1052 with the Very Long Baseline Array (VLBA) were presented. This source is due to an inclination angle close to the line of sight and the up to 86 GHz visible two jets a perfect source to study the innermost region of AGN.

The sources morphology at 43 GHz revealed a possible asymmetry in the jets and the flux density ratio of western to eastern jet changes from nearly one to above 2. A kinematic study showed a trend towards higher velocities for the eastern jet. The combination of the derived velocities and the flux density ratios gave an estimate on the angle to the line of sight. To fulfill the assumption of intrinsically the same brightness and velocities for both jets the only possibility (assuming 1σ Gaussian errors) is that the inclination angle has to change from 84° to 80° from 2006 to 2007.

There are mainly two possibilities that can lead to the observed asymmetry: a change of the angle of the jets to the line of sight or an intrinsic asymmetry. From all applied methods of analysis the best explanation of the results is the second one. Besides different intrinsic velocities or particle densities, there could be an asymmetric magnetic field or additional external absorption leading to an intrinsic asymmetry. For further constraints, a more detailed study of the 43 GHz observations analyzed in this thesis, with special emphasis on the synchrotron cooling times, could be made. Since earlier studies showed a different morphology of the source it is needed to test current understandings of the source structure of NGC 1052 by conducting more multi-frequency observations, for example to test the current models of the location of a free-free absorbing torus. The existence of further external media have to be proofed, as is possible by further analysis of the core-shift and spectrum in the ratio waveband.

In the future the same analysis could be repeated for the 22 GHz data. But at this frequency the torus is not optical thin, yet. The analysis at 43 GHz showed, that this frequency is a good starting point for testing the jet geometry, more observations could verify the achieved velocities.

As the source is bright enough to observe at 86 GHz it would be very interesting to apply a kinematic study at higher frequencies than 43 GHz and to test brightness temperature gradients and the orientation of the system. Earlier results and that from this thesis suggest different observational properties at different regions of the system. These different regions can be examined by observations at different frequencies. Only the combination of different observing frequencies, including the highest one possible, could reveal the origin of the in this work observed deviation from earlier studies and the standard model.

Bibliography

Acciari V.A., Aliu E., Arlen T., et al., 2009, Science 325, 444

Antonucci R., 1993, Ann. Rev. Astron. Astrophys. 31, 473

Baczko A.K., 2012, B.Sc. thesis, Friedrich-Alexander-Universität Erlangen-Nürnberg

Beasley A.J., Conway J.E., 1995, In: Zensus J.A., Diamond P.J., Napier P.J. (eds.) Very Long Baseline Interferometry and the VLBA, Vol. 82. Astronomical Society of the Pacific Conference Series, p. 327

Beasley A.J., Gordon D., Peck A.B., et al., 2002, ApJS 141, 13

Blakeslee J.P., Jordán A., Mei S., et al., 2009, ApJ 694, 556

Blandford R.D., Königl A., 1979, ApJ 232, 34

Boettcher M., Harris D.E., Krawczynski H., 2012, Relativistic Jets from Active Galactic Nuclei, Wiley

Briggs D.S., Schwab F.R., Sramek R.A., 1999, In: Taylor G.B., Carilli C.L., Perley R.A. (eds.) Synthesis Imaging in Radio Astronomy II, Vol. 180. Astronomical Society of the Pacific Conference Series, p. 127

Burke B.F., Graham-Smith F., 2009, An Introduction to Radio Astronomy, Cambridge University Press, Cambridge, United Kingdom

Böck M., 2012, Ph.D. thesis, Friedrich-Alexander-Universität Erlangen-Nürnberg

Clark B.G., 1999, In: Taylor G.B., Carilli C.L., Perley R.A. (eds.) Synthesis Imaging in Radio Astronomy II, Vol. 180. Astronomical Society of the Pacific Conference Series, p. 1

Cornwell T., Braun R., Briggs D.S., 1999, In: Taylor G.B., Carilli C.L., Perley R.A. (eds.) Synthesis Imaging in Radio Astronomy II, Vol. 180. Astronomical Society of the Pacific Conference Series, p. 151

Denicoló G., Terlevich R., Terlevich E., et al., 2005, MNRAS 356, 1440

Doeleman S.S., Fish V.L., Schenck D.E., et al., 2012, Science 338, 355

Fanaroff B.L., Riley J.M., 1974, MNRAS 167, 31P

Fendt C., Sheikhnezami S., 2013, ApJ 774, 12

Fomalont E.B., Perley R.A., 1999, In: Taylor G.B., Carilli C.L., Perley R.A. (eds.) Synthesis Imaging in Radio Astronomy II, Vol. 180. Astronomical Society of the Pacific Conference Series, p. 79

Fosbury R.A.E., Mebold U., Goss W.M., Dopita M.A., 1978, MNRAS 183, 549

Gebhardt K., Adams J., Richstone D., et al., 2011, ApJ 729, 119

Hada K., Doi A., Kino M., et al., 2011, Nature 477, 185

Hartigan P., Hillenbrand L., 2009, ApJ 705, 1388

Hjellming R.M., Johnston K.J., 1981, Astrophys. J., Lett. 246, L141

Ho L.C., Filippenko A.V., Sargent W.L.W., 1997, ApJS 112, 315

Kadler M., Ros E., Lobanov A.P., et al., 2004, A&A 426, 481

Kadler M., Ros E., Zensus J.A., et al., 2002, ArXiv: astro-ph/0204054

Kellermann K.I., Pauliny-Toth I.I.K., Williams P.J.S., 1969, ApJ 157, 1

Kellermann K.I., Vermeulen R.C., Cohen M.H., Zensus J.A., 1999, In: American Astronomical Society Meeting Abstracts #194, Vol. 31. Bulletin of the American Astronomical Society, p. 856

Kellermann K.I., Vermeulen R.C., Zensus J.A., Cohen M.H., 1998, AJ 115, 1295

Königl A., 1981, ApJ 243, 700

Kovalev Y.Y., Kellermann K.I., Lister M.L., et al., 2005, AJ 130, 2473

Krolik J., 1999, Active galactic nuclei : from the central black hole to the galactic environment,

Princeton University Press
Lister M.L., Cohen M.H., Homan D.C., et al., 2009, AJ 138, 1874
Lobanov A.P., 1998, A&AS 132, 261
Lobanov A.P., 2005, ArXiv: astro-ph/0503225
Ly C., Walker R.C., Junor W., 2007, ApJ 660, 200
Margon B., Anderson S.F., 1989, ApJ 347, 448
Martí-Vidal I., Krichbaum T.P., Marscher A., et al., 2012, A&A 542, A107
Mayall N.U., 1939, PASP 51, 282
Napier P.J., 1999, In: Taylor G.B., Carilli C.L., Perley R.A. (eds.) Synthesis Imaging in Radio Astronomy II, Vol. 180. Astronomical Society of the Pacific Conference Series, p. 37
NRAO 2011, AIPS COOKBOOK, The National Radio Astronomy Observatory
Pacholczyk A.G., 1970, Radio Astrophysics, W. H. Freeman and Company, USA
Ros E., Kadler M., 2008, Journal of Physics Conference Series 131, 012056
Rybicki G., Lightman A., 2004, Radiative Processes in Astrophysik, Wiley, New York, USA
Schneider P., 2008, Einführung in die Extragalaktisch Astronomie und Kosmologie, Springer
Schwab F.R., Cotton W.D., 1983, AJ 88, 688
Shepherd M.C., Pearson T.J., Taylor G.B., 1994, In: BAAS, Vol. 26. Bulletin of the American Astronomical Society, p.987
Taylor G., Carilli C., Preley R., 1999, Synthesis imaging in radio astronomy II, Vol. 180, Astronomical Society of the Pacific Conference Series
Thompson A., Moran J., Sweson J.G., 2001, Interferometry and Synthesis in Radio Astronomy,2nd Edition, Wiley, New York, USA
Thompson A.R., 1999, In: Taylor G.B., Carilli C.L., Perley R.A. (eds.) Synthesis Imaging in Radio Astronomy II, Vol. 180. Astronomical Society of the Pacific Conference Series, p. 11
Urry C.M., Padovani P., 1995, PASP 107, 803
Vermeulen R.C., Ros E., Kellermann K.I., et al., 2003, A&A 401, 113
Woitas J., Ray T.P., Bacciotti F., et al., 2002, ApJ 580, 336
Wrobel J.M., 1984, ApJ 284, 531

A | Appendix

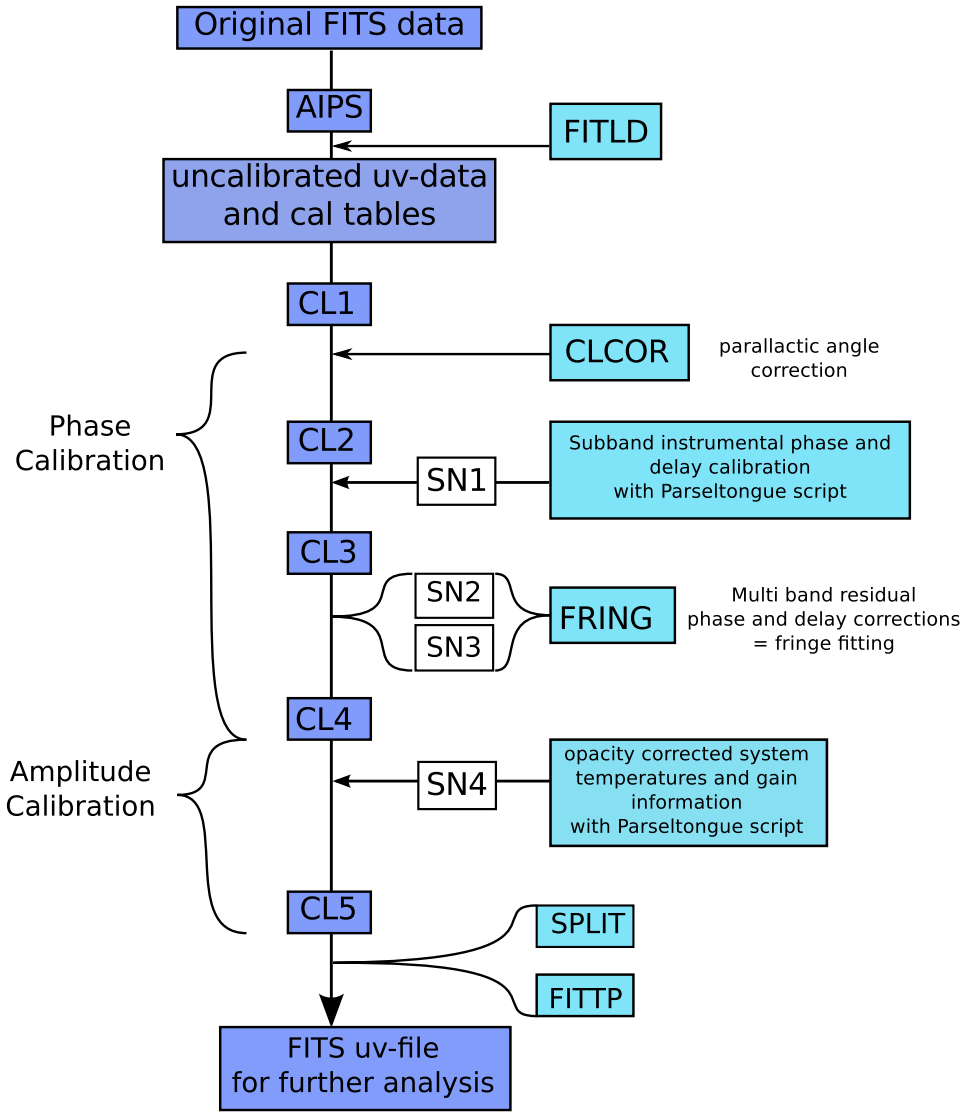

Figure A.1.: *Block diagram of the calibration routine that is done in AIPS for the case of the 86 GHz observation with the GMVA.*

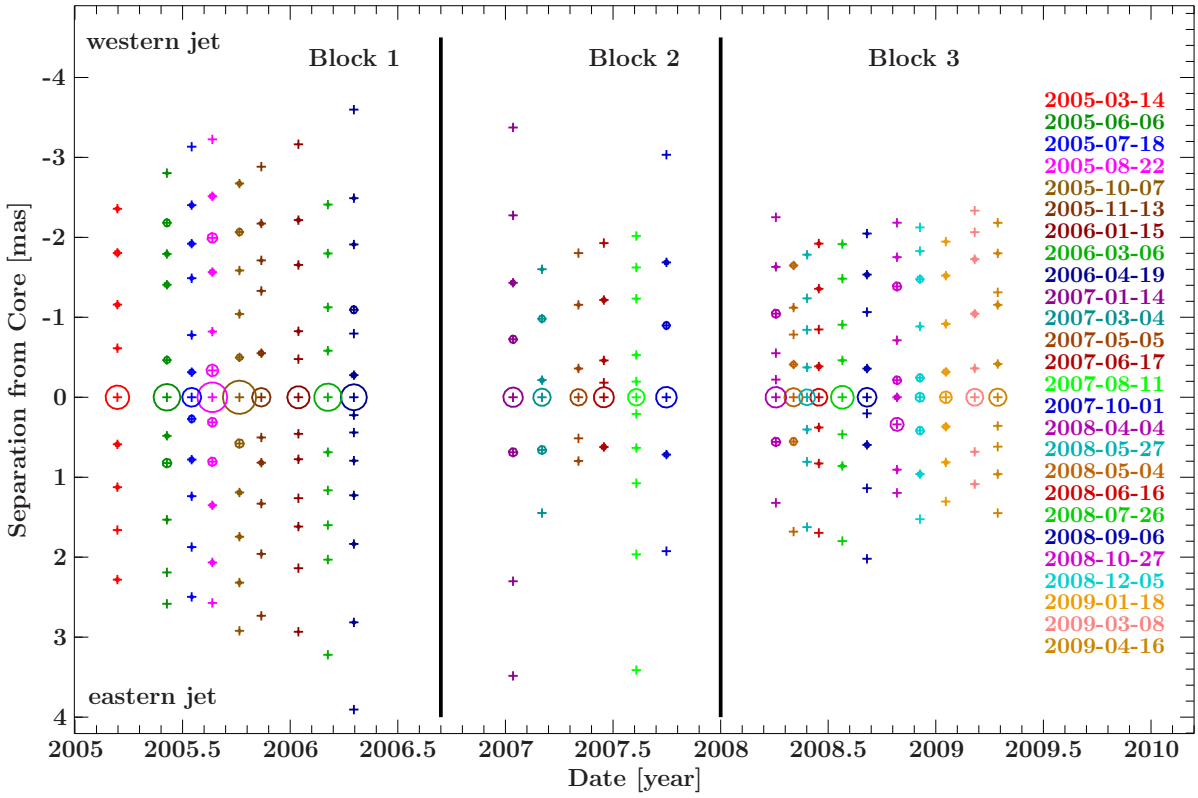

Figure A.2.: *Time evolution of model components. The color is sorted by the observation date. The size of the Components corresponds to the relative flux. Components that are not assigned are black. The eastern jet model is plotted in the lower lower half of the plot, the western jet in the upper half of the plot.*

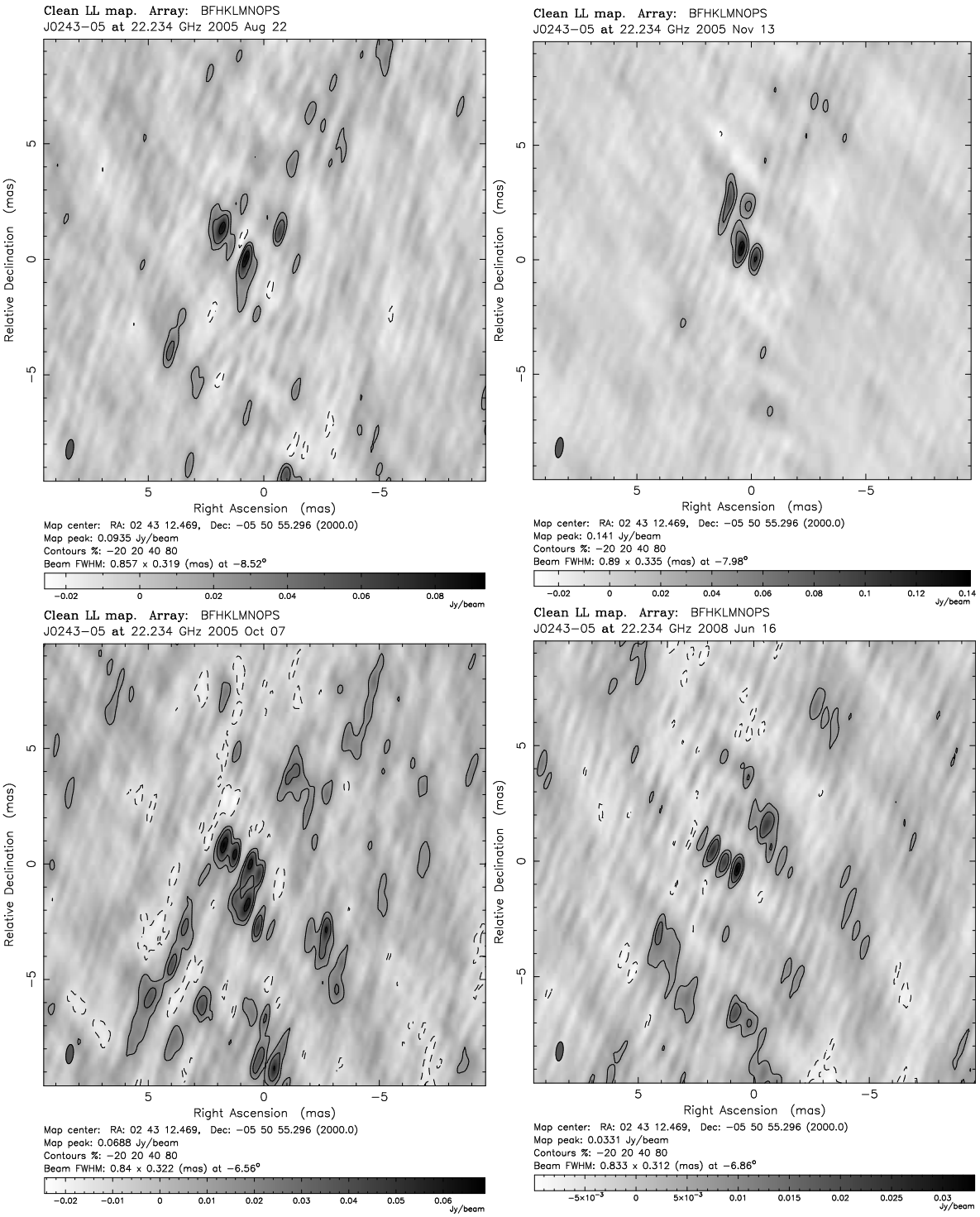

Figure A.3.: *Phase referenced map for observations BR099E (top left), BR099F (bottom left), BR099G (top right), BR130B (bottom right) without the use of clean boxes*

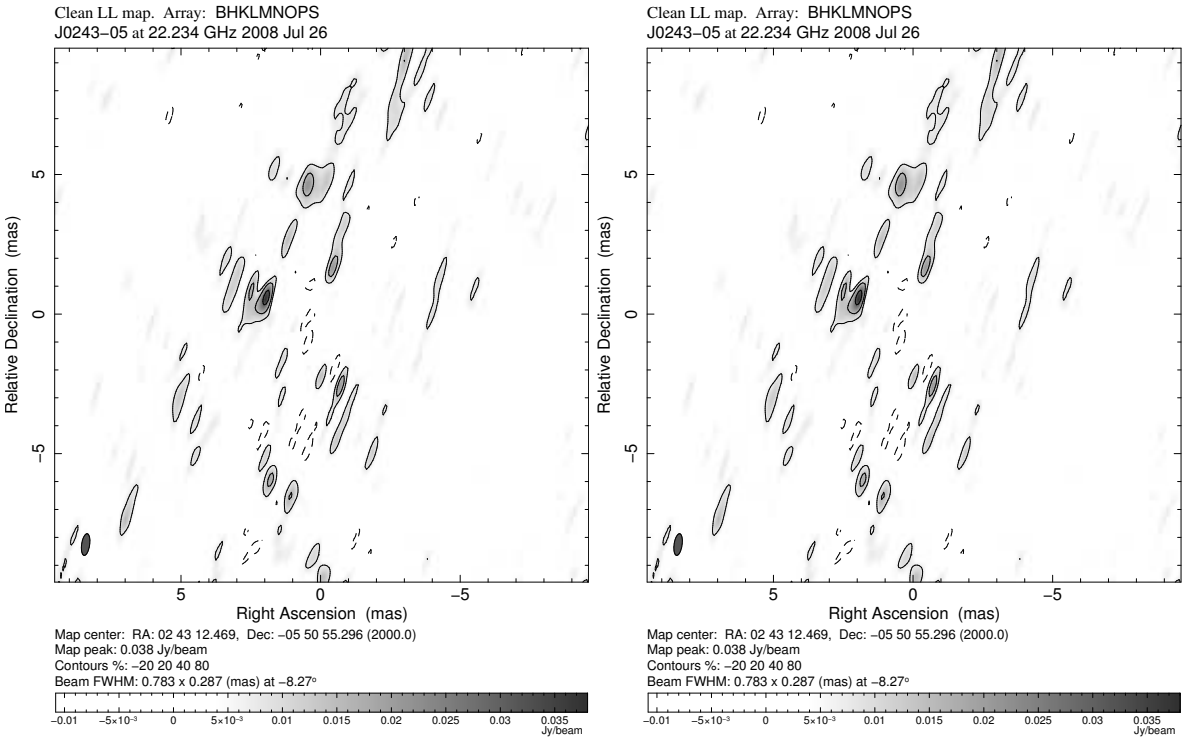

Figure A.4.: *Phase referenced map for observations BR099E (left) and BR099F (right) without the use of clean boxes*

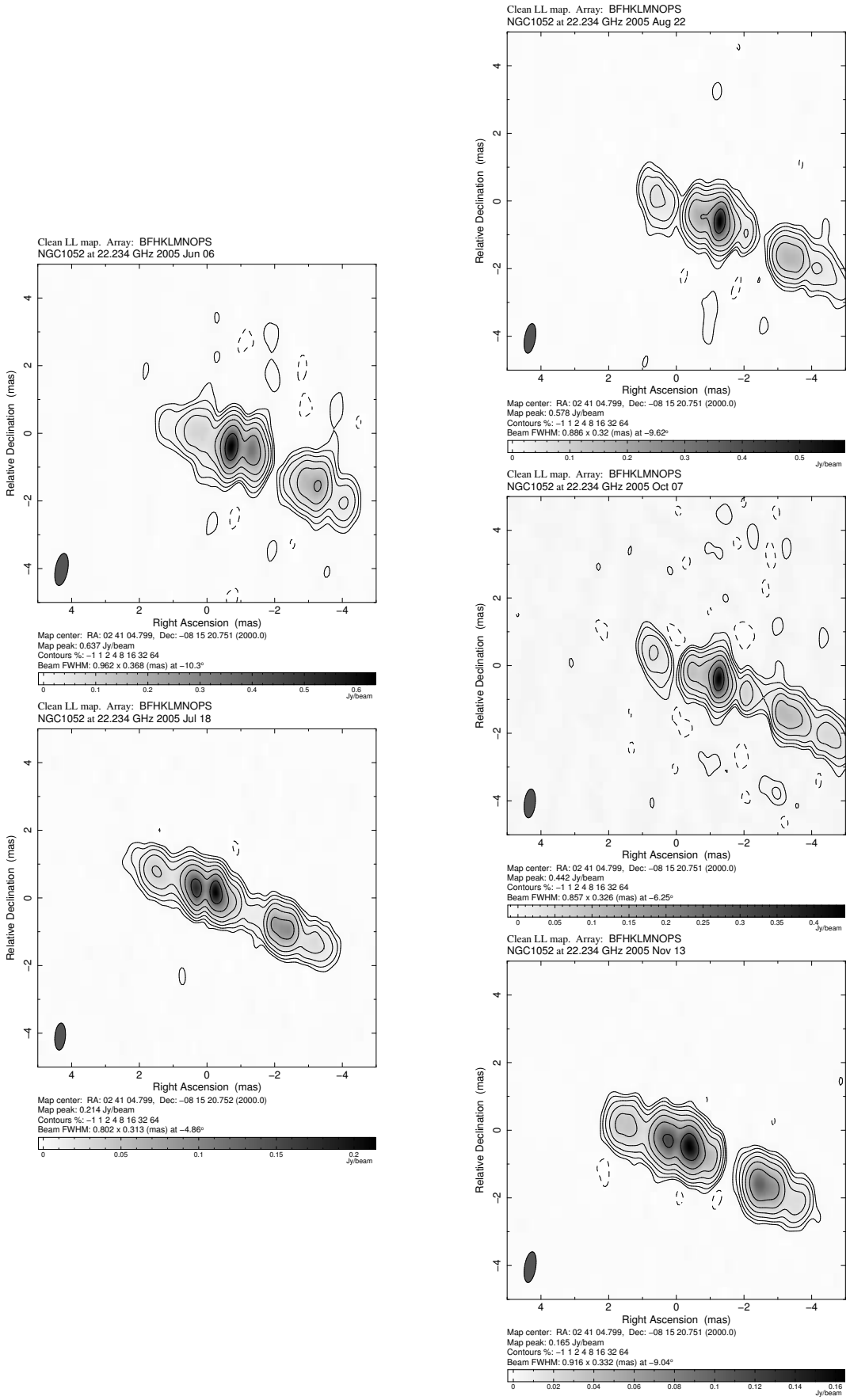

Figure A.5.: *Shifts due to results as in Tab.4.1 for BR099C(top left),BR099D(bottom left),BR099E(top right), BR099F(middle right) and BR099D(bottom right). Obviously there are remaining errors that distort the resulting shifts in the phase-referenced map.*

Table A.1.: *Flux densities of the whole source, the core, the western and the eastern jet and the flux density ratio of western to eastern jet for the analyzed observations and the corresponding observation date. The flux densities of all Gaussian components in the models were summed up for the specified region of the source.*

Obs. Code	Obs. date	S_{tot} [Jy]	S_{core} [Jy]	S_{west} [Jy]	S_{east} [Jy]	$S_{\mathrm{west}}/S_{\mathrm{east}}$
BR099A	2005-Mar-14	0.92	0.38	0.29	0.25	1.18
BR099C	2005-Jun-06	1.20	0.43	0.45	0.32	1.38
BR099D	2005-Jul-18	1.05	0.31	0.39	0.35	1.11
BR099E	2005-Aug-22	1.60	0.48	0.63	0.49	1.28
BR099F	2005-Oct-07	1.35	0.53	0.41	0.40	1.03
BR099G	2005-Nov-13	0.84	0.30	0.28	0.26	1.05
BR099I	2006-Jan-15	0.81	0.36	0.23	0.21	1.09
BR119A	2006-Mar-06	0.86	0.44	0.22	0.20	1.10
BR119B	2006-Apr-19	1.12	0.42	0.37	0.33	1.13
BR120A	2007-Jan-14	0.76	0.32	0.27	0.17	1.55
BR120B	2007-Mar-04	0.67	0.28	0.24	0.15	1.67
BR120C	2007-May-05	0.49	0.27	0.15	0.07	2.27
BR120D	2007-Jun-17	0.62	0.35	0.18	0.09	1.98
BR120E	2007-Aug-11	0.57	0.30	0.15	0.11	1.42
BR120F	2007-Oct-01	0.65	0.33	0.21	0.10	2.21
BR120H	2008-Apr-04	0.74	0.33	0.24	0.17	1.41
BR120I	2008-May-27	0.54	0.26	0.17	0.11	1.53
BR130A	2008-May-04	0.71	0.29	0.27	0.14	1.89
BR130B	2008-Jun-16	0.64	0.28	0.24	0.13	1.85
BR130C	2008-Jul-26	0.68	0.37	0.20	0.11	1.78
BR130D	2008-Sep-06	0.71	0.31	0.25	0.15	1.63
BR130E	2008-Oct-27	0.79	0.09	0.41	0.30	1.38
BR130F	2008-Dec-05	0.73	0.15	0.36	0.23	1.58
BR130G	2009-Jan-18	0.70	0.19	0.31	0.20	1.52
BR130H	2009-Mar-08	0.64	0.28	0.26	0.10	2.55
BR130I	2009-Apr-16	0.66	0.28	0.26	0.11	2.36

Table A.2.: *Velocity of each tracked component in units of mas per year and apparant velocity β in units of* c. *Velocities were derived with a linear regression fit for all components, that could be tracked over at least four epochs.*

Comp.	velocity [mas yr^{-1}]	$\beta[c]$	Comp.	velocity [mas yr^{-1}]	$\beta[c]$
wj1	-2.05 ± 3.04	-0.61 ± 0.91	ej1	2.02 ± 1.20	0.61 ± 0.36
wj2	-1.61 ± 1.08	-0.48 ± 0.32	ej2	2.21 ± 1.17	0.66 ± 0.35
wj3	-0.77 ± 1.23	-0.23 ± 0.37	ej3	2.08 ± 1.08	0.62 ± 0.32
wj4	-0.78 ± 1.86	-0.23 ± 0.56	ej4	1.98 ± 1.52	0.59 ± 0.46
wj5	-1.71 ± 1.23	-0.51 ± 0.37	ej5	2.22 ± 1.46	0.66 ± 0.44
wj6	-1.19 ± 1.46	-0.36 ± 0.44	ej6	1.80 ± 3.12	0.54 ± 0.93
wj7	-	-	ej7	-	-
wj8	-1.05 ± 2.20	-0.31 ± 0.66	ej8	-	-
wj9	-1.13 ± 1.67	-0.34 ± 0.50	ej9	-	-
wj10	-1.08 ± 2.22	-0.32 ± 0.66	ej10	0.45 ± 3.25	0.13 ± 0.97
wj11	-0.76 ± 1.16	-0.23 ± 0.35	ej11	1.39 ± 2.91	0.41 ± 0.87
wj12	-1.09 ± 0.89	-0.33 ± 0.27	ej12	1.41 ± 1.86	0.42 ± 0.55
wj13	-1.19 ± 0.89	-0.35 ± 0.27	ej13	1.40 ± 1.68	0.42 ± 0.50
wj14	-0.88 ± 0.89	-0.26 ± 0.27	ej14	2.09 ± 1.97	0.62 ± 0.59
wj15	-0.44 ± 2.65	-0.13 ± 0.79	ej15	-	-

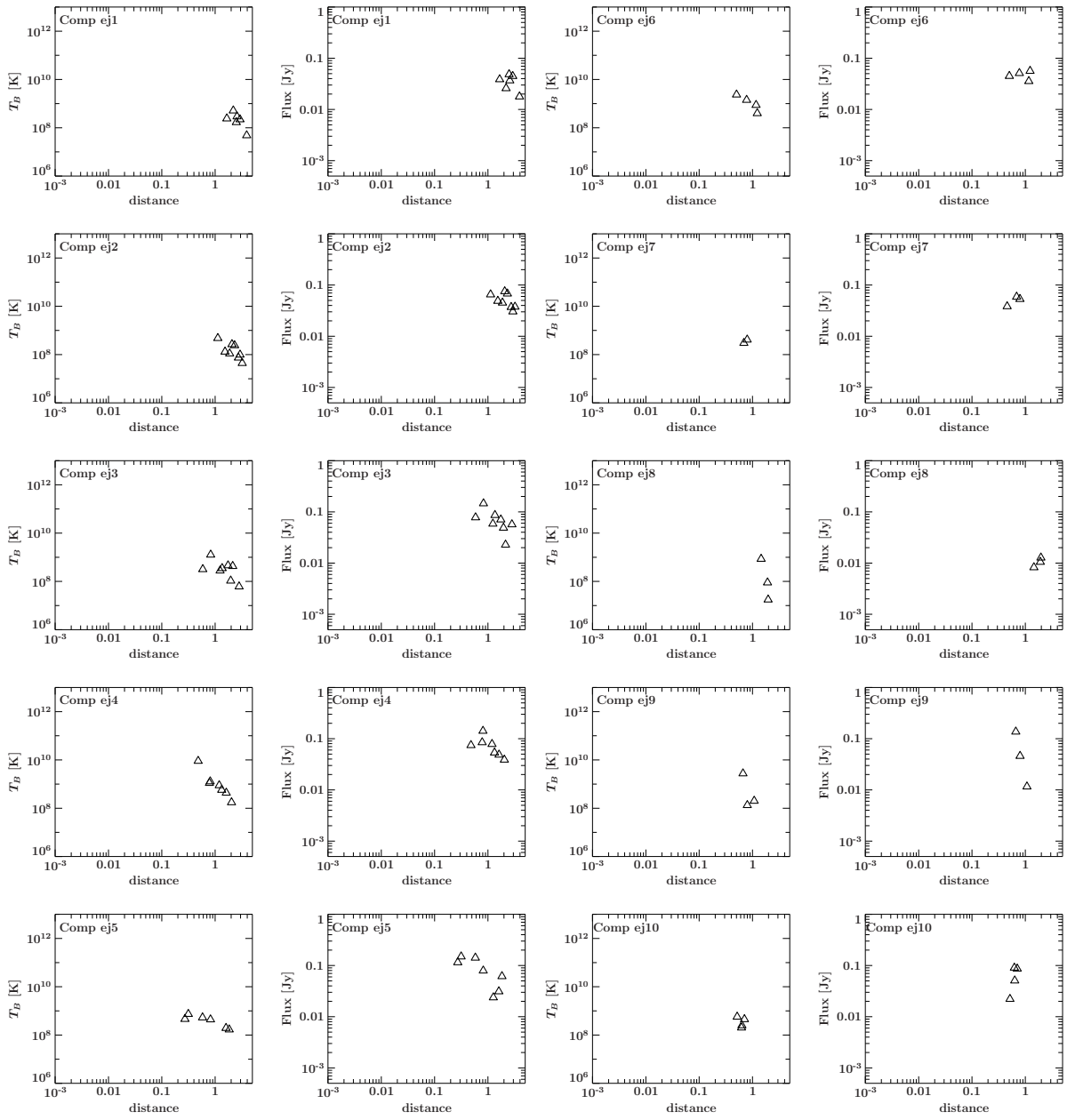

Figure A.6.: *Distance vs Tb and Flux for every component*

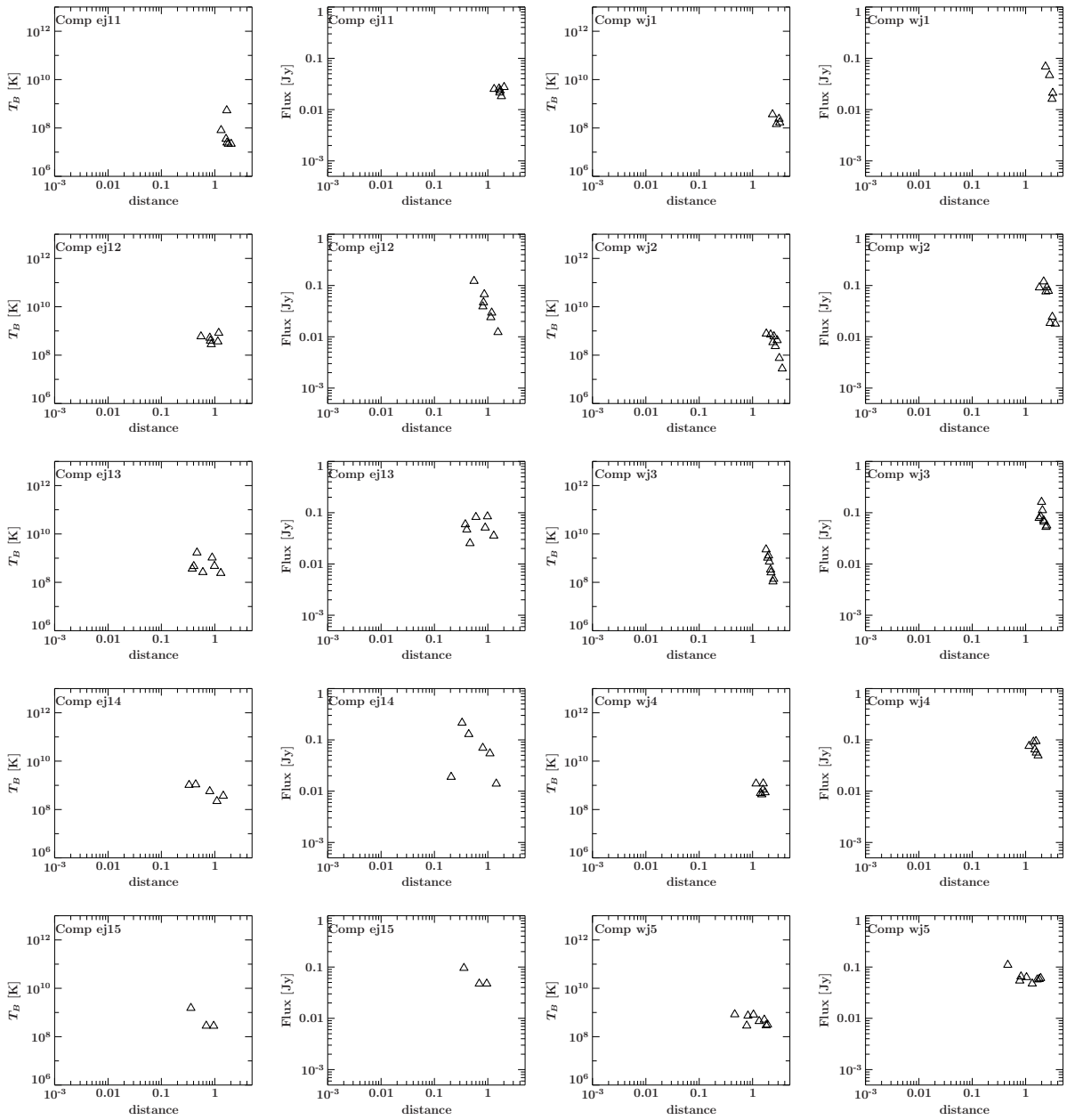

Figure A.7.: *Distance vs Tb and Flux for every component*

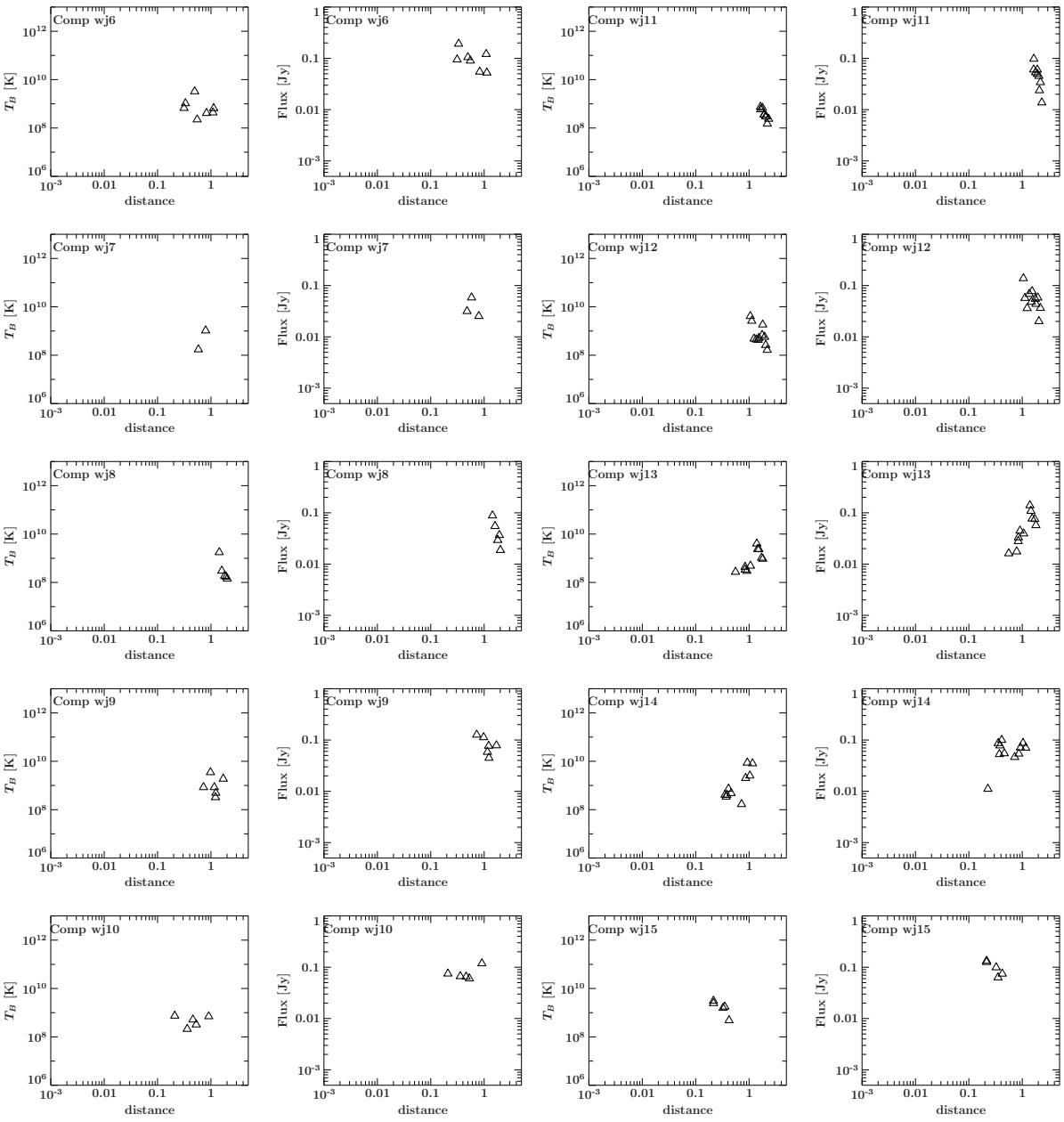

Figure A.8.: *Distance vs Tb and Flux for every component*

Table A.3.: *Parameters for all components of epochs BR099A, BR099C, BR099D and BR099E (from top to bottom)*

Component	S_{tot} [Jy]	Distance [mas]	P.A. [°]	Major [mas]	T_{b}
wj1	0.07	-2.36	0.00	0.36	3.64e+08
wj2	0.09	-1.81	0.00	0.28	7.72e+08
wj4	0.08	-1.16	0.00	0.21	1.17e+09
	0.05	-0.62	23.84	0.50	5.38e+08
core	0.38	-0.00	43.83	0.15	0.00e+00
ej3	0.08	0.59	0.00	0.40	3.19e+08
ej2	0.07	1.12	0.00	0.30	4.78e+08
ej1	0.04	1.66	0.00	0.33	2.41e+08
	0.06	2.28	40.86	0.65	1.73e+08

Component	S_{tot} [Jy]	Distance [mas]	P.A. [°]	Major [mas]	T_{b}
wj1	0.05	-2.80	0.00	0.47	1.43e+08
wj2	0.12	-2.18	0.00	0.34	7.10e+08
wj3	0.08	-1.79	0.00	0.15	2.28e+09
wj4	0.09	-1.40	0.00	0.36	4.74e+08
wj5	0.11	-0.46	0.00	0.30	8.35e+08
core	0.43	-0.01	5.50	0.13	4.31e+10
ej4	0.07	0.48	0.00	0.07	9.06e+09
ej3	0.15	0.82	0.00	0.28	1.27e+09
ej2	0.05	1.53	0.00	0.50	1.31e+08
ej1	0.03	2.19	0.00	0.18	5.14e+08
	0.03	2.59	0.00	0.22	3.81e+08

Component	S_{tot} [Jy]	Distance [mas]	P.A. [°]	Major [mas]	T_{b}
wj1	0.02	-3.13	0.00	0.21	2.38e+08
wj2	0.08	-2.40	0.00	0.39	3.41e+08
wj3	0.08	-1.92	0.00	0.23	1.04e+09
wj4	0.06	-1.49	0.00	0.32	4.20e+08
wj5	0.05	-0.78	0.00	0.36	2.85e+08
wj6	0.09	-0.31	0.00	0.31	6.67e+08
core	0.31	0.00	18.66	0.10	0.00e+00
ej5	0.12	0.27	0.00	0.41	4.59e+08
ej4	0.08	0.78	0.00	0.23	1.10e+09
ej3	0.06	1.24	0.00	0.37	2.79e+08
ej2	0.05	1.87	0.00	0.52	1.10e+08
ej1	0.05	2.50	0.00	0.44	1.70e+08

Component	S_{tot} [Jy]	Distance [mas]	P.A. [°]	Major [mas]	T_{b}
wj1	0.02	-3.22	0.00	0.29	1.68e+08
wj2	0.09	-2.51	0.00	0.32	5.95e+08
wj3	0.16	-1.99	0.00	0.29	1.28e+09
wj4	0.09	-1.56	0.00	0.31	6.59e+08
wj5	0.07	-0.82	0.00	0.24	7.37e+08
wj6	0.19	-0.33	0.00	0.35	1.05e+09
core	0.48	0.00	12.03	0.18	0.00e+00
ej5	0.15	0.31	0.00	0.37	7.38e+08
ej4	0.14	0.81	0.00	0.27	1.28e+09
ej3	0.09	1.35	0.00	0.41	3.50e+08
ej2	0.08	2.07	0.00	0.43	2.66e+08
ej1	0.04	2.57	0.00	0.29	2.93e+08

Table A.4.: *Parameters for all components of epoch BR099F, BR099G, BR099I and BR119A (from top to bottom)*

Component	$S_{\rm tot}$ [Jy]	Distance [mas]	P.A. [°]	Major [mas]	$T_{\rm b}$
wj2	0.08	-2.67	0.00	0.47	2.35e+08
wj3	0.11	-2.06	0.00	0.32	7.13e+08
wj4	0.06	-1.58	0.00	0.18	1.19e+09
wj5	0.06	-1.04	0.00	0.23	8.15e+08
wj6	0.10	-0.50	0.00	0.15	3.24e+09
core	0.53	0.01	0.00	0.08	5.49e+10
ej5	0.14	0.58	0.00	0.42	5.30e+08
ej4	0.08	1.19	0.00	0.24	8.86e+08
ej3	0.07	1.75	0.00	0.32	4.57e+08
ej2	0.07	2.32	0.00	0.43	2.41e+08
ej1	0.04	2.92	0.00	0.37	2.21e+08

Component	$S_{\rm tot}$ [Jy]	Distance [mas]	P.A. [°]	Major [mas]	$T_{\rm b}$
wj2	0.02	-2.88	0.00	0.17	4.11e+08
wj3	0.07	-2.17	0.00	0.38	3.33e+08
wj4	0.05	-1.71	0.00	0.25	5.09e+08
wj5	0.05	-1.33	0.00	0.27	4.39e+08
wj6	0.09	-0.55	0.00	0.52	2.24e+08
core	0.30	0.00	0.00	0.09	2.50e+10
ej6	0.04	0.50	0.00	0.11	2.35e+09
ej5	0.08	0.82	0.00	0.35	4.40e+08
ej4	0.05	1.33	0.00	0.25	5.72e+08
ej3	0.05	1.96	0.00	0.55	1.07e+08
ej2	0.04	2.73	0.00	0.58	7.42e+07

Component	$S_{\rm tot}$ [Jy]	Distance [mas]	P.A. [°]	Major [mas]	$T_{\rm b}$
wj2	0.02	-3.16	0.00	0.47	7.55e+07
wj3	0.07	-2.22	0.00	0.42	2.55e+08
wj5	0.06	-1.66	0.00	0.28	5.01e+08
wj6	0.05	-0.83	0.00	0.30	4.13e+08
wj7	0.03	-0.48	0.00	0.00	0.00e+00
core	0.36	-0.00	0.00	0.07	4.73e+10
ej7	0.04	0.46	0.00	0.00	0.00e+00
ej6	0.05	0.77	0.00	0.16	1.41e+09
ej5	0.02	1.26	0.00	0.00	1.11e+20
ej4	0.05	1.62	0.00	0.27	4.34e+08
ej3	0.02	2.14	0.00	0.19	4.29e+08
ej2	0.03	2.93	0.00	0.45	9.87e+07

Component	$S_{\rm tot}$ [Jy]	Distance [mas]	P.A. [°]	Major [mas]	$T_{\rm b}$
wj3	0.05	-2.41	0.00	0.57	1.08e+08
wj5	0.06	-1.80	0.00	0.36	2.94e+08
wj6	0.05	-1.12	0.00	0.23	6.51e+08
wj7	0.06	-0.58	0.00	0.48	1.73e+08
core	0.44	-0.00	40.59	0.09	4.36e+18
ej7	0.06	0.69	0.00	0.36	3.01e+08
ej6	0.04	1.17	0.00	0.17	8.73e+08
ej5	0.03	1.60	0.00	0.33	1.95e+08
ej4	0.04	2.03	0.00	0.38	1.75e+08
ej2	0.04	3.22	0.00	0.75	4.43e+07

Table A.5.: *Parameters for all components of epoch BR119B, BR120A, BR120B, BR120C and BR120D (from top to bottom)*

Component	S_{tot} [Jy]	Distance [mas]	P.A. [°]	Major [mas]	T_{b}
wj2	0.02	-3.60	0.00	0.66	2.78e+07
wj3	0.06	-2.49	0.00	0.52	1.37e+08
wj5	0.06	-1.91	0.00	0.36	3.15e+08
wj6	0.12	-1.09	0.00	0.43	4.34e+08
wj7	0.03	-0.80	0.00	0.13	1.04e+09
	0.09	-0.28	0.00	0.34	5.15e+08
core	0.42	-0.00	12.03	0.14	0.00e+00
	0.04	0.22	0.00	0.05	1.06e+10
	0.04	0.44	0.00	0.08	3.68e+09
ej7	0.05	0.79	0.00	0.29	4.13e+08
ej6	0.06	1.23	0.00	0.31	3.97e+08
ej5	0.06	1.84	0.00	0.49	1.69e+08
ej3	0.06	2.82	0.00	0.79	6.12e+07
ej1	0.02	3.91	0.00	0.50	4.82e+07

Component	S_{tot} [Jy]	Distance [mas]	P.A. [°]	Major [mas]	T_{b}
	0.02	-3.37	0.00	0.49	5.66e+07
	0.03	-2.28	0.00	0.21	5.20e+08
wj8	0.09	-1.43	0.00	0.18	1.76e+09
wj9	0.13	-0.73	0.00	0.32	8.43e+08
core	0.32	-0.00	0.00	0.18	6.48e+09
	0.14	0.69	0.00	0.32	8.85e+08
	0.02	2.30	0.00	0.08	2.19e+09
	0.02	3.48	0.00	0.27	1.38e+08

Component	S_{tot} [Jy]	Distance [mas]	P.A. [°]	Major [mas]	T_{b}
wj8	0.05	-1.60	0.00	0.35	3.03e+08
wj9	0.11	-0.98	0.00	0.15	3.51e+09
wj10	0.07	-0.21	0.00	0.26	7.43e+08
core	0.28	0.00	26.09	0.14	1.63e+10
ej9	0.14	0.66	73.04	0.35	2.75e+09
ej8	0.01	1.45	0.00	0.08	8.53e+08

Component	S_{tot} [Jy]	Distance [mas]	P.A. [°]	Major [mas]	T_{b}
wj8	0.03	-1.80	0.00	0.32	1.86e+08
wj9	0.06	-1.15	0.00	0.22	8.42e+08
wj10	0.07	-0.36	0.00	0.46	2.11e+08
core	0.27	0.00	28.12	0.10	6.80e+10
ej10	0.02	0.52	0.00	0.16	5.71e+08
ej9	0.05	0.80	0.00	0.48	1.33e+08

Component	S_{tot} [Jy]	Distance [mas]	P.A. [°]	Major [mas]	T_{b}
wj8	0.04	-1.93	0.00	0.38	1.70e+08
wj9	0.08	-1.22	0.00	0.40	3.24e+08
wj10	0.07	-0.46	0.00	0.29	5.16e+08
	0.03	-0.18	0.00	0.00	3.89e+20
core	0.33	-0.00	49.60	0.08	0.00e+00
ej10	0.09	0.62	0.00	0.55	2.03e+08

Table A.6.: *Parameters for all components of epoch BR120E, BR120F, BR120H, BR120I and BR130A (from top to bottom)*

Component	$S_{\rm tot}$ [Jy]	Distance [mas]	P.A. [°]	Major [mas]	$T_{\rm b}$
wj8	0.02	-2.02	0.00	0.30	1.42e+08
	0.03	-1.62	0.00	0.25	3.33e+08
wj9	0.04	-1.23	0.00	0.25	4.92e+08
wj10	0.06	-0.53	0.00	0.35	3.24e+08
	0.04	-0.20	-4.58	0.24	1.31e+09
core	0.27	0.00	20.67	0.09	0.00e+00
	0.02	0.21	0.00	0.09	1.67e+09
ej10	0.05	0.63	0.00	0.37	2.49e+08
ej9	0.01	1.07	0.00	0.20	2.01e+08
ej8	0.01	1.96	0.00	0.70	1.76e+07
	0.01	3.41	-19.34	0.93	2.08e+07

Component	$S_{\rm tot}$ [Jy]	Distance [mas]	P.A. [°]	Major [mas]	$T_{\rm b}$
	0.02	-3.04	0.00	0.95	1.29e+07
wj9	0.08	-1.70	0.00	0.17	1.89e+09
wj10	0.12	-0.91	0.00	0.34	7.05e+08
core	0.33	-0.01	0.00	0.17	7.55e+09
ej10	0.09	0.71	0.00	0.36	4.49e+08
ej8	0.01	1.91	0.00	0.28	8.95e+07

Component	$S_{\rm tot}$ [Jy]	Distance [mas]	P.A. [°]	Major [mas]	$T_{\rm b}$
	0.01	-2.26	0.00	0.40	4.31e+07
wj11	0.06	-1.64	-22.40	0.25	7.47e+08
wj12	0.14	-1.05	-85.65	0.21	4.13e+09
wj13	0.02	-0.56	0.00	0.20	2.72e+08
wj14	0.01	-0.23	0.00	0.00	2.02e+23
core	0.33	-0.01	80.64	0.20	1.10e+10
	0.14	0.55	0.00	0.32	9.40e+08
ej11	0.03	1.31	0.00	0.46	8.07e+07

Component	$S_{\rm tot}$ [Jy]	Distance [mas]	P.A. [°]	Major [mas]	$T_{\rm b}$
wj11	0.05	-1.78	48.69	0.51	6.72e+08
wj12	0.04	-1.24	0.00	0.22	4.79e+08
wj13	0.03	-0.84	0.00	0.21	4.38e+08
wj14	0.05	-0.37	0.00	0.32	3.43e+08
core	0.26	0.00	0.00	0.00	3.66e+22
ej13	0.05	0.40	0.00	0.26	4.65e+08
ej12	0.04	0.81	0.00	0.22	5.22e+08
ej11	0.03	1.62	0.00	0.70	3.53e+07

Component	$S_{\rm tot}$ [Jy]	Distance [mas]	P.A. [°]	Major [mas]	$T_{\rm b}$
wj11	0.10	-1.65	0.00	0.33	5.86e+08
wj12	0.06	-1.12	0.00	0.12	2.63e+09
wj13	0.02	-0.79	0.00	0.00	5.77e+21
wj14	0.10	-0.41	0.00	0.30	7.27e+08
core	0.29	-0.00	40.50	0.08	0.00e+00
ej12	0.12	0.55	0.00	0.37	5.93e+08
ej11	0.02	1.68	0.00	0.16	5.33e+08

Table A.7.: *Parameters for all components of epoch BR130B, BR130C, BR130D and BR130E (from top to bottom)*

Component	S_{tot} [Jy]	Distance [mas]	P.A. [°]	Major [mas]	T_{b}
wj11	0.06	-1.92	0.00	0.34	3.55e+08
wj12	0.07	-1.36	0.00	0.32	4.44e+08
wj13	0.03	-0.85	0.00	0.26	3.38e+08
wj14	0.08	-0.38	0.00	0.36	4.05e+08
core	0.28	0.00	27.61	0.13	0.00e+00
ej13	0.06	0.38	0.00	0.33	3.64e+08
ej12	0.05	0.83	0.00	0.28	3.94e+08
ej11	0.02	1.70	0.00	0.80	2.46e+07

Component	S_{tot} [Jy]	Distance [mas]	P.A. [°]	Major [mas]	T_{b}
wj11	0.05	-1.92	0.00	0.31	3.54e+08
wj12	0.05	-1.48	0.00	0.27	4.27e+08
wj13	0.04	-0.91	0.00	0.32	2.97e+08
wj14	0.05	-0.46	0.00	0.28	4.78e+08
core	0.37	-0.00	19.85	0.12	0.00e+00
ej13	0.03	0.46	0.00	0.10	1.69e+09
ej12	0.07	0.86	0.00	0.40	2.80e+08
ej11	0.02	1.80	0.00	0.74	2.19e+07

Component	S_{tot} [Jy]	Distance [mas]	P.A. [°]	Major [mas]	T_{b}
wj11	0.05	-2.04	0.00	0.31	3.06e+08
wj12	0.08	-1.53	0.00	0.32	5.19e+08
wj13	0.04	-1.06	0.00	0.23	4.86e+08
wj14	0.09	-0.36	0.00	0.37	4.13e+08
core	0.31	0.00	-24.93	0.02	0.00e+00
ej14	0.02	0.21	0.00	0.00	9.00e+21
ej13	0.08	0.60	0.00	0.46	2.62e+08
ej12	0.02	1.14	0.00	0.21	3.65e+08
ej11	0.03	2.02	0.00	0.91	2.20e+07

Component	S_{tot} [Jy]	Distance [mas]	P.A. [°]	Major [mas]	T_{b}
wj11	0.03	-2.19	0.00	0.39	1.51e+08
wj12	0.05	-1.76	0.00	0.23	6.74e+08
wj13	0.14	-1.39	0.00	0.15	4.01e+09
wj14	0.05	-0.72	0.00	0.43	1.68e+08
wj15	0.13	-0.22	0.00	0.19	2.46e+09
core	0.09	0.03	-14.80	0.14	7.09e+09
ej14	0.22	0.33	0.00	0.37	1.03e+09
ej13	0.05	0.89	0.00	0.18	1.05e+09
ej12	0.03	1.18	0.00	0.15	8.29e+08

Table A.8.: *Parameters for all components of epoch BR130F, BR130G, BR130H and BR130I (from top to bottom)*

Component	$S_{\rm tot}$ [Jy]	Distance [mas]	P.A. [°]	Major [mas]	$T_{\rm b}$
wj11	0.02	-2.10	0.00	0.23	2.97e+08
wj12	0.04	-1.80	0.00	0.13	1.84e+09
wj13	0.11	-1.45	0.00	0.17	2.40e+09
wj14	0.05	-0.86	0.00	0.13	2.01e+09
wj15	0.13	-0.22	0.00	0.17	3.08e+09
core	0.15	0.03	0.00	0.14	4.88e+09
ej14	0.13	0.44	0.00	0.28	1.08e+09
ej13	0.08	0.99	0.00	0.35	4.71e+08
ej12	0.01	1.55	0.00	0.00	2.12e+18

Component	$S_{\rm tot}$ [Jy]	Distance [mas]	P.A. [°]	Major [mas]	$T_{\rm b}$
wj12	0.06	-1.96	0.00	0.26	5.70e+08
wj13	0.08	-1.53	0.00	0.15	2.34e+09
wj14	0.07	-0.93	0.00	0.07	8.71e+09
wj15	0.10	-0.33	0.00	0.21	1.58e+09
core	0.19	-0.02	0.00	0.12	9.44e+09
ej15	0.10	0.36	0.00	0.20	1.53e+09
ej14	0.07	0.81	0.00	0.29	5.65e+08
ej13	0.04	1.30	0.00	0.31	2.41e+08

Component	$S_{\rm tot}$ [Jy]	Distance [mas]	P.A. [°]	Major [mas]	$T_{\rm b}$
wj11	0.01	-2.32	0.00	0.20	2.37e+08
wj12	0.02	-2.05	0.00	0.23	2.63e+08
wj13	0.08	-1.72	0.00	0.22	1.05e+09
wj14	0.09	-1.04	0.00	0.15	2.54e+09
wj15	0.06	-0.35	0.00	0.15	1.76e+09
core	0.28	0.01	53.49	0.34	1.10e+10
ej15	0.05	0.69	0.00	0.33	2.82e+08
ej14	0.05	1.10	0.00	0.41	2.21e+08

Component	$S_{\rm tot}$ [Jy]	Distance [mas]	P.A. [°]	Major [mas]	$T_{\rm b}$
wj12	0.04	-2.19	0.00	0.39	1.64e+08
wj13	0.06	-1.81	0.00	0.20	9.40e+08
	0.02	-1.32	0.00	0.12	1.20e+09
wj14	0.07	-1.16	0.00	0.08	8.17e+09
wj15	0.07	-0.42	0.00	0.32	4.83e+08
core	0.28	-0.01	54.02	0.26	1.41e+10
	0.04	0.35	0.00	0.26	3.61e+08
	0.01	0.61	0.00	0.00	7.90e+21
ej15	0.05	0.96	0.00	0.34	2.80e+08
ej14	0.01	1.44	0.00	0.16	3.68e+08

Danksagung

Mein besonderer Dank gilt meinen Betreuern, die mich stets unterstützt und gefördert haben.
Prof. Dr. Matthias Kadler hat mir schon früh in meinem Studium die Möglichkeit gegeben meine Begeisterung für die Radioastronomie zu entdecken und mich fortwährend darin bestärkt auch größere Herausforderungen anzunehmen. Ohne ihn hätte ich mich nicht in so vielen grundlegenden Bereichen der Radioastronomie vertiefen und neue Techniken erlernen können.
Prof. Dr. Jörn Wilms danke ich für sein jeder Zeit offenes Ohr. Er hat mir bei jedweden Problemen stets zur Seite gestanden und hatte immer einen guten Rat parat.
Prof. Dr. Eduardo Ros verdanke ich es, dass ich den Mut in meinen Kämpfen mit AIPS nicht verloren habe und auftretende Probleme doch lösen konnte. Ohne seine Hilfe und Unterstützung hätte ich wahrscheinlich mein Interesse an VLBI-Techniken und Kalibration schon längst verloren. Besonders seine zahlreichen Kommentare zu meiner Arbeit haben mir sehr weiter geholfen.

Ganz besonders dankbar bin ich für die vielen Möglichkeiten meine Arbeit auf Konferenzen zu präsentieren und meine Fähigkeiten in Workshops noch verbessern zu können. Vielen herzlichen Dank für die Unterstützung und das in mich gesetzte Vertrauen!

Die meisten Erkenntnisse und Lücken im eigenen Wissen findet man erst durch Gespräche mit anderen. Ich bin sehr glücklich in einer so tollen Truppe wie die der Bamberger Astronomen die letzten Jahre verbringen zu dürfen. Die Erweiterung durch die Würzburger hat viele nette Menschen in die Gruppe gebracht, die einige neue Sichtweisen und Interessen mit einbringen konnten.
Besonders hervorheben möchte ich Robert Schulz, der mir währen meiner Masterarbeit stets mit gutem Rat zur Seite stand und einen Großteil seiner Zeit hergegeben hat um mit mir neue Erkenntnisse und auftretende Probleme zu diskutieren.
Ich danke Dr. Christoph Grossberger für die Bereitstellung ausführlicher ISIS Skripte und seine Hilfe bei jedweden programmiertechnischen Problemen.
Sowohl innerhalb als auch außerhalb des beruflichen Umfeldes konnte ich auf viele Menschen immer zählen. Um nur einige zu nennen: Christina Gräfe, Dr. Cornelia Müller, Markus Schindewolf, Sebastian Falkner und Marco Fink.

Ein Studium ist nicht immer einfach, sowohl körperlich als auch psychisch. Hätte ich nicht so viele wunderbare Freunde und eine tolle Familie, die mich in meinen Vorhaben bestärkt und mich, wenn nötig, von diversen Problemen abgelenkt haben, hätte ich die Zeit wahrscheinlich nicht durchgehalten. Hannes hat mir stets Kraft gegeben und mir den Rücken freigehalten wenn dies notwendig war. Seine Liebe und sein Vertrauen in mich hat mich immer in meinem Studium bestärkt und jegliche Zweifel im Keim erstickt.
Ohne die Unterstützung meines Vaters wäre mein Studium gar nicht erst möglich gewesen. Nicht nur finanziell, sondern besonders in seiner Bereitschaft sich jederzeit meine Sorgen und Erfolgserlebnisse anzuhören und mir mit gutem väterlichen Rat zur Seite zu stehen hat mir stets geholfen.

Erklärung

Hiermit erkläre ich, diese Masterarbeit in Eigenarbeit angefertigt zu haben, sofern nicht explizit in Text oder Referenzen vermerkt. Diese Arbeit ist der Universität Erlangen-Nürnberg als Vorraussetzung für den Erhalt des Abschlusses "Master of Science" vorgelegt worden. Ich erkläre, dass diese Arbeit weder partiell noch als Ganzes für den Erhalt eines anderweitigen Abschlusses verwendet wurde und wird.

Erlangen, den

Anne-Kathrin Baczko